

# Method to Sense Changes in Network Parameters with High-Speed, Nonlinear Dynamical Nodes

by

Kristine E. Callan

Department of Physics  
Duke University

Date: \_\_\_\_\_

Approved:

\_\_\_\_\_  
Daniel J. Gauthier, Supervisor

\_\_\_\_\_  
Joshua E. S. Socolar

\_\_\_\_\_  
Stephen W. Teitsworth

\_\_\_\_\_  
Christopher W. Walter

\_\_\_\_\_  
Ying K. Wu

Dissertation submitted in partial fulfillment of the  
requirements for the degree of Doctor of Philosophy  
in the Department of Physics  
in the Graduate School of  
Duke University

2013

# ABSTRACT

## Method to Sense Changes in Network Parameters with High-Speed, Nonlinear Dynamical Nodes

by

Kristine E. Callan

Department of Physics  
Duke University

Date: \_\_\_\_\_

Approved:

\_\_\_\_\_  
Daniel J. Gauthier, Supervisor

\_\_\_\_\_  
Joshua E. S. Socolar

\_\_\_\_\_  
Stephen W. Teitworth

\_\_\_\_\_  
Christopher W. Walter

\_\_\_\_\_  
Ying K. Wu

An abstract of a dissertation submitted in partial fulfillment of the  
requirements for the degree of Doctor of Philosophy  
in the Department of Physics  
in the Graduate School of  
Duke University

2013

Copyright © 2013 by Kristine E. Callan  
All rights reserved

## Abstract

The study of dynamics on networks has been a major focus of nonlinear science over the past decade. Inferring network properties from the nodal dynamics is both a challenging task and of growing importance for applied network science. A subset of this broad question is: How can one determine changes to the coupling strength between elements in a small network of chaotic oscillators just by measuring the dynamics of one of the elements (nodes) in the network? In this dissertation, I propose and report on an implementation of a method to simultaneously determine: (1) which link is affected and (2) by how much it is attenuated when the coupling strength along one of the links in a small network of dynamical nodes is changed. After proper calibration, realizing this method involves only measurements of the dynamical features of a single node.

Previous attempts to solve this problem focus mainly on synchronization-based approaches implemented in low-speed, homogeneous experimental systems. In contrast, the experimental apparatus I use to implement my method comprises two high-speed (ps-timescale), heterogeneous optoelectronic oscillators (OEOs). Each OEO constitutes a node, and a network is formed by mutually coupling two nodes. I find that the correlation properties of the chaotic dynamics generated by the nodes, which are heavily influenced by the propagation time delays in the network, change in a quantifiable way when the coupling strength along either the input or output link is attenuated. By monitoring multiple aspects of the correlation properties, which I call “time delay signatures” (TDSs), I find that the affected link can be determined for changes in coupling strength greater than  $20\% \pm 10\%$ . Due to the sensitivity with which the TDSs change, it is also feasible to determine approximately the time-varying coupling strength for large enough attenuations.

I also verify that the TDSs' sensitivity to changes in coupling strength are captured by a simple deterministic model that takes into account each OEO's nonlinearities, bandpass filtering, and time delays. I find qualitative agreement between my experimental observations and numerical simulations of the model and also use the model to explore the dependence of the TDS signature on the OEO heterogeneity. I find that making the time delays identical leads to larger changes in TDSs, which improves the precision with which the coupling strength can be determined. This also leads, however, to a decrease in the ability to determine which link has been attenuated, indicating that a balance must be struck between optimizing the network's ability to discern the new coupling strength and the affected link. To investigate the role of the nonlinearity, I again test my method numerically using the same delay-coupled topology, but with dynamics generated by a linear stochastic process. I find that sensing can be achieved in the absence of nonlinear effects, but that, with regards to determining which link is affected, the performance is optimized differently in the linear and nonlinear cases.

This method could be extended to design a low-profile intrusion detection system, where several OEOs are spread around a scene and wirelessly coupled via antennas. The ultra-wide-band signals emitted by the nodes (OEOs) can pass through building materials with little attenuation, but would be strongly attenuated by a person who enters the path between two nodes. Beyond practical applications, it also remains to be seen if TDSs could prove to be a simple way to analyze information flow in networks with chaotic dynamics and propagation delays between the nodes.

# Contents

<b>Abstract</b>	<b>iv</b>
<b>List of Tables</b>	<b>ix</b>
<b>List of Figures</b>	<b>x</b>
<b>Acknowledgements</b>	<b>xiii</b>
<b>1 Introduction</b>	<b>1</b>
1.1 Chaos and networks . . . . .	2
1.2 Why use OEOs? . . . . .	4
1.3 Overview of thesis . . . . .	5
<b>2 Nonlinear time-delay dynamical systems and OEOs</b>	<b>8</b>
2.1 Nonlinear and delayed dynamics . . . . .	8
2.2 Nonlinear time-delayed feedback systems . . . . .	12
2.3 The dynamics of my OEO . . . . .	19
2.3.1 Experimental setup and model . . . . .	19
2.3.2 Featureless broadband chaos . . . . .	22
2.3.3 Time-delay signatures . . . . .	24
2.4 Summary . . . . .	28
<b>3 Introduction to sensing with dynamical networks</b>	<b>30</b>
3.1 Overview of the problem . . . . .	30
3.2 Adaptive synchronization-based approach . . . . .	32
3.3 Summary . . . . .	38
<b>4 Sensing method and experimental implementation</b>	<b>39</b>

4.1	Experimental setup . . . . .	39
4.2	Correlation properties of a two-node network of OEOs . . . . .	42
4.3	Using TDSs for sensing . . . . .	49
4.4	Using multiple TDSs for sensing . . . . .	54
4.5	General sensing method . . . . .	55
4.6	Toward optimization . . . . .	63
4.7	Summary . . . . .	64
<b>5</b>	<b>Numerical implementation of the sensing method</b>	<b>67</b>
5.1	Model and integration . . . . .	67
5.2	Proof of principle numerical simulation . . . . .	70
5.3	Other types of observables . . . . .	76
5.4	Impact of the relative values of the time delays . . . . .	77
5.5	Replacing deterministic chaos with stochasticity . . . . .	81
5.6	Summary . . . . .	88
<b>6</b>	<b>Conclusions</b>	<b>92</b>
6.1	Summary of results . . . . .	92
6.2	Future directions . . . . .	95
	<b>Appendix A Experimental apparatus</b>	<b>99</b>
A.1	OEO overview and components . . . . .	99
A.1.1	The laser diodes . . . . .	100
A.1.2	The polarization controllers . . . . .	102
A.1.3	The Mach-Zehnder modulators . . . . .	102
A.1.4	The photodetectors . . . . .	105

A.1.5	The bandpass filters . . . . .	106
A.1.6	The modulator drivers . . . . .	107
A.1.7	The variable optical attenuator . . . . .	109
A.1.8	The time delays . . . . .	109
A.2	Summary . . . . .	110
<b>Appendix B Permutation entropies of experimental dynamics</b>		<b>111</b>
B.1	Definition of PE . . . . .	111
B.2	Using PEs as observables . . . . .	112
B.3	Summary . . . . .	114
<b>Appendix C Numerical analysis and code</b>		<b>119</b>
C.1	ABM Integration . . . . .	119
C.2	Algorithm to calculate TDSs . . . . .	124
<b>Bibliography</b>		<b>126</b>
<b>Biography</b>		<b>130</b>

## List of Tables

2.1	Approximate values of the fixed experimental parameters . . . . .	21
2.2	Approximate value ranges for the adjustable experimental parameters .	21
3.1	Comparison of typical OEO parameter values with and without DSP . .	36
4.1	Measured values of the fixed experimental parameters . . . . .	41
4.2	Value ranges for the adjustable experimental parameters . . . . .	42
4.3	Changes in TDSs for $(\Phi_1, \Phi_2) = (0, -0.08\pi)$ . . . . .	52
4.4	Changes in TDSs for $(\Phi_1, \Phi_2) = (0.08\pi, -0.06\pi)$ . . . . .	52
5.1	Values of the time delays in each of the four scenarios . . . . .	78
B.1	Changes in PEs for $(\Phi_1, \Phi_2) = (0, -0.08\pi)$ . . . . .	114

# List of Figures

1.1	Brief illustration of sensing method . . . . .	6
2.1	Schematic of the Ikeda system . . . . .	13
2.2	MZM transmission function . . . . .	14
2.3	Schematic of typical OEO experimental setup . . . . .	15
2.4	Breather solution . . . . .	18
2.5	Modulator driver transmission function model . . . . .	20
2.6	Featureless broadband chaos . . . . .	22
2.7	Transient pulsing behavior and critical pulse amplitude . . . . .	23
2.8	Experimental time series and ACF for $\Phi = 0$ . . . . .	26
2.9	Experimental ACFs for $\Phi = 0.08\pi$ . . . . .	27
2.10	ACFs in the vicinity of $\tau_d$ . . . . .	28
2.11	TDS at $\tau_d$ as a function of $\Phi$ . . . . .	29
3.1	Adaptive synchronization experimental setup . . . . .	33
4.1	Experimental setup . . . . .	40
4.2	Comparing the dynamics of a single OEO and two coupled OEOs . . . . .	43
4.3	Experimental time series as the input coupling strength varies . . . . .	45
4.4	Experimental ACFs as the input coupling strength varies . . . . .	47
4.5	Experimental ACFs as the output coupling strength varies . . . . .	48
4.6	Experiment: TDSs for $(\Phi_1, \Phi_2) = (0, -0.08\pi)$ . . . . .	50

4.7	Experiment: TDSs for $(\Phi_1, \Phi_2) = (0.08\pi, -0.06\pi)$ . . . . .	51
4.8	Experiment: Strands in TDS-coupling strength space . . . . .	56
4.9	Experiment: Projection of strands in TDS <sub>1</sub> -TDS <sub>2</sub> plane . . . . .	57
4.10	Experiment: Strands in TDS-coupling strength space . . . . .	58
4.11	Experiment: Projection of strands in TDS <sub>1</sub> -TDS <sub>2</sub> plane . . . . .	59
4.12	Illustration of sensing method with a two-node network . . . . .	61
4.13	Experiment: Maximum and minimum signal amplitudes . . . . .	62
4.14	Determining optimal parameters for sensing . . . . .	66
5.1	Mathematical block diagram . . . . .	68
5.2	Single OEO comparison between experiment and simulation . . . . .	69
5.3	Simulation time series and ACF of two coupled OEOs . . . . .	71
5.4	Simulation: TDSs for $(\Phi_1, \Phi_2) = (0.03\pi, 0)$ . . . . .	73
5.5	Simulation: Strands in TDS-coupling strength space . . . . .	74
5.6	Simulation: Projection of strands in TDS <sub>1</sub> -TDS <sub>2</sub> plane . . . . .	75
5.7	Simulation: Maximum and minimum signal amplitudes . . . . .	77
5.8	Simulation: Average change in observables . . . . .	79
5.9	Simulation: Coupling strength necessary to distinguish link . . . . .	80
5.10	Two coupled linear stochastic maps . . . . .	83
5.11	Stochastic map: TDSs as coupling strength varies . . . . .	85
5.12	Stochastic map: Strands in TDS-coupling strength space . . . . .	86
5.13	Stochastic map: Projection of strands in TDS <sub>1</sub> -TDS <sub>2</sub> plane . . . . .	87

5.14 Stochastic map: Average change in observables . . . . .	89
5.15 Stochastic map: Coupling strength necessary to distinguish link . . . . .	90
5.16 Stochastic map: Identical delays . . . . .	91
6.1 Comparison: Average change in observables . . . . .	97
6.2 Comparison: Coupling strength necessary to distinguish link . . . . .	98
A.1 Detailed experimental setup . . . . .	100
A.2 Characterizing laser diode . . . . .	101
A.3 Characterizing $V_{\pi,dc}$ . . . . .	104
A.4 Characterizing $V_{\pi,rf}$ . . . . .	105
A.5 Characterizing bandpass filter . . . . .	107
A.6 Characterizing modulator driver . . . . .	108
B.1 PE for different values of the embedding time . . . . .	114
B.2 Experiment: PEs for $(\Phi_1, \Phi_2) = (0, -0.08\pi)$ . . . . .	115
B.3 Experiment: Strands in PE-coupling strength space . . . . .	116
B.4 Experiment: Projection of strands in $PE_1$ - $PE_2$ plane . . . . .	117

## Acknowledgements

My nonlinear path toward the completion of this dissertation has been significantly improved by many wonderful people. I wish I could acknowledge everyone who has helped me along the way (as seemingly small gestures have had large effects), but, due to space constraints, below is an abbreviated list of some of the most significant contributions.

I'd like to thank my research advisor, Dan Gauthier, for not only supporting my leave from Duke in 2008, but also for encouraging me to keep the option of returning open. At first, I didn't think there was any chance I would ever come back to graduate school; then I didn't think there was a chance I'd come back full-time; and then, before I knew it, I was back. I'd also like to thank him for always trying to understand my struggles and, at times, succeeding. Even in the few weeks prior to my defense, he continued to help me find new ways overcome my fears.

My committee members (Josh Socolar, Stephen Teitworth, Chris Walter, and Ying Wu) have also helped support me over the past three years of my graduate work. I am grateful for the time they took to read my annual reports and this dissertation, to meet with me to discuss my work, and for the occasional hallway conversation just to see how things were going.

The current and former members of the Qelectron group have been invaluable resources during my time at Duke. Those most closely related to my work (Lucas Illing, Zheng Gao, Seth Cohen, David Rosin, and Damien Rontani) have given me helpful scientific criticism and insight. Those with different research interests (Carolyn Martsberger, Andy Dawes, Joel Greenberg, Rena Zhu, Hannah Guilbert, Bonnie Schmittberger, Mei Shi, and Meg Shea) have always been willing to help in any way they can. And all of the members of the Gauthier Wildcats have contributed to making

our office a cheerful environment, for which I am truly grateful.

Derek Leadbetter, Richard Nappi, Ronen Plesser, and Roxanne Springer are, in my opinion, four of the most dedicated teachers in the Duke Physics Department. I'd like to thank Derek for always being willing to show me the latest demo in his collection and inviting me to participate in his outreach events so I could get my teaching fix; Richard for teaching me how to build components for my experiment in the machine shop with an incredible amount of patience and kindness; and Roxanne and Ronen for sharing their interests in both pedagogy and creating a respectful climate, and for going out of their way to be mentors to me.

Prior to my return to my graduate studies, I was fortunate to work with many wonderful colleagues at the Winsor school, in particular Denise Labieniec and Byron Parrish, who never made me feel as though I couldn't ask a question. As a result, I asked a lot of them and learned an incredible amount in the process. And I am confident I would not have returned had I not also worked with such a passionate and fearless group of young women in the classroom, who probably taught me more about courage than I taught them about physics.

Lastly, I'd like to thank my close friends and family for their relentless encouragement during one of the most professionally and personally challenging events in my life. The phone and skype conversations; emails; coffee, lunch, and dinner dates; text messages; offers of a place to live for the summer; funny cards; anxiety-reducing gifts (only some of which were alcohol); and visits (or promises to visit) over the past few months have meant so much to me. I feel privileged to have had the opportunity to pursue graduate studies and, while doing so, elated to have had the support of such caring and thoughtful people. I sincerely hope to be able to return the favor someday.

# Chapter 1

## Introduction

The universe is composed of dynamical systems, many of which are nonlinear and none of which are truly isolated from one another. As such, the last decade has seen the merging of two fields (nonlinear dynamics and complex networks) into the study of dynamics on networks. A few of the many fundamental questions that interest dynamical network scientists are: How do you determine the topological properties of a network from the dynamics of its nodes (the so-called “network inverse problem”)? How does information flow in a network? How does the finite propagation time of information impact the resulting dynamics and our ability to discern the network’s properties?

These problems are relevant and interesting because networks, which are a collection of nodes connected by links, are ubiquitous both in nature (e.g., gene regulatory networks, food webs, the brain) and in human-made structures (e.g., transportation networks, power grids, financial markets). Additionally, many networks have dynamics with timescales as fast or faster than the propagation time between nodes, which means that the propagation time cannot be neglected and further complicates their interaction.

This dissertation relates to a subset of these broader questions: How can one determine changes to the coupling strength between elements in a small network of chaotic oscillators by measuring the dynamics of just one of the elements (nodes) in the network? Besides the fundamental implications for network science, this work is also partially motivated by the desire to exploit chaotic dynamical systems to build novel

sensor networks. My contribution to this field is based on the idea that properties of the dynamics change as a node is decoupled from the network (e.g., due to the presence of an “intruder”), and that these properties change differently depending on precisely how it is decoupled (e.g., where the intruder enters). The particular dynamical characteristics I focus on are termed “time-delay signatures” (TDSs), which, as the name implies, are features due to the inherent propagation delays in my network. I find that TDSs are sensitive to the network properties and can be used in a simple way to diagnose changes to the network. Furthermore, my method to “sense” changes in network properties is applicable to high-speed (ps-timescale) dynamics.

In this first chapter, I give a general overview of chaos and networks. I also motivate the choice of the experimental device central to this dissertation: the optoelectronic oscillator (OEO). Finally, I briefly present the main results presented in this dissertation.

## 1.1 Chaos and networks

It was once a common belief that if all the forces on a classical system could be understood fully, then the future behavior of the system would be known for all time. This is now often referred to as the “Laplacian view,” after the Pierre Simon Laplace. There is, however, something that Laplace’s argument was missing: There is more to the prediction game than just knowing the rules (e.g. the equation of motion of the system). When the dynamics are chaotic, which can happen when the equations of motion are nonlinear, one also needs to know the *exact* starting point in order to win. Since this is impossible to realize, long-term predictability of nonlinear, deterministic systems cannot be guaranteed. Or, as Motter and Campbell recently wrote in a review article appearing in *Physics Today* celebrating the 50th anniversary of the “discovery”

of chaos in a dissipative dynamical system, “Determinism, surprisingly enough, does not preclude chaos” [1].

The way chaotic dynamics defy predictability is through sensitive dependence on initial conditions, popularly known as the “butterfly effect” [2]. This means that if identical chaotic systems are initialized with arbitrarily small differences in their initial conditions, then the difference between the states of the two systems grows exponentially with time. On the surface, the unpredictable nature of chaos may make applications of, or even experimentation with, chaotic systems seem hopeless. However, despite its unpredictability, researchers have found ways to reliably characterize and exploit chaotic dynamics.

While the dynamics of isolated individual systems are important to understand, it is also important to determine how these dynamics are influenced when two or more systems are coupled together to form a network. A network is a mathematical representation of a collection of systems, called nodes or vertices, that interact with one another via links or edges [3]. An example of a network diagram is shown in Fig. 1.1(a), where the nodes are represented with circles and the links are represented with lines. This network is: directional, with the direction of information propagation along the links shown with arrows; weighted, where the interactions that take place via each of the links can have varying strengths  $c_{ij}$ ; and time-delayed, with the propagation time along each link given by  $\tau_{ij}$ .

While commonly occurring networks typically have large numbers of nodes, these networks often have a community structure where, due to structure or function, certain nodes can be grouped together, and this subset of the network can be analyzed to provide insight to the network as a whole [4]. Furthermore, researchers have found that, out of all of the possible three-node networks, some appear as sub-networks of real-life networks more frequently than random chance would predict [5]. These

“motifs” are thought to have increased information processing capabilities. Both of these properties motivate controlled studies of smaller networks, with hopes that, as basic building blocks, they can provide insights to the behavior of larger networks.

I study a system that lies at the intersection of these two fields: a two-node, directed network, where each of the nodes exhibits chaotic dynamics. I am interested in how features of the dynamics at each of the nodes change as each of the link weights that connect the two nodes are tuned from fully coupled to fully uncoupled. In doing so, I find that the dynamics of just one of the nodes can, under the appropriate circumstances, provide information about the global network properties. In principle, this technique to infer global network properties can be extended to larger networks, although one may have to measuring the dynamics of more than one of the nodes.

## 1.2 Why use OEOs?

My experiment comprises two OEOs, which I describe in detail in Ch. 2. For now, it is important to know that each OEO has a nonlinear element, a time-delayed feedback loop, and a delay-coupled output and input. Time delays are known to induce instabilities in experimental systems and were originally considered to be nuisances that should be avoided or controlled [6]. In the 1980s, however, researchers began to realize that time-delay induced instabilities could provide insight about the fundamental physics of the devices and that their resulting dynamics could be useful [6]. Furthermore, in applications with high-speed dynamics, time delays due to signal propagation often cannot be ignored, making the study of their effects essential.

While semiconductor lasers with feedback are a popular system of choice for studying nonlinear systems with delays, OEOs have the advantages that the nonlinearity is simpler to model and agreement between experiments and theory are typically excel-

lent [7]. Additionally, the chaos generated by these devices has noise-like properties and a large bandwidth (20 kHz to 10 GHz), making it an attractive candidate for many low-profile and high-speed applications [8, 9]. Thus, OEOs have recently become a standard bench-top tool to investigate fundamental interactions between nonlinearities and delay, as well as to demonstrate proof of principles for various applications [10]. I extend the utility of these devices to study chaotic dynamics on a small network and show its potential usefulness as a node in a sensor network.

### 1.3 Overview of thesis

In this dissertation, I investigate a method I developed to sense changes in the properties of a network via three different implementations: experimentation with the physical system comprising two OEOs, numerical simulation of a simplified model of the network of OEOs, and numerical analysis of a network of stochastic maps with time-delayed feedback and coupling. I introduce several characteristics of nonlinear and time-delayed dynamical systems in Ch. 2, as well as describe the dynamics of single OEOs that have been analyzed by other researchers and myself. The chapter culminates with my discovery that particular properties of the chaotic dynamics, its TDSs, are sensitive to changes in the OEO parameters. Next, I describe other researchers' attempts to extract information about the properties of a network by manipulating the dynamics of the nodes in Ch. 3, focusing in particular on the experimental work by Cohen *et al.* [11, 12].

I then present my experimental findings in Ch. 4. First, I show that the behavior of the TDSs are sensitive to the coupling strengths along the links of the network. Then I describe a method by which, under the appropriate conditions, an observer can determine: (1) which link is affected, and (2) by how much it is attenuated through

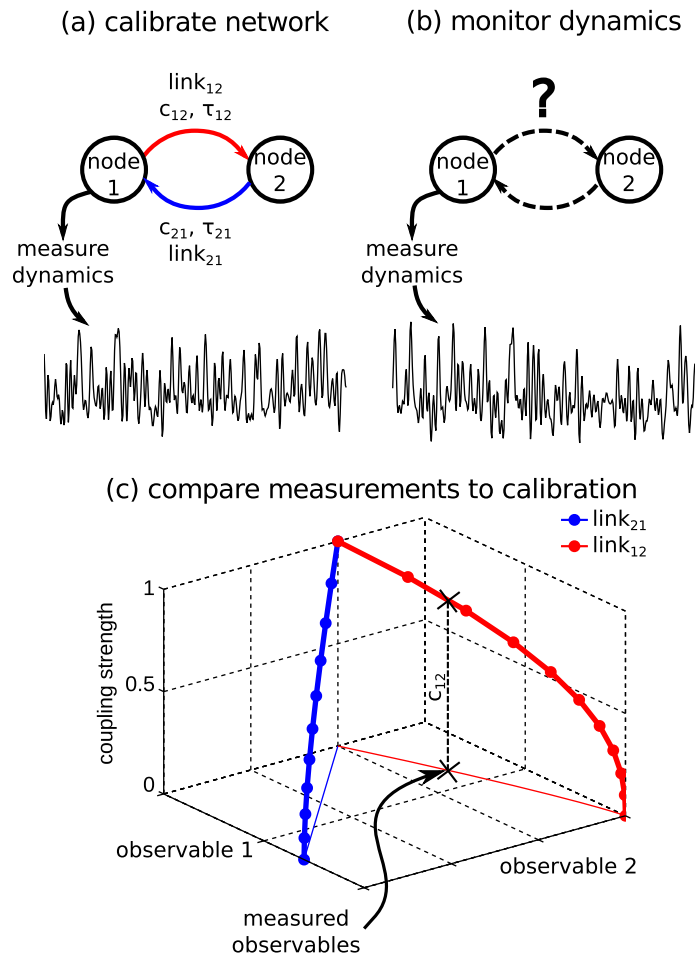


**Figure 1.1: Brief illustration of sensing method.** (a) To calibrate the network for sensing, the coupling strength along each link,  $c_{ij}$ , is independently varied from 0 to 1, while representative time series of the dynamics of one node are recorded. (b) The dynamics of the same node are recorded as an unknown change is made to one of the coupling strengths. (c) Quantitative measures, which I call “observables,” are extracted from the time series and compared against the calibration to determine link location and coupling strength.

monitoring changes in TDSs. This method is briefly illustrated in Fig. 1.1. I find experimentally that sensing can be achieved for an attenuation in coupling strength (link weight) of roughly 20% or greater by monitoring two TDSs. In addition, the changes in these TDSs, when either the input or output link to the observed node is blocked, are on the order of 10 times greater than their experimental uncertainties, making it possible to also approximate changes to the coupling strength of the attenuated link. This method is reliable despite the inherent unpredictability of chaos, the presence of experimental noise and parameter mismatch, and the unavoidable propagation time between the nodes.

In Ch. 5, I first demonstrate that TDSs are present in the chaotic dynamics generated by numerical simulations of a simplified model of my experimental system. I then show that, as with the experimental case, the TDSs are sensitive to both the nodal and network parameters. After demonstrating a numerical proof of principle of my sensing method, I then investigate how the heterogeneity (or lack thereof) in the time delays impacts the performance. I also demonstrate the generality of my method by applying it to a network of linear stochastic maps with the same topology as my experimental network and show that sensing can be achieved without any nonlinear effects. The optimal way in which to implement the sensing method, however, is different in the nonlinear and linear cases.

In Ch. 6, I compare the results obtained from each of these approaches and conclude with some ideas for possible avenues to pursue in the future. In an effort not to distract the reader with details, I save most of the discussion of my experimental apparatus for Appendix A. In Appendix B, I show how a complexity metric, permutation entropy, could be used instead of TDSs as observables in my sensing method. Finally, in Appendix C I provide the details and code for my numerical analyses.

## Chapter 2

# Nonlinear time-delay dynamical systems and OEOs

In this chapter, I explain the important characteristics of both nonlinear and time-delayed dynamical systems and show that combining the two results in very interesting, and potentially useful, dynamics. I present the history of the theory and experiments pertaining to nonlinear delayed-feedback devices. I then introduce the experimental setup that is central to the rest of this dissertation: the optoelectronic oscillator (OEO). This system is well-known in the field for being a versatile bench-top device that is suitable for exploring fundamental aspects of nonlinear physics and delayed dynamics [10]. I then describe the new behavior I discovered and analyzed, part of which was reported in Refs. [8–10, 13]. The features of these dynamics are to be exploited later in this dissertation to make a novel sensor network.

### 2.1 Nonlinear and delayed dynamics

Nonlinear systems are ubiquitous in both nature and human-made devices. In contrast to linear systems, where small changes have similarly small effects, small changes can have relatively large effects in nonlinear systems [2]. This potential for heightened sensitivity makes nonlinear systems appealing candidates for use in applications where one wants to indirectly measure small changes in a factor that influences a system by relating it to large changes in the system's dynamics.

Nonlinear systems are also capable of producing an interesting and paradigm-altering dynamical phenomenon known as chaos. There are three hallmarks of chaos: the behavior is aperiodic; the behavior is deterministic; and the behavior is sensitive

to initial conditions (making it predictable in principle, but not in practice). Once researchers recognized that chaotic behavior was not only possible, but also that it could potentially be useful in certain applications, a large number of scientists began to devote their research to developing simple chaotic devices. A nonlinear system needs to have at least a three-dimensional phase space to be capable of producing chaos, which sets limits on the simplicity of the chaos-generating devices. Furthermore, high-dimensional chaos takes place in a phase space with a dimension much greater than three, which, on the surface, seems to imply that the devices themselves must be rather complex.

Putting the discussion of nonlinear systems on hold for a moment, another type of system that produces interesting dynamics is one with inherent time delays: a system that takes a non-negligible amount of time to acquire or process information before responding to it. A good example from engineering is a control system, which relies on measurements of the current state of the system before outputting an appropriate perturbation to force the system toward the desired behavior. If the time required for the controller to sense the state of the system and output the perturbation is much less than the timescale on which the system responds, then this system can be modeled without a time delay. If, on the other hand, the timescales are similar or the system responds much more quickly than the controller can acquire and output information, then the time delay due to the controller cannot be neglected. In the continuous time limit, these systems obey delay differential equations (DDEs), rather than ordinary differential equations (ODEs). A DDE is an equation in which the state of a dynamic variable at a given time depends on the values of the dynamic variables at both current and previous times, unlike ODEs where only values at current times matter [7].

To get a feel for what makes systems with delays special, I follow Ref. [7] and

consider a linear DDE of the form

$$\dot{x}(t) = \gamma x(t - \tau_d), \quad (2.1)$$

where  $x$  is the dynamic variable, the dot denotes a derivative with respect to time  $t$ ,  $\tau_d$  is the delay, and  $\gamma$  is a parameter that determines the strength of the feedback. The only steady-state solution to Eq. 2.1 is  $x^* = 0$ . If  $\tau_d = 0$  (reducing the DDE to an ODE) the steady-state is stable (unstable) for  $\gamma < 0$  ( $\gamma > 0$ ), and perturbations away from the fixed point exhibit exponential decay (growth). For  $\tau_d \neq 0$  new instabilities are possible.

One can investigate the stability of the steady-state for  $\tau_d \neq 0$  by using the trial solution  $x(t) = e^{\lambda t}$  to obtain the characteristic equation

$$\lambda - \gamma e^{-\lambda \tau_d} = 0. \quad (2.2)$$

Equation 2.2 is transcendental and has an infinite number of roots ( $\lambda$ ), which can be real or complex, that determine the stability of the steady-state solution. The solution is stable if  $\text{Re}(\lambda) < 0$  for all  $\lambda$ . If  $x^*$  is stable for a given set of parameters, it can lose stability as one or more parameters are tuned via a bifurcation [2]. One type of bifurcation, termed a Hopf bifurcation, occurs when a pair of complex conjugate roots cross the imaginary axis and leads to oscillatory behavior. One can determine the ‘‘Hopf curves’’ in parameter space where this bifurcation occurs by setting  $\lambda = i\omega$  in the Eq. 2.2. After separating the real and imaginary terms one obtains

$$\gamma \cos \omega \tau_d = 0, \quad (2.3)$$

$$\omega + \gamma \sin \omega \tau_d = 0. \quad (2.4)$$

These equations can be solved to obtain the condition for a Hopf bifurcation

$$\gamma_H = \pm n \frac{\pi}{2\tau_d}, \quad (2.5)$$

where  $n$  is odd. If  $\tau_d$  is fixed and nonzero, one can show that the fixed point,  $x^* = 0$ , becomes unstable and begins to exhibit oscillatory behavior as  $\gamma$  is decreased below  $-\pi/2\tau_d$ . It can be seen that  $\gamma_H \rightarrow \infty$  as  $\tau_d \rightarrow 0$ , which means that the corresponding first-order ODE cannot oscillate. It is therefore the time delay ( $\tau_d$ ) that is responsible for the instability.

Another substantial difference between ODEs and DDEs is that the former requires an initial condition to determine a solution, whereas the latter requires an entire initial history function (IHF) defined over a length of time equal to  $\tau_d$  [7]. This amounts to supplying an infinite number of initial conditions, which makes the phase space of any DDE infinite-dimensional. Since the complexity of the dynamics is ultimately limited by the number of available phase space dimensions, DDEs can have very simple functional forms and still exhibit a wide variety of complicated behaviors.

Today, DDEs are used to model the behavior of many types of nonlinear systems: physiological diseases [14], population dynamics [15], neuronal networks [16], and nonlinear optical devices [17]. As one might guess from the preceding discussion, combining a nonlinearity with a time delay allows for the possibility of chaotic solutions, even if the systems themselves are relatively simple, due to the infinite dimensional phase space that can be explored by the folding and stretching of the nonlinearity. In the next section, I discuss how scientists began to construct nonlinear systems with time-delayed feedback with the intent of studying the nonlinear dynamics produced by these delay-induced instabilities.

## 2.2 Nonlinear time-delayed feedback systems

Ikeda was one of the first scientists to study a nonlinear system subject to time-delayed feedback [17–20]. Motivated by the optical bistability observed in the intensity of the transmitted light from a Fabry-Pérot cavity (which proved to be very difficult to study theoretically due to the spatial dependence of the counter-propagating electric fields), Bonifacio and Lugiato proposed a slightly different system that was easier to model. This system consisted of a nonlinear absorbing medium placed in an optical ring cavity and subject to a constant-intensity light source, as shown in Fig. 2.1. By using a ring cavity, they introduced the need for a time-delayed feedback term in the equations of motion. Starting with the Maxwell-Bloch equations, Ikeda derived a set of coupled DDEs, which, after a series of assumptions, can be reduced to

$$\tau_l \dot{x}(t) + x(t) = \gamma F_{\text{Ikeda}}[x(t - \tau_d)], \quad (2.6)$$

where  $x$  is proportional to the amplitude of the electric field at the output,  $\tau_l$  is the response time of the dielectric medium (which effectively acts as a low-pass filter with corner frequency  $f_l = 1/\tau_l$ ),  $\gamma$  characterizes the strength of the feedback, and  $F$  is a nonlinear function characterizing the interference between the co-propagating electric fields in the cavity. For this particular system,  $F_{\text{Ikeda}} = \pi[1 + 2B \cos(x - x_0)]$ , where  $B$  represents the dissipation of the electromagnetic field in the cavity and  $x_0$  corresponds to a tuning parameter of the cavity.

The finite propagation time necessary for light to traverse the loop and its nonlinear interaction with the dielectric material results in new types of instabilities. In particular, Ikeda showed that multiple stable steady-states and periodic states can coexist for the same parameter values (multistability). Ikeda also showed numerically that, as  $\gamma$  is increased slowly, the steady-state undergoes a Hopf bifurcation and a square-wave

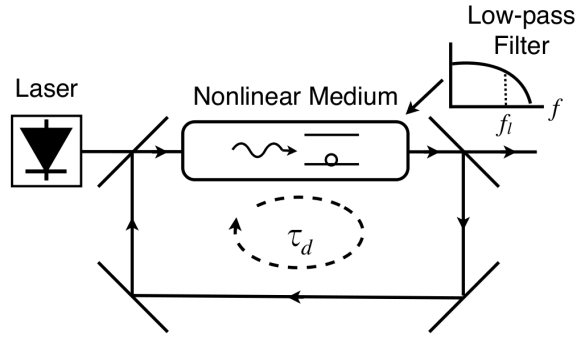


**Figure 2.1: Schematic of the Ikeda system.** Light from the constant-intensity laser source propagates through the nonlinear medium and around the ring via a series of fully and partially reflecting mirrors.

solution with a period approximately equal to  $2\tau_d$  appears. One can linearize the DDE and then use the methods discussed in the first section to predict the value of  $\gamma$  where the Hopf bifurcation occurs. Furthermore, as one continues to increase  $\gamma$ , this square-wave solution undergoes a period-doubling bifurcation (with the universal properties predicted by Feigenbaum) until the solution becomes chaotic. Shortly after Ikeda's prediction, this behavior was first observed experimentally by Gibbs *et al.* [21].

After the pioneering work of Ikeda, several more experiments were designed to investigate Eq. 2.6. One reason these devices became so popular is that the chaos generated could be of arbitrarily high dimension: Farmer showed that the dimension of a chaotic attractor in a time-delayed system increases with the delay [22]. Additionally, the speed of these systems began to increase with advances in technology, making them even more attractive for certain applications, like secure chaos communication [23]. Along with the increase in speed, however, came components that were AC-coupled, meaning that signals below a certain frequency ( $f_h$ ) were also blocked. This led to a new class of DDE that incorporates bandpass filtering rather than just low-pass filtering.

A popular way to increase the speed of Ikeda-like systems is to use a common

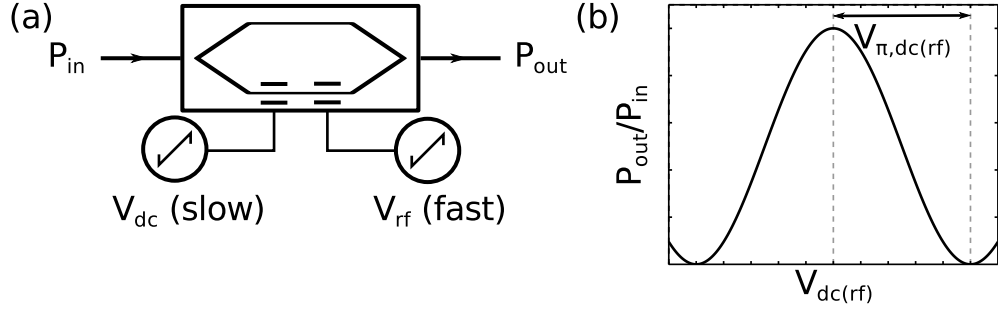


**Figure 2.2: MZM transmission function.** (a) Schematic of method used to measure MZM transfer function and characterize the widths of both the dc and rf ports. A slowly varying ramp voltage ( $f < 1$  kHz) can be applied to the dc port to characterize the width of its interference fringe, and a rapidly varying ramp voltage ( $f > 100$  kHz) can be applied to the rf port to characterize the width of its interference fringe. (b) The interference fringe for the dc (rf) port with the characteristic voltage  $V_{\pi,dc(rf)}$  shown as the voltage necessary to bring the transmission of the MZM from a maximum to a minimum.

(nonlinear) telecommunication component: the electro-optic Mach-Zehnder modulator (MZM). This device modulates the intensity of an incident optical signal by exploiting Pockels electro-optic effect in a lithium niobate crystal in one arm of a Mach-Zehnder interferometer. As shown in Fig. 2.2 when the optical signals from each arm of the interferometer are recombined at the output, their resulting interference depends on a constant bias voltage ( $V_B$ ) and a fluctuating radio-frequency (rf) voltage ( $V_{in}(t)$ ) applied to two electrodes across the crystal. The optical power ( $P_{out}$ ) transmitted through the devices is given by

$$P_{out} = P_{in} \cos^2 \left[ \frac{\pi}{2} \left( \frac{V_B}{V_{\pi,dc}} + \frac{V_{in}(t)}{V_{\pi,rf}} \right) \right], \quad (2.7)$$

where  $P_{in}$  is the power incident on the MZM, and  $V_{\pi,dc}$  and  $V_{\pi,rf}$  characterize the widths of the interference fringe corresponding to each of the two ports.

As shown in Fig. 2.3, a typical setup for an OEO incorporating an MZM is as follows: light generated by a semiconductor laser propagates through an optical fiber to the

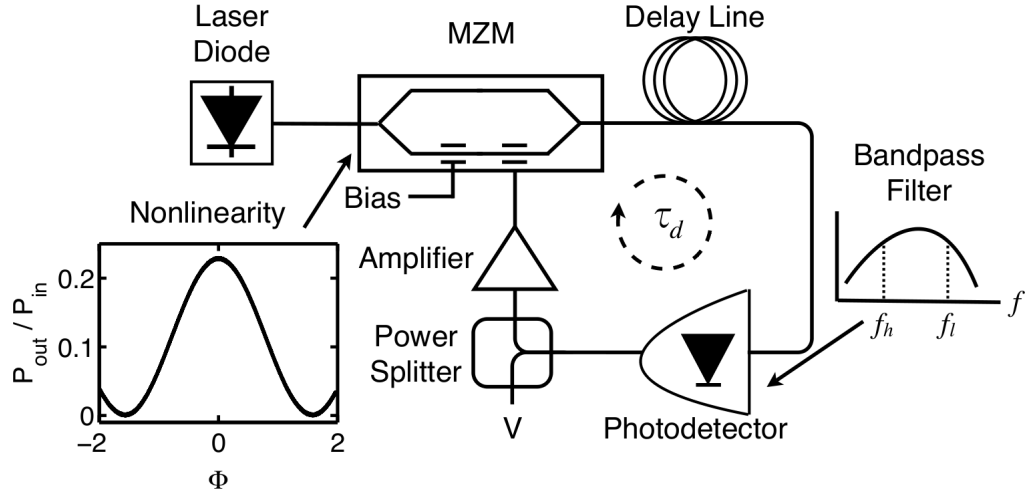


**Figure 2.3: Schematic of typical OEO experimental setup.** This shows the key system components and the order in which a signal originating from the laser diode propagates through them. The measured electrical signal  $V$  is taken from one arm of the power splitter. Inset: Nonlinear transmission of the MZM (ratio of the output to input powers of the device) as a function of the dimensionless operating point  $\Phi$ .

MZM. The light exiting the modulator is incident on a photodetector, and half of the resulting voltage is amplified and fed back into one of the MZM's electrodes (the rf port). The other half is measured with a high-speed oscilloscope. The linear gain in the feedback loop ( $\gamma$ ), the bias voltage applied to the MZM ( $V_B$ ), and the length of the time delay ( $\tau_d$ ) are all easily accessible parameters that determine the dynamics of the measured voltage ( $V$ ).

The fundamental difference between this setup and the one studied by Ikeda is that high-speed photodetectors and amplifiers are typically AC-coupled, and this additional filtering needs to be taken into account when modeling the system. Approximately, this amounts to incorporating a first-order high-pass filter in the model (with high-pass corner frequency  $f_h = 1/\tau_h$ ), in addition to the low-pass filter (with low-pass frequency  $f_l$ ) that characterizes the finite response time ( $\tau_l$ ) of the system's components. This

leads to the dimensionless integro-delay differential equation (iDDE)

$$\tau_l \dot{x}(t) + x(t) + \frac{1}{\tau_h} \int_{t_0}^t x(t') dt' = \gamma F_{\text{MZM}}[x(t - \tau_d)], \quad (2.8)$$

where  $x$  is the dimensionless analog of the measured voltage,  $\gamma$  is the dimensionless gain in the feedback loop, and the nonlinear function is given by

$$F_{\text{MZM}} = \cos^2[x(t - \tau_d) + \Phi] - \cos^2 \Phi, \quad (2.9)$$

with the dimensionless parameter  $\Phi$  determined by the constant bias voltage applied to the MZM according to

$$\Phi = \frac{\pi}{2} \left( \frac{V_B}{V_{\pi, \text{dc}}} \right). \quad (2.10)$$

Equation 2.8 differs from Eq. 2.6 by the inclusion of the integral term corresponding to the high-pass filter.

It is important to note that Eq. 2.8 incorporates three timescales: the time delay of the feedback ( $\tau_d$ ), the high-pass filter response time ( $\tau_h$ ), and the low-pass filter response time ( $\tau_l$ ), where  $\tau_l < \tau_d < \tau_h$ . In typical experiments, these timescales are separated by many orders of magnitude, with  $\tau_l$  on the order of ten picoseconds,  $\tau_d$  on the order of ten nanoseconds, and  $\tau_h$  on the order of microseconds. A variety of dynamics (fundamentally different from those of Eq. 2.6) have been found for different values of  $\Phi$ ,  $\gamma$  and the three timescales [24–28].

Illing and Gauthier proved that the steady-state of Eq. 2.8 becomes unstable through a Hopf bifurcation [29]. Additionally, they used linear stability analysis to show that the frequencies of the periodic states that emerge right after the steady-state bifurcation can be different than the “fundamental” frequency always observed in Ikeda sys-

tems ( $f = 1/2\tau_d$ ). This is because the gain of the bandpass filter is not perfectly flat with respect to frequency. As  $\gamma$  increases, whichever frequency mode has the highest gain overcomes the losses in the loop and achieves stability first. Since the frequencies of each mode in the feedback loop depend on  $\tau_d$ , the mode at threshold also depends on  $\tau_d$ . In a purely low-pass system, however, the lowest frequency mode always has the highest gain, hence one always sees the fundamental frequency at the first steady-state bifurcation regardless of the time delay.

A few years later, Peil *et al.* performed an exhaustive study of the dynamics of an OEO (modeled with Eq. 2.8) analytically, numerically, and experimentally [26]. For low feedback gain ( $\gamma \approx 1$ ), they found that there exist two distinct routes to oscillatory dynamics. For  $-\pi/2 < \Phi < 0$ , the Hopf bifurcation as  $\gamma$  is increased from below threshold leads to fast square-wave solutions, with the period determined by  $\tau_d$ . For  $0 < \Phi < \pi/2$ , however, they found that, as  $\gamma$  increases, the system bifurcates once and then quickly bifurcates again to a low-frequency periodic solution with the period determined by  $\tau_h$ . While the former bifurcation is due to the delay, the latter bifurcation is due to the inclusion of the high-pass filter. As a result, the waveform of this low-frequency solution only includes the timescales  $\tau_l$  and  $\tau_h$ .

As the feedback gain is increased further ( $\gamma \gtrsim 1$ ), the low-frequency solution evolves into a dynamical state termed “breathers” by Kouomou *et al.* [25]. This is a hybrid regime where a fast oscillation is superimposed on the low-frequency oscillation, and an example is shown in Fig. 2.4. The fast oscillations are periodic (quasi-square wave) for lower gain and can become chaotic for higher gain. In a sense, the low-frequency oscillations are essentially sweeping out an Ikeda-like period-doubling bifurcation diagram (though no external parameters are being varied), where the scanning time-period is related to  $\tau_h$ . The chaotic fluctuations are on the order of  $\tau_l$ , while the square-wave oscillations are on the order of  $\tau_d$ . Thus, all three (very different)

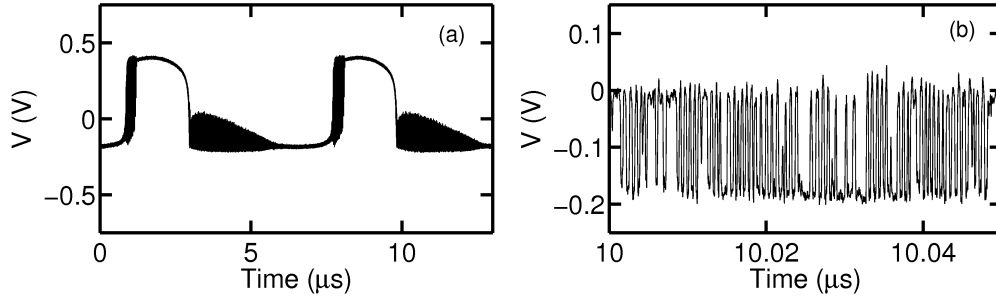


**Figure 2.4: Breather solution.** (a) A zoomed out view of a breather solution obtained with my experimental system with parameter values  $\Phi = -0.23$  and  $\gamma = 1.3$ . (b) A zoomed in view of the fast timescale dynamics.

timescales are present in this dynamical regime. Using a multiple timescale analysis, they were able to accurately predict the frequencies and damping rates present in the breathers.

For high feedback gain ( $\gamma \approx 4$ ), Peil *et al.* observe broadband chaos spanning all three timescales for all values of  $\Phi$ . In this regime, the electric signal fed into the MZM is large enough that it can scan up to three extrema of the nonlinear function shown Fig. 2.2(b). This strong nonlinear feedback produces dynamics with a nearly Gaussian probability density function.

It is interesting to note that the utility of this device has also been successfully demonstrated in the realm of secure chaos communication [30]. The chaos generated by this device was used to encode a message, and the resulting signal was transmitted over 120 km of optical fiber using the metropolitan area network of Athens, Greece. The message was then retrieved using chaos synchronization with a nearly identical OEO at the end of the line. The transmission rates were on the order of gigabits per second. In addition to communications applications, this system has also been used as a stable multiple GHz frequency generator [31, 32] and in reservoir computing

[33, 34].

## 2.3 The dynamics of my OEO

The OEO I study is similar to the one studied by Peil *et al.*, with some important differences. In the following section I describe the basics of my experimental setup and model, as well as the characteristics of the high-speed dynamics I observe.

### 2.3.1 Experimental setup and model

*The results of this subsection were first reported in Refs. [8, 9, 13].*

The main difference between my experimental setup and the one described in the previous section is that the high-speed modulator driver (amplifier) I use saturates for high values of the feedback voltage. To account for this difference, I model the saturation with a hyperbolic tangent function

$$V_{\text{out}} = V_{\text{sat}} \tanh\left(\frac{g_{\text{MD}} V_{\text{in}}}{V_{\text{sat}}}\right), \quad (2.11)$$

where  $V_{\text{in}}$  ( $V_{\text{out}}$ ) is the voltage input (output) of the modulator driver,  $g_{\text{MD}}$  is the gain in the linear region of the modulator driver, and  $V_{\text{sat}}$  is the maximum voltage output of the modulator driver when it is saturated. The relevant parameters are labeled in Fig. 2.5.

By combining the effects of the transmission functions, bandpass characteristics, and time-delay, I arrived at the following set of coupled DDEs (in mostly physical

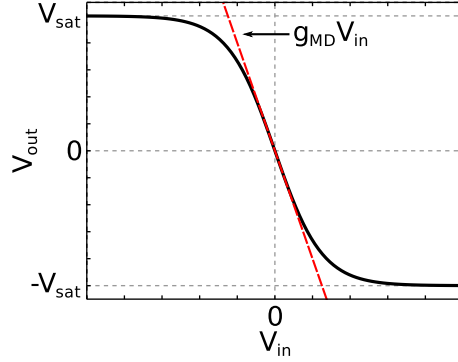


**Figure 2.5: Modulator driver transmission function model.** I use a hyperbolic tangent model to show that small input voltages experience an approximately linear gain with  $g_{\text{MD}} < 0$ , while the output signal saturates for high input voltages at  $V_{\text{sat}}$ .

units) for the measured voltage  $V(t)$

$$\dot{V}(t) = \Delta \{-V(t) - U(t) + F[V(t - \tau_d)]\}, \quad (2.12)$$

$$\dot{U}(t) = \Delta \varepsilon V(t), \quad (2.13)$$

where the nonlinear function  $F[V]$  is given by

$$F[V] = \frac{\gamma g}{d} \left\{ \cos^2 \left[ \Phi + d \tanh \left( \frac{V}{g} \right) \right] - \cos^2 [\Phi] \right\}. \quad (2.14)$$

Here,  $\Delta = 2\pi(f_l - f_h)$ ,  $\varepsilon = f_l f_h / (f_l - f_h)^2$ ,  $g = V_{\text{sat}} / g_{\text{MD}}$ ,  $d = \pi V_{\text{sat}} / 2V_{\pi, \text{rf}}$ , and all other parameters have been previously defined, with approximate values given in Tables 2.1 and 2.2. The variable  $U(t)$  is introduced as an auxiliary variable to account for the integral that appeared in Eq. 2.8. I explain how I determine experimentally each of the quantities that enter Eq. 2.12, 2.13, and 2.14 and their corresponding uncertainties in Appendix A. In what follows, it is important to note that, in my current experimental setup, I estimate my statistical uncertainty in  $\Phi$  to be  $\delta\Phi = 0.005\pi$ .

**Table 2.1:** Approximate values of the fixed experimental parameters

Description	Symbol	Value	Units
Filter high-pass frequency	$f_h$	20	kHz
Filter low-pass frequency	$f_l$	10	GHz
Filter high-pass timescale	$\tau_h$	50	$\mu s$
Filter low-pass timescale	$\tau_l$	100	ps
Filter bandwidth	$\Delta$	$2\pi \times 10^{10}$	rad/s
MD gain	$g_{MD}$	-20	-
MD saturation voltage	$V_{sat}$	5	V
MZM dc port $\pi$ voltage	$V_{\pi,dc}$	7.5	V
MZM rf port $\pi$ voltage	$V_{\pi,rf}$	7.1	V
Re-scaled saturation voltage	$g$	-0.25	V
Dimensionless saturation voltage	$d$	1.1	-
Dimensionless filter parameter	$\varepsilon$	$1 \times 10^{-6}$	-

**Table 2.2:** Approximate value ranges for the adjustable experimental parameters

Description	Symbol	Range	Units
Feedback gain	$\gamma$	(0, 10)	-
Time delay	$\tau_d$	(20, 1000)	ns
MZM operating point	$\Phi$	$(-\pi/2, \pi/2)$	-

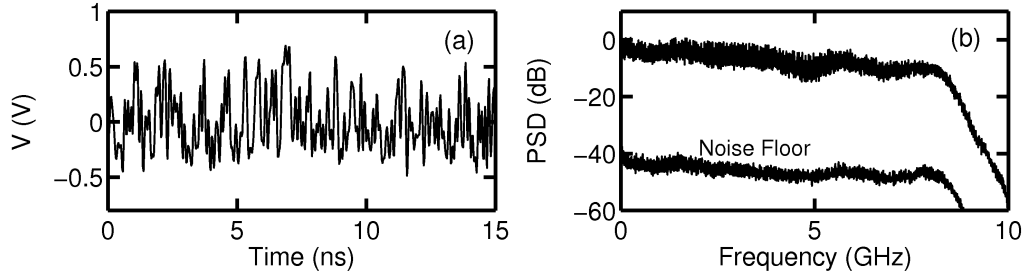


**Figure 2.6: Featureless broadband chaos.** The experimental time series (a) and power spectral density (b) of the broadband chaotic behavior in the physical system for  $\Phi \approx 0$  and  $\gamma = 4.8$  (upper trace). The power spectral density of the noise floor obtained for  $\Phi \approx 0$  and  $\gamma = 4.3$  (lower trace) is also shown. For these parameters, the system is just below the value of  $\gamma$  where the pulsing instability arises.

### 2.3.2 Featureless broadband chaos

*The results of this subsection were first reported in Refs. [8, 9, 13].*

In my experiment, I see similar behavior to other researchers, including square wave oscillations, breathers, and broadband chaos. I was the first person to find, however, that when  $\Phi \approx 0$ , which corresponds to the MZM being biased at a point where the slope is nearly equal to zero, the power spectrum of the observed chaos is essentially “featureless” over a wide range of frequencies (20 kHz to 10 GHz). A typical time series and power spectrum for  $\Phi \approx 0$  are shown in Fig. 2.6. One can see that the power spectrum is essentially flat up to the cutoff frequency of the oscilloscope used to measure the dynamics (8 GHz), with almost no signatures of the three characteristic timescales, indicating that all frequencies are contributing with approximately equal weight. This should be compared to the power spectrum of the (noisy) steady-state behavior just below the steady-state bifurcation threshold also shown in Fig. 2.6(b) (labeled “Noise Floor”), which has approximately the same degree of “flatness.”

In addition to the featureless power spectrum for  $\Phi \approx 0$ , it is also interesting to note

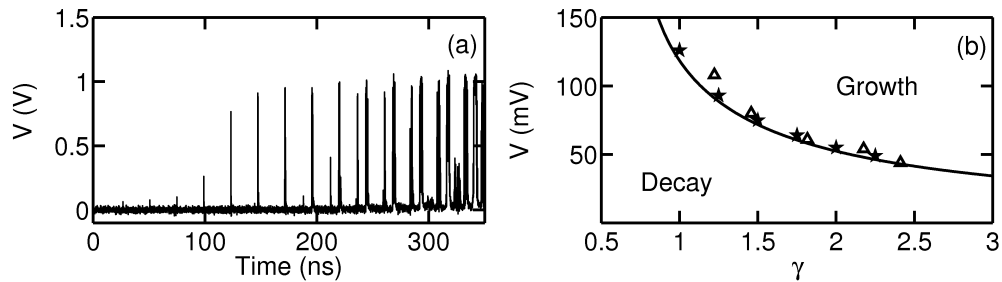


**Figure 2.7: Transient pulsing behavior and critical pulse amplitude.** (a) Experimentally observed transient behavior that results for  $\Phi \approx 0$  and  $\gamma = 4.36$  when the system leaves the steady-state. The pulses have a full width at half maximum  $\sim 0.2$  ns and are separated by the time-delay  $\tau_d$ . (b) The critical pulse amplitude as a function of  $\gamma$  in the experiment (triangles) and simulation (stars) with the prediction from the map superimposed as a solid curve.

that a linear stability analysis of the noise-free model (Eq. 2.8) predicts that steady-state is stable for all values of the gain at this operating point. My finding that the steady-state does transition into chaotic behavior at this operating point for sufficiently large  $\gamma$  indicates that linear stability analysis is not sufficient to describe the dynamics in this case. Furthermore, I find that increasing the noise level of the system causes this transition threshold to lower further, indicating that the likely cause for why the system transitions to this coexisting chaotic attractor is that noise is taking the system outside of the basin of attraction of the linearly-stable fixed point. Since this discovery in my system, Menck *et al.* have argued that the volume of basin of attraction gives a more relevant measure of stability than linear stability analysis. They then used this new metric to give an explanation to the perplexing question of why real-world networks tend to be small-world rather than random, which is what linear stability would suggest [35, 36].

To gain more insight about how the transition from fixed point to chaos occurs as  $\gamma$  increases, I analyze the transient behavior at the transition threshold. An experimental

time series of this transient behavior is shown in Fig. 2.7(a). An analysis of the time series reveals that the transient is comprised of a series of narrow pulses separated in time by  $\tau_d$  and with an average full width at half-maximum (FWHM) of approximately 0.2 ns. These pulses grow in amplitude initially, but the amplitude remains approximately constant after about the sixth pulse. Around this time, a second train of pulses appears to emerge, also with a time separation of  $\tau_d$ . This pulsing behavior motivates approximating the coupled DDEs 2.12 and 2.13 with a one-dimensional map

$$V_{n+1} = F[V_n], \quad (2.15)$$

which describes the amplitude of the pulse peak  $V_n$  for each successive round-trip time  $\tau_d$ . Using Eq. 2.15 with  $\Phi = 0$ , I determine the critical value of  $V_0$  as a function of  $\gamma$  that generates pulses that successively grow in amplitude until leveling off (similar to the observed transient behavior). I then use this value to predict the critical noise level or critical amplitude of an applied perturbation necessary to cause the system to leave basin of attraction of the steady-state via a train of pulses. The excellent agreement between the prediction of the map, experiment, and simulation is shown in Fig. 2.7(b).

### 2.3.3 Time-delay signatures

*The results of this subsection have yet to be reported in the literature.*

Another main difference between my results and those in Ref. [26] is that, while Peil does not report a difference in the chaos observed for different values of  $\Phi$ , I find that the spectral properties within the chaotic regime are extremely sensitive to this parameter. This sensitivity can only be observed, however, if the experimental uncertainty in  $\Phi$  is small relative to  $V_{\pi,dc}$ , which is the case in my current setup as described in Appendix A. I describe how I quantify the changes in the properties of the

dynamics below.

In general, the chaotic dynamics produced by systems with inherent time delays have signatures of those time delays [37]. One way to quantify these signatures is to examine the (normalized) autocorrelation function (ACF) of the time series. The ACF for a time series  $V(t)$  at a time lag  $\theta$  is calculated by

$$\text{ACF}(\theta) = \frac{\int_{t_i}^{t_f} V(t)V(t + \theta)dt}{\int_{t_i}^{t_f} V^2(t)dt}, \quad (2.16)$$

where  $t_i$  and  $t_f$  are the initial and final times of the time series. The ACF of an infinitely long and purely white noise signal is a delta function centered at zero, whereas the ACF of a periodic signal with period  $T$  is also periodic, returning to unity for time lags that correspond to integer multiples of  $T$ . The broadband chaotic signals that I observe, on the other hand, tend to have sharp, well-defined peaks near integer multiples of  $\tau_d$  superimposed on the white noise ACF. An example of an experimentally obtained chaotic time series and ACF for  $\Phi = 0$  is shown in Fig. 2.8(a) and (b). I define a time-delay signature (TDS) at a time  $\theta$  to be the amplitude of the peak in the ACF in the vicinity of time lag  $\theta$ . To make this more concrete, the TDS at  $\tau_d$  is indicated by the red bar in the inset of Fig. 2.8(b). The code I use to calculate TDSs is shown in Appendix C. Repeated measurements of the ACF have remarkably similar structure, as shown in Fig. 2.9 for the case with  $\Phi = 0.08\pi$ . I find that the TDS at  $\tau_d$  with the same experimental parameters, but different IHFs, yield a standard deviation of 0.01, which I take to be my statistical experimental uncertainty  $\delta_{\text{TDS}}$ .

I observe that correlation properties, and hence the TDS at  $\tau_d$ , are sensitive to changes in  $\Phi$ . Some examples of the ACF in the vicinity of  $\tau_d$  for several different values of  $\Phi$  are shown in Fig. 2.10(a-f). This is also illustrated in Fig. 2.11(b), where I plot the TDS at  $\tau_d$  for values of  $\Phi$  ranging from  $-0.08\pi$  to  $0.08\pi$ . This shows that

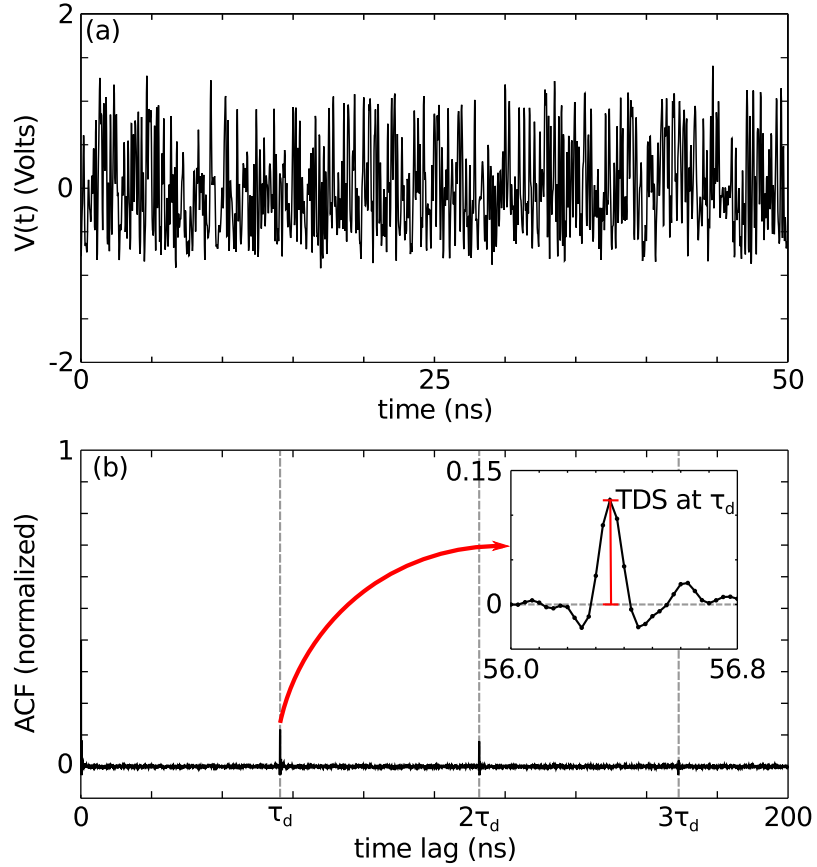


**Figure 2.8: Experimental time series and ACF for  $\Phi = 0$ .** (a) A portion of an experimental time series of  $V(t)$  for  $\Phi = 0$  and  $\gamma \approx 5$ . The full time series lasts for  $13.1 \mu\text{s}$  and was recorded with a high-speed oscilloscope (Agilent DSO90804A, 8 GHz analog bandwidth, 40 GS/s sampling rate). (b) The ACF of  $V(t)$  over a range of time lags from 0 to 200 ns. Peaks occur at multiples of  $\tau_d = 56.4$  ns. A zoomed in view of the peak at  $\tau_d$  with its corresponding TDS is shown in the inset. While the ACF and TDS at  $\tau_d$  were calculated in a post-processing stage, these measurements could be done in real time.

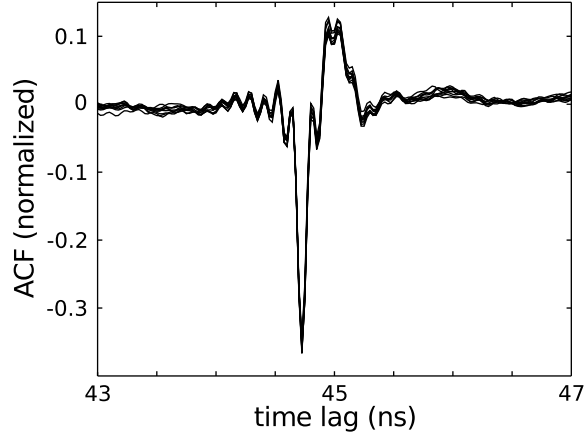


**Figure 2.9: Experimental ACFs for  $\Phi = 0.08\pi$ .** Ten measurements of the ACF in the vicinity of  $\tau_d = 44.7$  ns are overlaid. The structure surrounding the TDS is similar in each of the ten measurements.

changing  $\Phi$  by  $0.01\pi$  ( $2\delta_\Phi$ ) results in changes in the TDS of approximately 0.1, which is on the order of 10 times greater than the measurement uncertainty ( $\delta_{\text{TDS}} = 0.01$ ). Additionally, the TDS at  $\tau_d$  changes monotonically with respect to  $\Phi$ , so that each TDS corresponds to a unique value of  $\Phi$ .

It is also interesting to note that the TDS at  $\tau_d$  is asymmetric with respect to  $\Phi$ . I had initially hypothesized that the broadband chaos was the most “featureless” for  $\Phi = 0$ . However, further study in the experiment and numerical simulations of Eqs. 2.12 and 2.13 shows that this is not the case: the smallest TDS at  $\tau_d$  occurs for  $\Phi \gtrsim 0$  (the exact value of  $\Phi$  for which this occurs depends on the values of all the other parameters, but to the best of my knowledge is always positive). The source of this asymmetry is still unknown. In addition, I find that the TDS at  $\tau_d$  of a single OEO cannot be completely eliminated. The complete elimination of all TDS from the dynamics would be advantageous for some applications, like secure communications [38] and random number generation [39]. The smallest magnitude of the TDS at  $\tau_d$  that I have observed experimentally is  $0.05 \pm 0.01$ .

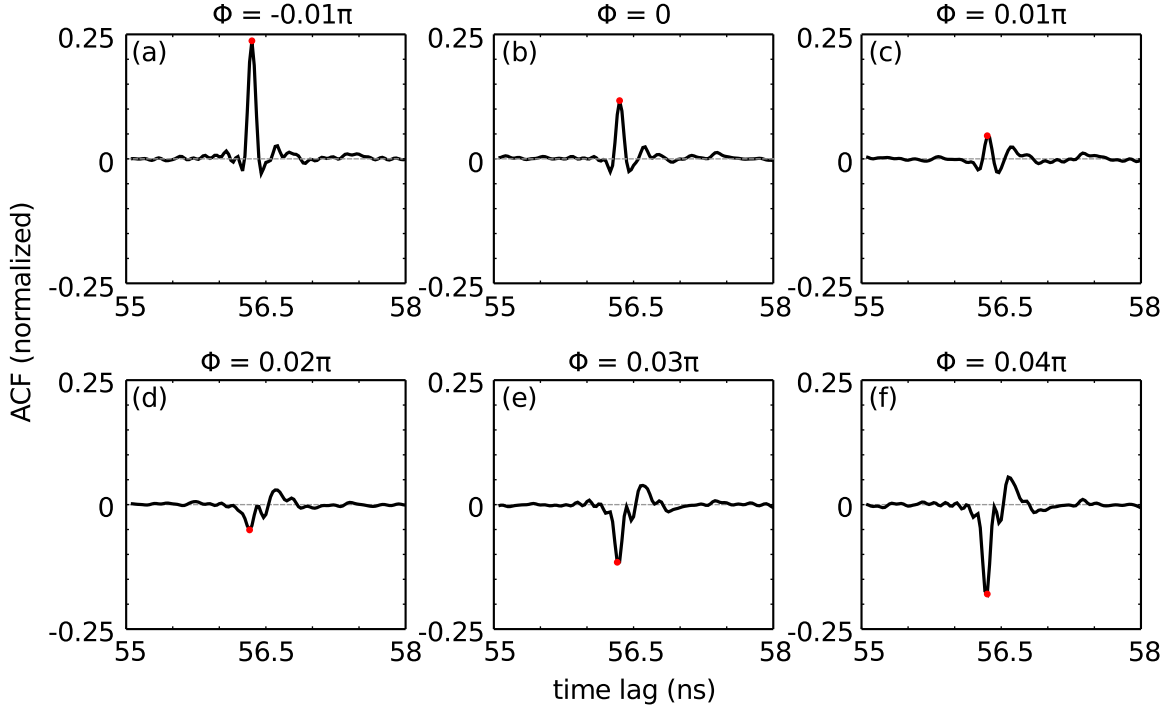


**Figure 2.10: ACFs in the vicinity of  $\tau_d$ .** As the value of  $\Phi$  increases, the value of the TDS at  $\tau_d$  (indicated by the red circle) decreases, switching sign around  $\Phi \approx 0.015\pi$ .

## 2.4 Summary

In this chapter, I show that simple nonlinear time-delayed feedback systems can exhibit a variety of complex dynamics. These systems can be divided into two classes based on the filtering characteristics of the feedback (low-pass and bandpass), and each class is found to have fundamentally different behaviors. One particular bandpass feedback system (an OEO) has proven to be a useful device for studying this class of time-delayed feedback, as the relevant parameters are easy to vary and the agreement between theory and experiment is often excellent. Most importantly, I show that a particular characteristic (the TDS at  $\tau_d$ ) of the chaotic dynamics I observe is sensitive to small changes in parameters, which can be measured in real-time. This feature of the high-speed and broadband chaos is central to my proposed sensing scheme.

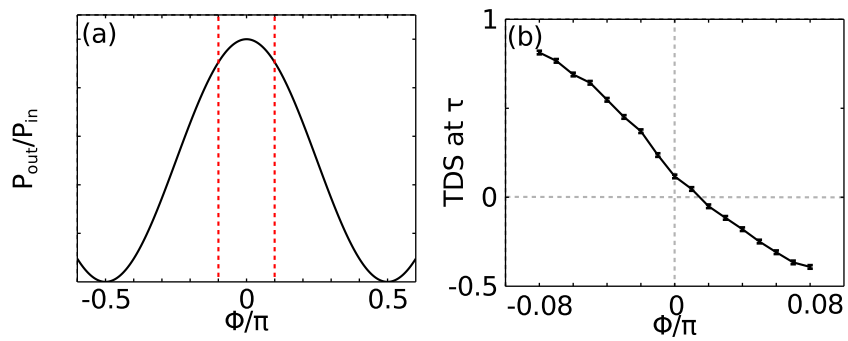


**Figure 2.11: TDS at  $\tau_d$  as a function of  $\Phi$ .** (a) Transmission function of an MZM as a function of dimensionless operating point  $\Phi$  with the relevant region of axes indicated. (b) TDS at  $\tau_d$  as a function of  $\Phi$  over a range near  $\Phi = 0$ .

## Chapter 3

# Introduction to sensing with dynamical networks

In Ch. 2, I introduce several characteristics of nonlinear and delayed dynamics, as well as describe OEOs and the chaos they can generate. In this chapter, I give an overview of a few of the approaches researchers have developed that utilize networks composed of nonlinear dynamical nodes to sense changes in the environment to which they are coupled. I focus, in particular, on one such approach that has been experimentally demonstrated with a network of low-speed OEOs [11, 12, 40, 41].

### 3.1 Overview of the problem

Nonlinear dynamics, and chaotic dynamics in particular, are known for their sensitivity to perturbations [1, 2]. In addition, recent discoveries in complex network science have shown that the interconnectedness of individual dynamical systems can have a profound effect on the overall behavior [42]. With this in mind, researchers hypothesize that, by building a network composed of chaotic nodes, the dynamics at each of the nodes are sensitive to the coupling topology of the network. Furthermore, if this network is then placed in an environment that influences the coupling topology, then by measuring the dynamics of one, a few, or all of the nodes, it might be possible to determine the time-varying properties of the environment with a high degree of precision.

One potential application of such a sensor network is an intrusion detection device. For this application, the dynamics generated by each of the nodes are broadcast and

received by antennas to form the proposed network. The dynamics should also be ultra-wide-band (UWB), as defined by the Federal Communications Commission (FCC) regulation 47CFR15.503. That is, they have a fractional bandwidth greater than 20% or a bandwidth greater than 500 MHz; they operate below 10.6 GHz; and they are low power. UWB radiation is desirable because it penetrates many building materials, such as drywall and concrete [43], and does not penetrate substantially water (and hence people). Therefore, these proposed networks have properties (e.g., link weights) that depended upon the presence (or lack thereof) and position of any water-based elements, which I refer to as intruders. An added advantage of using UWB devices is that they are unregulated by the FCC, which means any devices that adhere to these guidelines have the potential to be commercialized. In addition to being UWB, the signals should also have wavelengths with roughly the same order of magnitude as the length scales of potential intruders (i.e.,  $\lambda \sim 10^{-1} - 10^1$  m,  $f \sim 10^7 - 10^9$  Hz) if one hopes to image their presence with standard techniques. As I show in the previous chapter, OEOs are ideal candidates for producing dynamics with the UWB and high-speed properties required for this application.

This sensing task essentially boils down to: How does one identify certain properties of a network from limited measurements and available information? Thus far, the methods that have been proposed to perform this task can mostly be divided into two categories: perturbation-based and synchronization-based approaches (see Ref. [44] and the references therein). Due to the complexity of this task, however, most of these methods make assumptions such as: the parameters of the nodes are known and often identical; the coupling between nodes is linear; communication between nodes happens instantaneously (no propagation delay); and the dynamics of each node can be acquired simultaneously (see Ref. [45] and the references therein). For the application I have in mind, many of these assumptions are impractical for sensing the properties

of the network in real time. In the next section, I give an overview of an approach that extracts information about the properties of a network in a way that is better suited for the intrusion detection task.

## 3.2 Adaptive synchronization-based approach

One potential approach to uncovering network properties from the dynamics of one or more nodes in real time is based on adaptive synchronization [40]. This method was successfully implemented using a network of three bidirectionally coupled OEOs in Ref. [11, 12]. I explain the basics of the method below.

The basic experimental setup is shown in Fig. 3.1. Each of the three nodes is an OEO, similar to the ones described at the beginning of Ch. 2, but rather than incorporating just a time-delayed self-feedback signal, each OEO also receives a time-delayed signal from its two neighbors. Each OEO also incorporates a digital signal processor (DSP), which I discuss later. The strength of the signal that is allowed to propagate from  $\text{OEO}_i$  to  $\text{OEO}_j$  is determined by the corresponding element of the weighted adjacency matrix  $A_{ij}$ , and the goal is to determine the unknown and time-varying elements of this matrix, under the assumption that these coupling strengths are changing on a much slower timescale than that of the dynamics on the nodes.

This method relies on the fact that, under certain circumstances, two or more chaotic systems can synchronize [46]. That is, each chaotic system is doing the same thing at the same time. Since its initial discovery, this counter-intuitive phenomena has been demonstrated in numerous experiments. However, the criteria for synchronization is often very strict. To determine whether or not a synchronized solution for a given coupling topology is stable, one can use the master stability function approach derived in Ref. [47]. Adaptive synchronization techniques use knowledge of the master

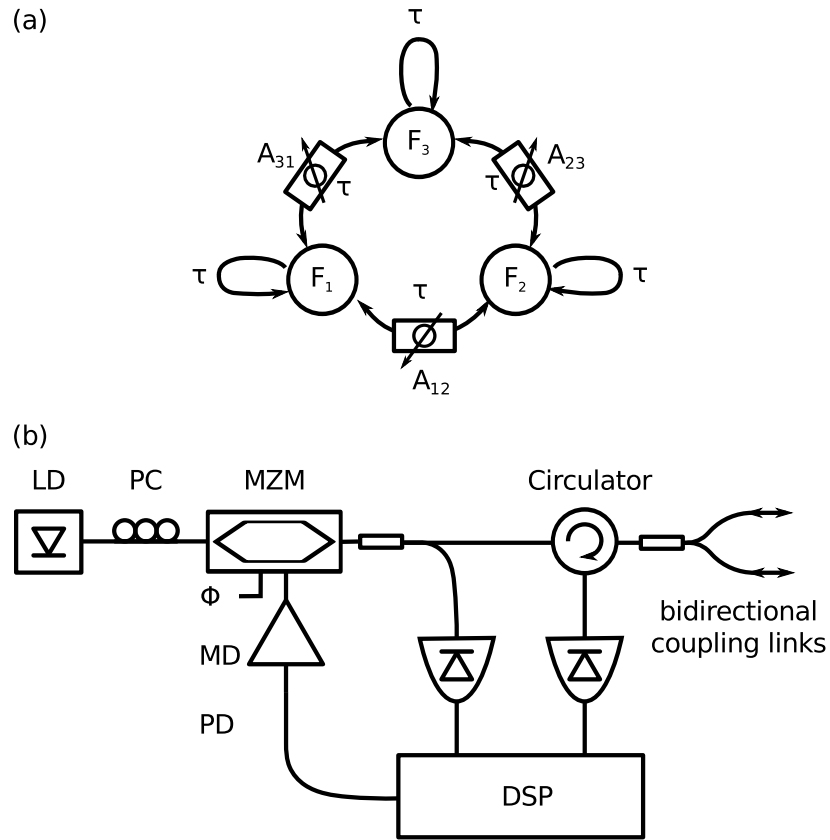


**Figure 3.1: Adaptive synchronization experimental setup.** (a) A simplified diagram of the setup, with the nonlinear elements represented as nodes and the self-feedback and coupling delay lines represented as links. (b) A detailed diagram of one of the nodes in the setup. Each OEO consists of a laser diode (LD), polarization controller (PC), Mach-Zehnder modulator (MZM), two 50/50 optical couplers, a circulator, two photodiodes (PD), a digital signal processor (DSP) and a modulator driver (MD). The signal exiting one MZM is split so that half is fed back to the itself and half is sent to the other two OEOs via two bidirectional fiber optic channels.

stability function to drive the network toward synchrony.

To make this more concrete, I follow Ref. [11] and consider a network of  $N$  dynamical systems of the discrete-time form

$$\mathbf{x}_i(n+1) = \mathbf{F}(\mathbf{x}_i(n)) + \mathbf{v} \frac{\alpha_0}{k_i} r_i(n), \quad (3.1)$$

where  $\mathbf{x}_i(n)$  denotes the state vector of one time-delay worth of sample points from node  $i$  at time  $n$ , the vector function  $\mathbf{F}(\mathbf{x})$  describes the internal dynamics,  $\alpha_0$  is the overall coupling strength, and  $\mathbf{v}$  is a vector describing how the net received coupling signal  $r_i(n)$  is incorporated. This received signal is given by

$$r_i(n) = \sum_j A_{ij} H(\mathbf{x}_j(n)), \quad (3.2)$$

where  $\mathbf{A}$  is the weighted adjacency matrix that specifies the coupling strength of each of the network's links and  $H$  is a scalar function describing how the nodes are coupled. Finally, the net coupling strength into node  $i$  is given by

$$k_i = \sum_j A_{ij}. \quad (3.3)$$

The values  $A_{ij}$  are crucial to whether or not synchronization occurs, but are unknown. Therefore, synchronization has to be maintained based solely on the physically accessible signal  $r_i(n)$ . To do this, each node implements an adaptive strategy that seeks to minimize the time-averaged synchronization error among the three nodes. Equation 3.1 was designed such that a synchronized solution  $\mathbf{x}_1(n) = \mathbf{x}_2(n) = \dots = \mathbf{x}_N(n) \equiv \mathbf{x}_S(n)$  satisfies

$$\mathbf{x}_S(n+1) = \mathbf{F}(\mathbf{x}_S(n)) + \mathbf{v} \alpha_0 H(\mathbf{x}_S(n)), \quad (3.4)$$

where  $r_i(n) = k_i H(\mathbf{x}_s(n))$ . Thus, if  $k_i = \sum_j A_{ij} = 1$  for all  $i$ , the nodes synchronize. However, the values of  $A_{ij}$  are unknown and time-varying, which is where the adaptive strategy comes in. Re-expressing Eq. 3.1 as

$$\mathbf{x}_i(n+1) = \mathbf{F}(\mathbf{x}_i(n)) + \mathbf{v}\beta_i(n)r_i(n), \quad (3.5)$$

the time-averaged synchronization error is minimized when the (controllable) weight factor  $\beta_i(n)$  is given by

$$\beta_i(n) = \alpha_0/k_i(n). \quad (3.6)$$

If the variations in  $A_{ij}$  vary slowly compared to the length of time over which the synchronization error is averaged, then the value of  $\beta_i(n)$  necessary to achieve synchronization is computed from  $H(\mathbf{x}_i(n))$ ,  $r_i(n)$ , and  $\alpha_0$ . Once this  $\beta_i(n)$  is known, then so is  $k_i(n)$ . Thus, the interesting byproduct of this method is that, in the process of maintaining synchronization, the adaptive algorithm at node  $i$  “learns” the net coupling strength of the input signals  $k_i(n)$ .

This method was successfully implemented in an experimental three node network of OEOs, generating high-dimensional chaos, to track both sudden and smoothly varying changes in the values of  $k_1$ ,  $k_2$ , and  $k_3$  [11, 12]. In this experiment, the weighted adjacency matrix  $\mathbf{A}$  was taken to be symmetric, therefore the values of the coupling strengths  $A_{12}(n)$ ,  $A_{23}(n)$ , and  $A_{31}(n)$  could be solved for using  $k_1$ ,  $k_2$ , and  $k_3$ . Furthermore, the authors numerically implemented their method with a larger network of OEOs ( $N = 25$ ), but with mixed success, due to the fact that synchronization is only possible for certain coupling configurations. Also, for these larger networks the number of links can be greater than the number of nodes, making determination of the

**Table 3.1:** Comparison of typical OEO parameter values with and without DSP

Parameter	OEO without DSP	OEO with DSP	Units
$f_h$	$10^3$	$10^2$	Hz
$f_l$	$10^{10}$	$10^3$	Hz
$\tau_d$	$10^{-9}$	$10^{-3}$	s

values of  $A_{ij}$  from the values of  $k_i$  impossible.

The limitations of this scheme are: (1) it relies on synchronization, which severely limits the allowed parameter mismatch among the nodes and network topologies; (2) it requires dynamical measurements of all nodes; (3) while probing each node, a signal ( $\beta_i(n)$ ) must be output based on the dynamical state; (4) for larger networks it only provides the net input coupling strength to each node, rather than the coupling strength along each link; and (5) it fails when the nodes are completely uncoupled ( $k_i = 0$ ), as synchronization can no longer be maintained. The easiest way to meet requirements (1) and (3) is to slow down the dynamics. The authors do this with the use of a DSP at each node, which implements the bandpass filtering and delay digitally to ensure that the bandpass characteristics and delays are uniform among all the nodes. As a result, the use of the DSP allows for better agreement between experiment and theory, and the DSP also performs the necessary calculations to properly rescale the received signals. The addition of the DSP in their system decreases the speed of the chaotic dynamics (which roughly scale with the time delay) by about six orders of magnitude, as can be seen in Table 3.1. While the dynamics are UWB, their wavelengths are on the order of  $10^5 - 10^6$  m, making it unlikely that a person-sized intruder would produce large enough changes to the coupling strengths to be detected.

In Ref. [41], the authors investigate numerically the influence of the propagation delay between the nodes under a slightly different coupling strategy and find that

keeping the time delays distinct improves the likelihood of identifying the coupling strengths of the individual links (not just the net coupling strength into a given node). Note that, in order for the propagation delay between nodes to be non-negligible in a wireless network with the low-speed dynamics shown in Table 3.1, the nodes either have to be separated by  $\sim 10^5$  m or incorporate a buffer. They also investigate the effect of parameter mismatch, and find that, in order to keep their identification errors less than 10%, the parameters need to be matched within a 3% tolerance. Finally, they investigate an alternate version of their strategy that makes use of an additional “maestro” node, whose coupling to the other nodes in the network is assumed to be known and is responsible for maintaining the network synchrony. There have been no experimental verification of these claims, however, and, to the best of my knowledge, the only experimental implementations of an adaptive strategy to track time-varying coupling strengths are reported in Ref. [11, 12, 48], where the experiments are carried out with two- and three-node networks.

In Ref. [49], the authors use a similar adaptive strategy, but only rely on dynamical measurements of a single node rather than all the nodes. Instead of maintaining synchrony on the network, however, they seek to maintain synchrony between the  $N^{\text{th}}$  node of the network with unknown coupling strengths and a replica network with adaptable coupling strengths. They have demonstrated the ability to successfully track the time-varying coupling strengths in numerical simulations with a chain of  $N = 3$  nodes. Their method has the advantages that one only needs to measure one node and the nodes can be heterogeneous (as long as the parameters are known), but suffers from the disadvantages that the performance degrades with increasing  $N$  and its speed is limited by the need to measure and respond to the dynamics. While it is not a promising candidate for the application I have in mind, the authors conjecture that it could be applied to estimating time-varying synaptic strengths within small neuronal

networks.

### **3.3 Summary**

In this chapter, I discuss an experimental demonstration of a method to track time-varying coupling strengths in a small network of OEOs. However, this method requires that: the OEOs be nearly identical; the dynamical measurements of all of the nodes are continuously performed; and the received signals are appropriately scaled. The end result is that the dynamics have to be slowed down by six orders of magnitude than that of a typical OEO. This million-fold decrease in frequency (and increase in wavelength) is undesirable for applications, and, therefore, schemes that can be implemented with high-speed dynamics must be explored. In the next chapter, I introduce a new method I developed to track time-varying coupling strengths in a small network of heterogeneous, high-speed OEOs based on dynamical measurements of a single node.

## Chapter 4

# Sensing method and experimental implementation

I find in Ch. 2 that OEOs can produce high-speed and broadband chaos and that the properties of this type of chaos are sensitive to the system's parameters. I quantify the changes in correlation properties by monitoring changes in TDSs. In Ch. 3, I discuss recently developed methods for determining network parameters when two or more chaotic systems are coupled together. These methods are often limited to low-speed dynamics generated by homogeneous nodes. In this chapter, I show how I can take advantage of the TDSs produced by a network of two coupled OEOs to “sense” changes in the network parameters in real time with heterogeneous nodes generating high-speed dynamics. I focus mainly on the utility of TDSs, as they are both sufficiently sensitive to changes to the network parameters and relatively quick to calculate.

### 4.1 Experimental setup

I construct a two-node OEO network to investigate whether TDSs embedded in the chaotic dynamics generated by the OEOs can be used for sensing changes to the network properties. Both simplified and detailed experimental schematics are shown in Fig. 4.1. I modify the single OEO setup shown in Ch. 2 by adding three additional 50/50 optical couplers and one additional high-speed photodiode. The first coupler and photodiode serve to measure the signal coming directly out of the MZM, which I denote  $X_i(t)$ . The other two couplers serve to split and combine the signals passing between  $OEO_1$  and  $OEO_2$ . The fixed parameters of each OEO differ by roughly 10%

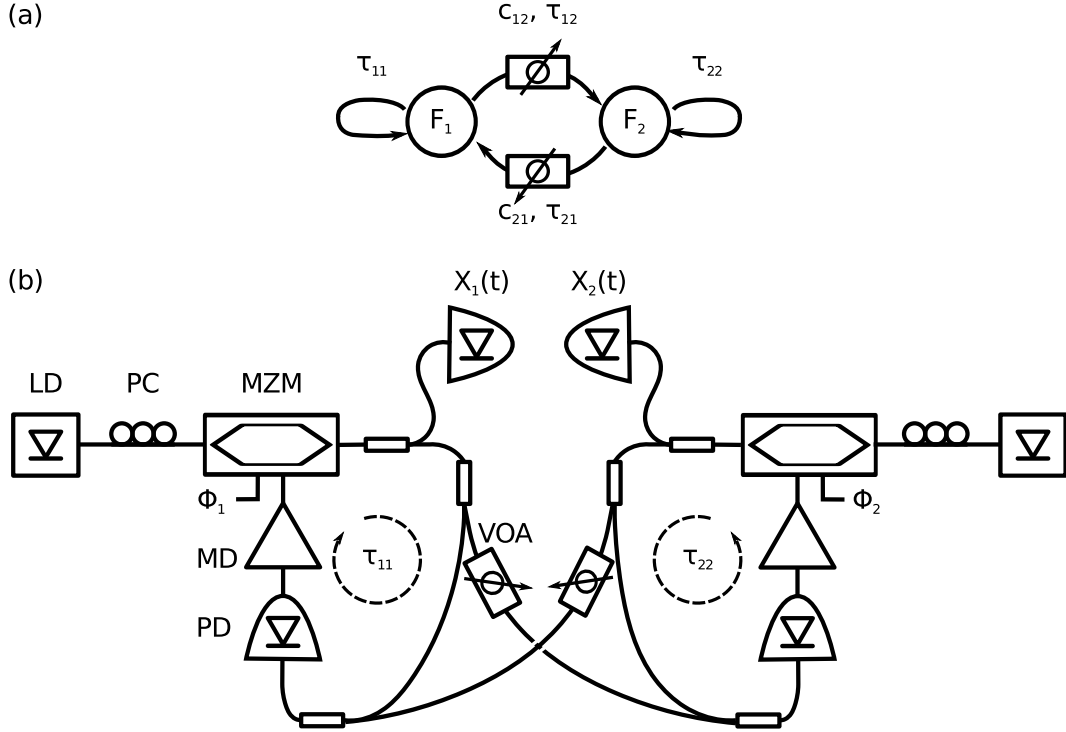


**Figure 4.1: Experimental setup.** (a) A simplified diagram of the setup, with the non-linear elements represented as nodes and the self-feedback and coupling delay lines represented as links. (b) A detailed diagram of the setup. Each OEO consists of a laser diode (LD), polarization controller (PC), Mach-Zehnder modulator (MZM), three 50/50 optical couplers, a variable optical attenuator (VOA), two high-speed photodiodes (PD), and a modulator driver (MD). The signal exiting one MZM is split twice so that half is measured, a quarter is sent to the other OEO, and a quarter is fed back to itself.

and are given in Table 4.1. I discuss how the values of each of these parameters are determined in Appendix A.

The adjustable parameters for my two-node network are: the self-feedback time delays  $\tau_{11}$  and  $\tau_{22}$ ; the coupling time delays  $\tau_{12}$  and  $\tau_{21}$ ; the dimensionless self-feedback gains  $\gamma_1$  and  $\gamma_2$ ; the (normalized) coupling strengths  $c_{12}$  and  $c_{21}$ ; and the MZM operating points  $\Phi_1$  and  $\Phi_2$ . I use the notation  $x_{ij}$  to denote the quantity  $x$  along a link that passes from  $\text{OEO}_i$  to  $\text{OEO}_j$  (see Fig. 4.1(a)). Without adding any extra components, the self-feedback times of each OEO and the coupling delay times are different from

**Table 4.1:** Measured values of the fixed experimental parameters

Parameter	Value for OEO <sub>1</sub>	Value for OEO <sub>2</sub>	Units
$f_h$	$16 \pm 7$	$25 \pm 11$	kHz
$f_l$	$10 \pm 0.4$	$10 \pm 0.3$	GHz
$g_{\text{MD}}$	$-18.7 \pm 1.5$	$-22.6 \pm 1.1$	–
$V_{\text{sat}}$	$4.5 \pm 0.2$	$5.0 \pm 0.2$	V
$V_{\pi,\text{dc}}$	$7.18 \pm 0.02$	$7.62 \pm 0.03$	V
$V_{\pi,\text{rf}}$	$7.14 \pm 0.07$	$7.15 \pm 0.07$	V
$g$	$-0.24 \pm 0.02$	$-0.22 \pm 0.02$	V
$d$	$0.98 \pm 0.07$	$1.1 \pm 0.07$	–
$\varepsilon$	$(1.6 \pm 0.7) \times 10^{-6}$	$(2.5 \pm 1) \times 10^{-6}$	–

each other:  $\tau_{11} = 44.7$  ns,  $\tau_{22} = 56.4$  ns, and  $\tau_{12} + \tau_{21} = 116.6$  ns. This is due to the fact that each fiber-optical component has a different length of fiber attached to it. A general guide for fibers is that 1 meter of fiber corresponds to 5 ns of propagation time, so these differences in time delay equate to fiber length differences on the order of a few meters. In principle, these could be made to be equal to within less than a picosecond by using additional components, but I hypothesize that keeping these timescales distinct improves sensing. I, therefore, leave the study of the identical time delay situation for the next chapter. The gain of each feedback loop is determined by adjusting the power of each laser diode, and I choose values of  $\gamma_1 = \gamma_2 = 5 \pm 0.5$ , which results in chaotic dynamics for a wide range of  $(\Phi_1, \Phi_2)$  values. The value ranges for each of the adjustable parameters are given in Table 4.2. The experimental statistical uncertainties are also shown, and I explain how each of these is determined in Appendix A.

**Table 4.2:** Value ranges for the adjustable experimental parameters

Parameter	Range	Uncertainty	Units
$\gamma$	(0, 6)	$\pm 0.5$	–
$\tau_{11}, \tau_{22}, \tau_{12} + \tau_{21}$	(20, 1000)	$\pm 0.050$	ns
$\Phi$	$(-\pi/2, \pi/2)$	$\pm 0.005\pi$	–
$c_{12}, c_{21}$	(0, 1)	$\pm 0.01$	–

## 4.2 Correlation properties of a two-node network of OEOs

While a single OEO has only one time delay ( $\tau_d$ ), two bi-directionally coupled OEOs have four time delays ( $\tau_{11}$ ,  $\tau_{22}$ ,  $\tau_{12}$  and  $\tau_{21}$ ). Here, the single self-feedback delay time  $\tau_d$  of the isolated OEO is replaced by two distinct self-feedback delay times  $\tau_{11}$  and  $\tau_{22}$ . In Ch. 2, I see that the ACF for broadband chaotic dynamics generated by a single OEO has sharp peaks at time lags equal to integer multiples of  $\tau_d$ , and I refer to the height of a peak in the vicinity of time lag  $\theta$  as the TDS at  $\theta$ . For my two-node OEO network operating in an analogous broadband chaotic regime, the correlation properties are quite different. In particular, the ACF of a time series taken from one of the two nodes has sharp peaks at time lags equal to integer multiples of: the self-feedback time delays  $\tau_{11}$  and  $\tau_{22}$ ; the round-trip coupling delay time  $\tau_{12} + \tau_{21}$ ; and sums and differences of these three timescales. The differences in dynamics, correlation properties, and spectral properties between a single OEO and two coupled OEOs are illustrated in Fig. 4.2. I use the following notation to refer to the TDSs that characterize the dynamics of OEO<sub>1</sub> (OEO<sub>2</sub>) at the various delay times:  $\tau_{11}$  ( $\tau_{22}$ ) is  $\tau_{\text{self}}$ ;  $\tau_{22}$  ( $\tau_{11}$ ) is  $\tau_{\text{other}}$ ; and  $\tau_{12} + \tau_{21}$  is  $\tau_{\text{coupling}}$ .

To investigate what happens to the correlation properties as the coupling strengths of the network change, I select values for  $\Phi_1$  and  $\Phi_2$  (the operating points of the non-

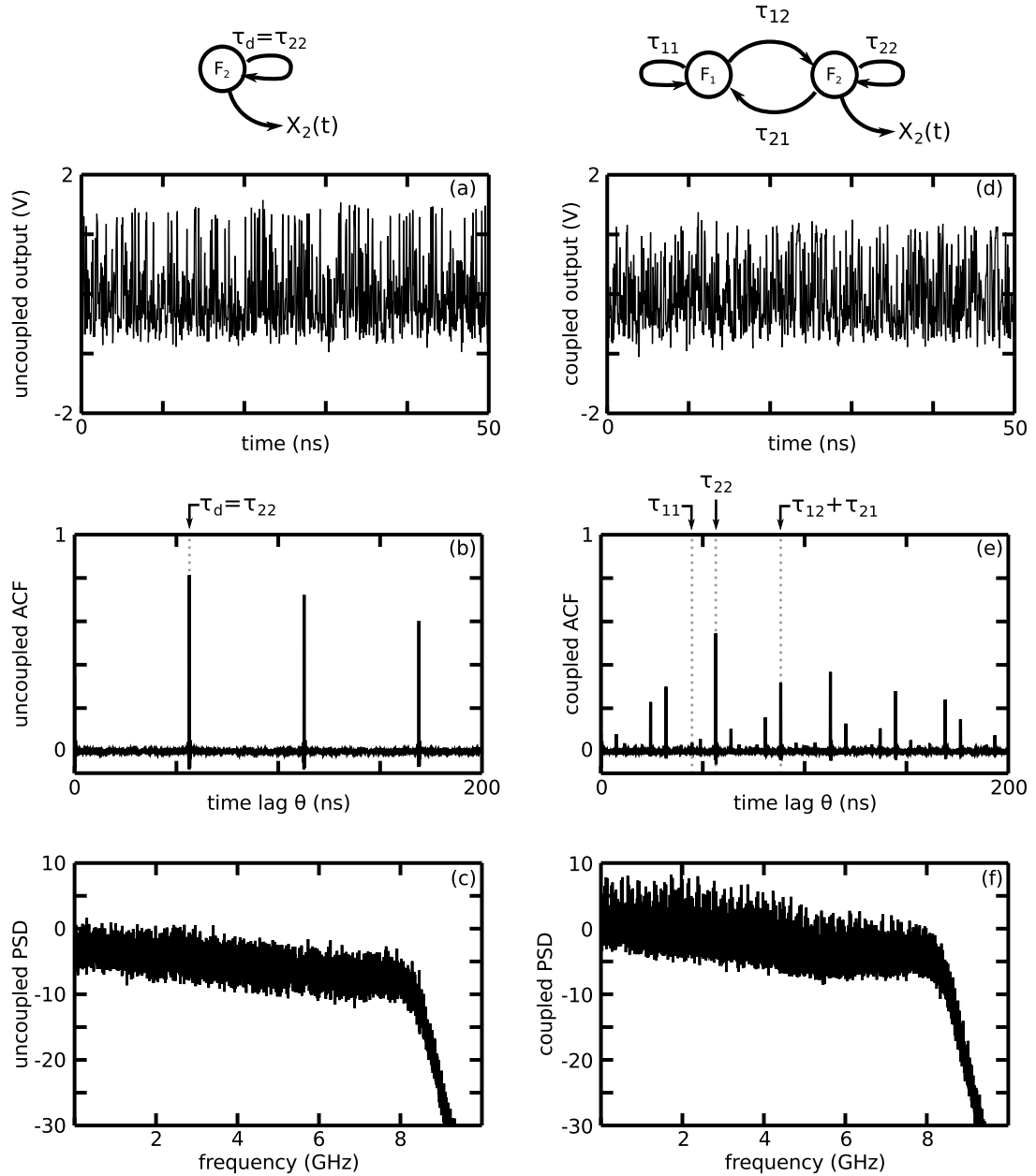


**Figure 4.2: Comparing the dynamics of a single OEO and two coupled OEOs.** The experimental (a) time series, (b) ACF, and (c) power spectral density (PSD) of a single OEO with adjustable parameters  $\gamma = 5$ ,  $\Phi = -0.08\pi$ , and  $\tau_d = 56.4$  ns. These should be compared to the experimental (d) time series, (e) ACF, and (f) PSD generated by two coupled OEOs with adjustable parameters of the two coupled OEOs are  $\gamma_1 = \gamma_2 = 5$ ,  $(\Phi_1, \Phi_2) = (0, -0.08\pi)$ ,  $c_{12} = c_{21} = 1.00$ ,  $\tau_{11} = 44.7$  ns,  $\tau_{22} = 56.4$  ns, and  $\tau_{12} + \tau_{21} = 88.3$  ns. Note that in both cases I measure dynamics of OEO<sub>2</sub>, and the PSD incorporates an 8 MHz median filter.

linear MZM) and allow the dynamics of the two nodes to evolve while fully coupled ( $c_{12} = c_{21} = 1$ ). I record representative time series (13.1  $\mu\text{s}$  of data at 40 GSa/s) of the dynamics after all transients have died away. Then, using a variable optical attenuator placed along one of the two links connecting the nodes, I successively decrease the effective coupling strength in steps of  $\sim 10\%$  and record representative time series for each step. I then calculate the ACF and extract the TDSs at various time lags in a post-processing stage. Note that these measurements could also be done realistically in real time as the network changes, assuming that these changes are slow compared to the length of the acquired time series.

Figure 4.3 shows representative time series from  $\text{OEO}_2$  with  $(\Phi_1, \Phi_2) = (0, -0.08\pi)$  for three different values of  $c_{12}$  (the coupling strength along the link that is on the input of this node), with  $c_{21} = 1$  (the coupling strength along the output link). Only 50 ns portions of the time series are shown so that the fast timescale fluctuations can be seen. There are no noticeable differences in the time series of the chaotic dynamics as changes are made to the network parameters. Even the maximum and minimum signal amplitudes (taken from the entire 13.1  $\mu\text{s}$  of data, denoted with red dashed lines) have only minor changes.

Figure 4.4, on the other hand, shows the ACFs for these same time series. Here, I show 150 ns portions so that the features at time lags  $\tau_{11}$ ,  $\tau_{22}$ , and  $\tau_{12} + \tau_{21}$  are visible. Viewed this way, it is easy to discern visually differences in the correlation properties of the dynamics due to the different coupling strengths. Most notably, as  $c_{21}$  increases the ACF transitions from having TDSs only at multiples of  $\tau_{22}$ , the self-feedback time of the OEO being measured, to having peaks at several different time lags. For example, when  $c_{12} = 0$ , the TDSs at  $\tau_{\text{other}}$  and  $\tau_{\text{coupling}}$  are both zero, which they must because  $\text{OEO}_2$  is isolated. As  $c_{21}$  increases, the TDSs at  $\tau_{\text{other}}$  and  $\tau_{\text{coupling}}$  also increase from zero. However, the TDS at  $\tau_{\text{self}}$  decreases as  $c_{12}$  increases and the dynamics from

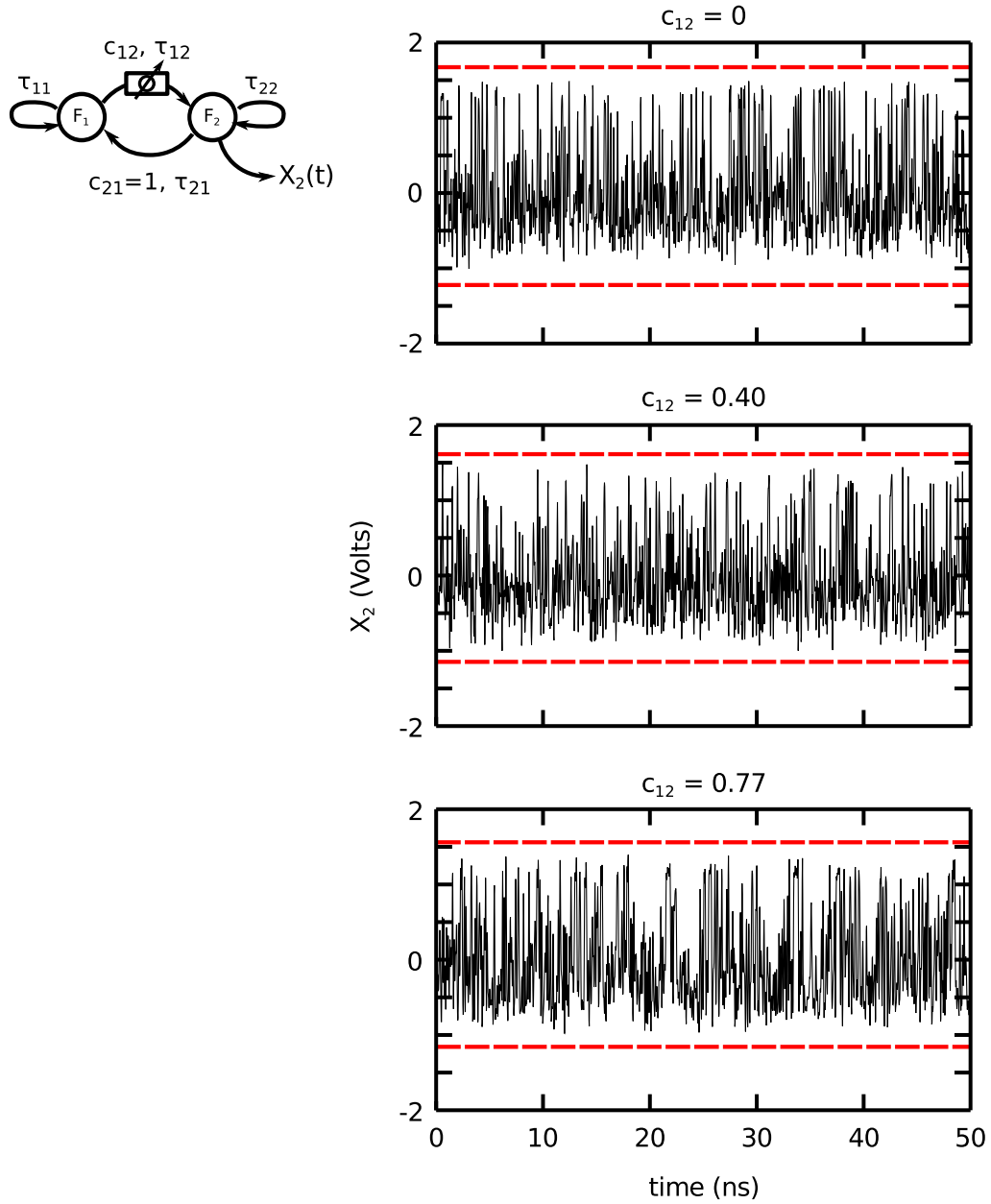


**Figure 4.3: Experimental time series as the input coupling strength varies.** The adjustable parameters are  $\gamma_1 = \gamma_2 = 5$ ,  $(\Phi_1, \Phi_2) = (0, -0.08\pi)$ ,  $c_{21} = 1.00$ , and (a)  $c_{12} = 0.00$ , (b)  $c_{12} = 0.40$ , and (c)  $c_{12} = 0.77$ . The red horizontal lines correspond to the global maximum and minimum signal amplitudes over the entire 13.1  $\mu s$ .

OEO<sub>1</sub> begin to influence that of OEO<sub>2</sub>. While the correlation properties change as the coupling strength is varied, I do not see any bifurcations to other attractors, which implies that multistability is not an issue for this scheme.

In Fig. 4.5, I show how the correlation properties of OEO<sub>2</sub> change as the coupling strength on the output link ( $c_{21}$ ) is varied, while  $c_{12} = 1$ . As with the previous case, the TDS at  $\tau_{12} + \tau_{21}$  starts at zero when  $c_{21} = 0$ , and grows as  $c_{21}$  is increased. In this case, however, OEO<sub>2</sub> is never completely isolated, so the TDSs at both  $\tau_{\text{self}}$  and  $\tau_{\text{other}}$  are nonzero for all values of  $c_{21}$ . In addition, these TDSs have the opposite behavior from the previous case: the TDS at  $\tau_{\text{self}}$  ( $\tau_{\text{other}}$ ) increases (decreases) as  $c_{21}$  increases. It is also important to note that these TDSs not only experience a change in a different direction, but they also change less than they did when the coupling on the input was varied. This seems reasonable because the effect of changing the output coupling only reaches OEO<sub>2</sub> after passing through OEO<sub>1</sub>, making link<sub>21</sub> more “distant” than link<sub>12</sub>.

The changes in correlation properties can be more easily viewed by plotting the TDS at each of the three relevant timescales as a function of the varying coupling strength of one of the links. This is shown in Fig. 4.6, where the blue (red) curves correspond to the situation where  $c_{21}$  ( $c_{12}$ ) varies with  $c_{12} = 1$  ( $c_{21} = 1$ ). The data characterizing the dynamics of both OEOs are shown. Due to the parameter mismatch between the nodes, the actual values of the TDSs are different, but the trends are similar. Note that, for OEO<sub>1</sub>, the blue curve corresponds to changing the input link, while the red curve corresponds to changing the output link. The situation is reversed for OEO<sub>2</sub>. From these plots one can see that the TDSs at  $\tau_{\text{self}}$  and  $\tau_{\text{other}}$  are sensitive to which link is being attenuated, while the TDS at  $\tau_{\text{coupling}}$  exhibit similar behavior regardless of the location of the attenuator.

To determine whether these qualitative behaviors can be general, I select new values for  $\Phi_1$  and  $\Phi_2$  ( $0.08\pi$  and  $-0.06\pi$ , respectively) and repeat the experiment. The

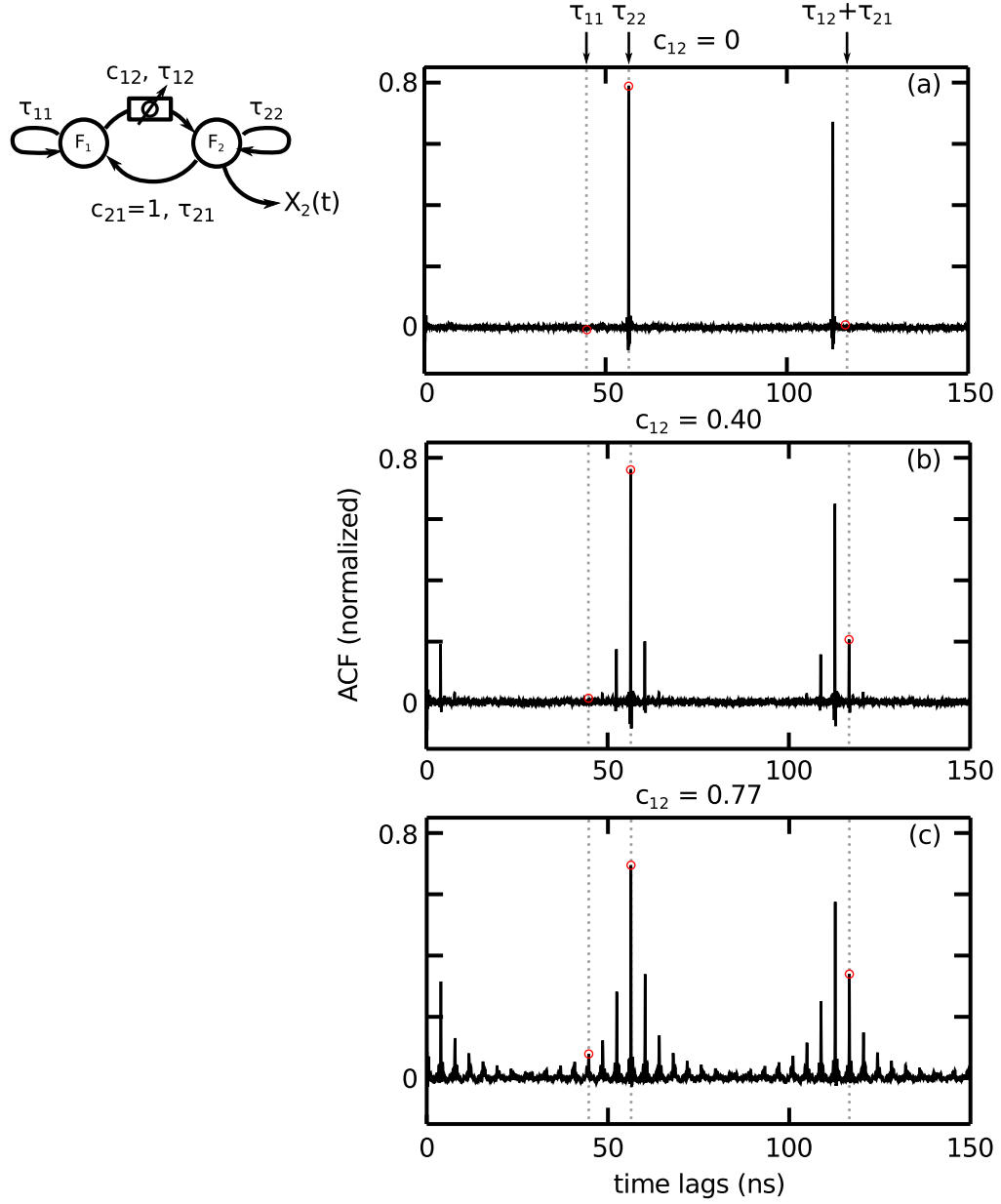


**Figure 4.4: Experimental ACFs as the input coupling strength varies.** The adjustable parameters are  $\gamma_1 = \gamma_2 = 5$ ,  $(\Phi_1, \Phi_2) = (0, -0.08\pi)$ ,  $c_{21} = 1.00$ , and (a)  $c_{12} = 0.00$ , (b)  $c_{12} = 0.40$ , and (c)  $c_{12} = 0.77$ . The red circles correspond to the TDSs at  $\tau_{11}$ ,  $\tau_{22}$ , and  $\tau_{12} + \tau_{21}$ .

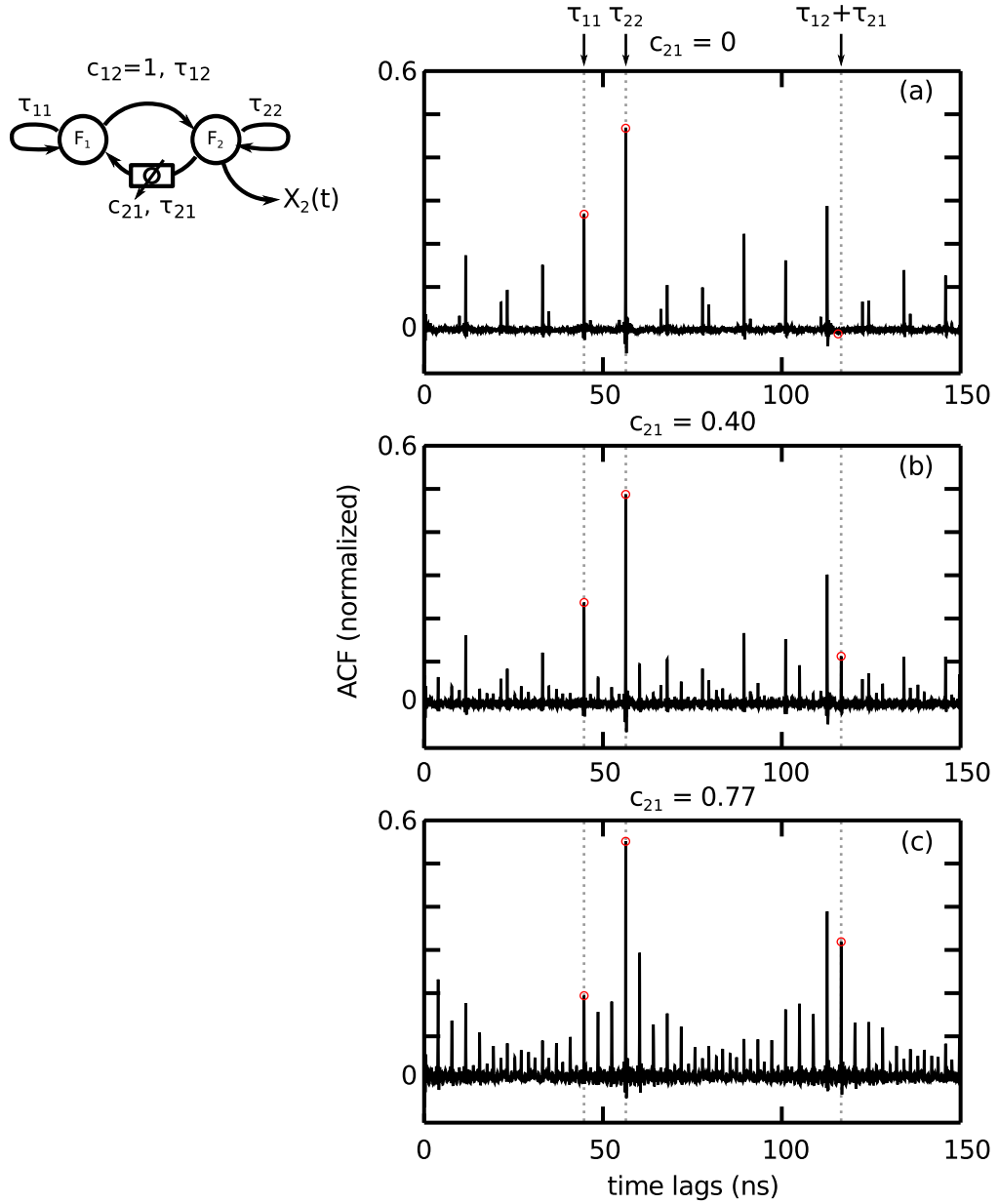


**Figure 4.5: Experimental ACFs as the output coupling strength varies.** The adjustable parameters are  $\gamma_1 = \gamma_2 = 5$ ,  $(\Phi_1, \Phi_2) = (0, -0.08\pi)$ ,  $c_{12} = 1.00$ , and (a)  $c_{21} = 0.00$ , (b)  $c_{21} = 0.40$ , and (c)  $c_{21} = 0.77$ . The red circles correspond to the TDSs at  $\tau_{11}$ ,  $\tau_{22}$ , and  $\tau_{12} + \tau_{21}$ .

TDSs as a function of coupling strength for each of the two links are shown in Fig. 4.7. As with the first example, the magnitude of the TDS at  $\tau_{\text{self}}$  decreases as the coupling strength on the input link increases. Also, when the coupling strength of the output link is changed, the TDS at  $\tau_{\text{self}}$  changes by a smaller amount. However, while the TDSs at  $\tau_{\text{coupling}}$  start and end at the same values, their behavior at intermediate coupling strengths is different for each link.

Quantitatively, I calculate difference between the TDSs at each of the three delay times (rescaled by  $\delta_{\text{TDS}}$ ) when the OEOs are fully coupled ( $c_{12} = c_{21} = 1$ ) and when one of the links is fully attenuated ( $c_{12} = 0$  with  $c_{21} = 1$ , and  $c_{12} = 1$  with  $c_{21} = 0$ ). The results are shown in Tables 4.3 and 4.4. For the experiment with  $(\Phi_1, \Phi_2) = (0, -0.08\pi)$ , the values of  $\tilde{\Delta}\text{TDS}$  at  $\tau_{\text{coupling}}$  are equal, within the experimental uncertainty of  $\sqrt{2}$ , regardless of which link is attenuated and which node is measured. However, none of the other values are equal. The situation is similar for the experiment with  $(\Phi_1, \Phi_2) = (0.08\pi, -0.06\pi)$ , where only the values of  $\tilde{\Delta}\text{TDS}$  at  $\tau_{\text{coupling}}$  for the same node are equal. This indicates that the majority of the changes in the correlation properties are not only dependent on the precise changes in the network parameters, but also depend sensitively on the parameters of the nodes themselves. So while it seems promising that some qualitative behavior could be general, it is also clear that much of the behavior depends in a complicated way on the parameters of each node, which are different in this experimental network.

### 4.3 Using TDSs for sensing

One can use the results shown in Figs. 4.6 and 4.7 to calibrate the two-node network for sensing changes to the coupling strength along one of the links<sup>1</sup> I illustrate how

---

<sup>1</sup>Note that this is done under the assumption that these changes are slow relative to the timescale of the dynamics. Also, the coupling is fiber-optical, and thus the changes in coupling strength cannot be brought about by the presence of an intruder, as discussed in Ch. 1.

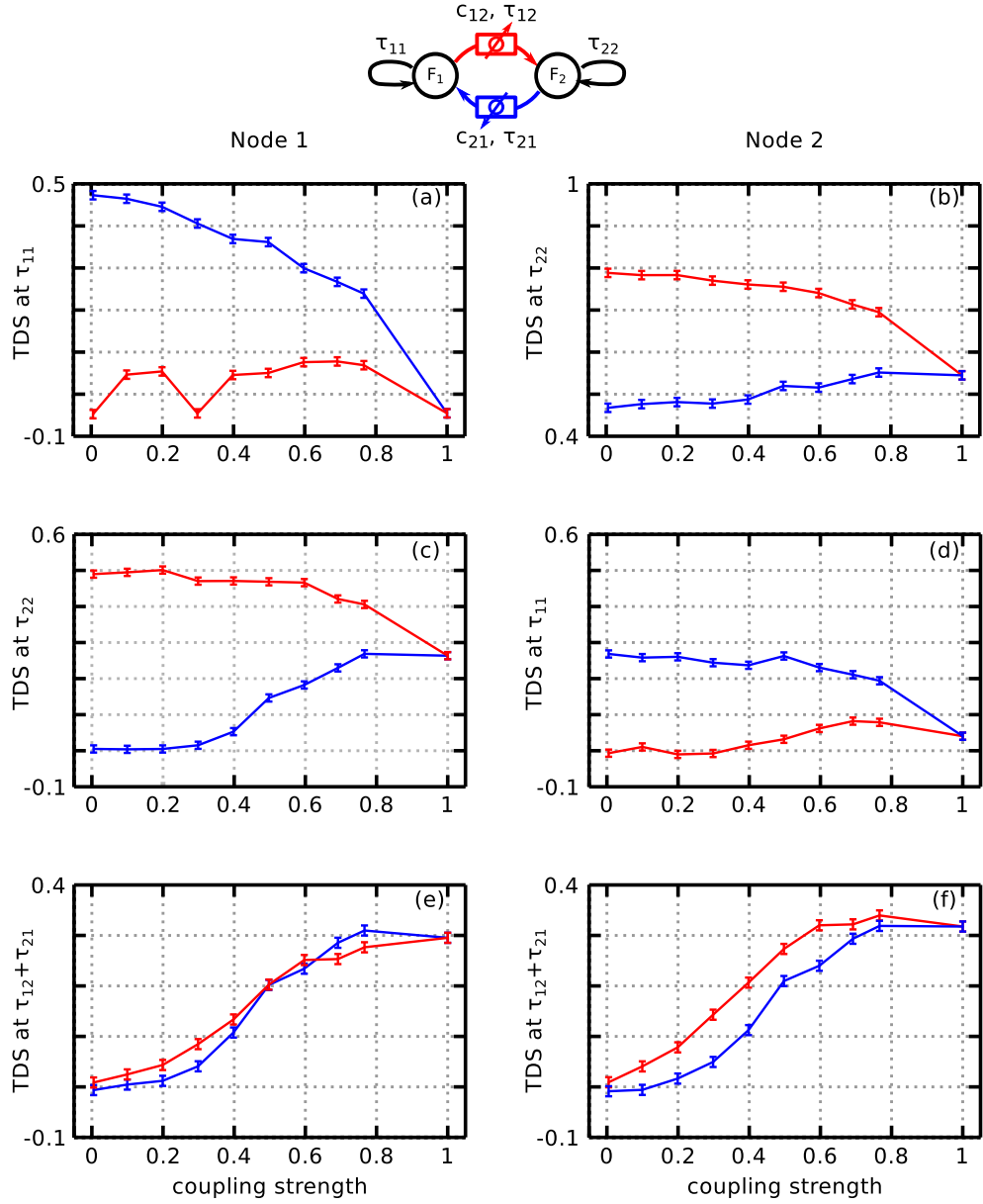


**Figure 4.6: Experiment: TDSs for  $(\Phi_1, \Phi_2) = (0, -0.08\pi)$ .** Data for both nodes is shown. The red data points correspond to  $c_{12}$  varying (with  $c_{21} = 1$ ) and the blue data points to  $c_{21}$  varying (with  $c_{12} = 1$ ). TDSs at (a,b)  $\tau_{\text{self}}$ , (c,d)  $\tau_{\text{other}}$ , and (e,f)  $\tau_{\text{coupling}}$  are shown. The errors bars represent a statistical error of 0.01, estimated with the standard deviation of several measurements of the TDSs with the same parameters. Note that the vertical scales for side-by-side plots are chosen to be the same for ease of comparison, although the maximum and minimum values may be shifted so that all of the data are displayed.

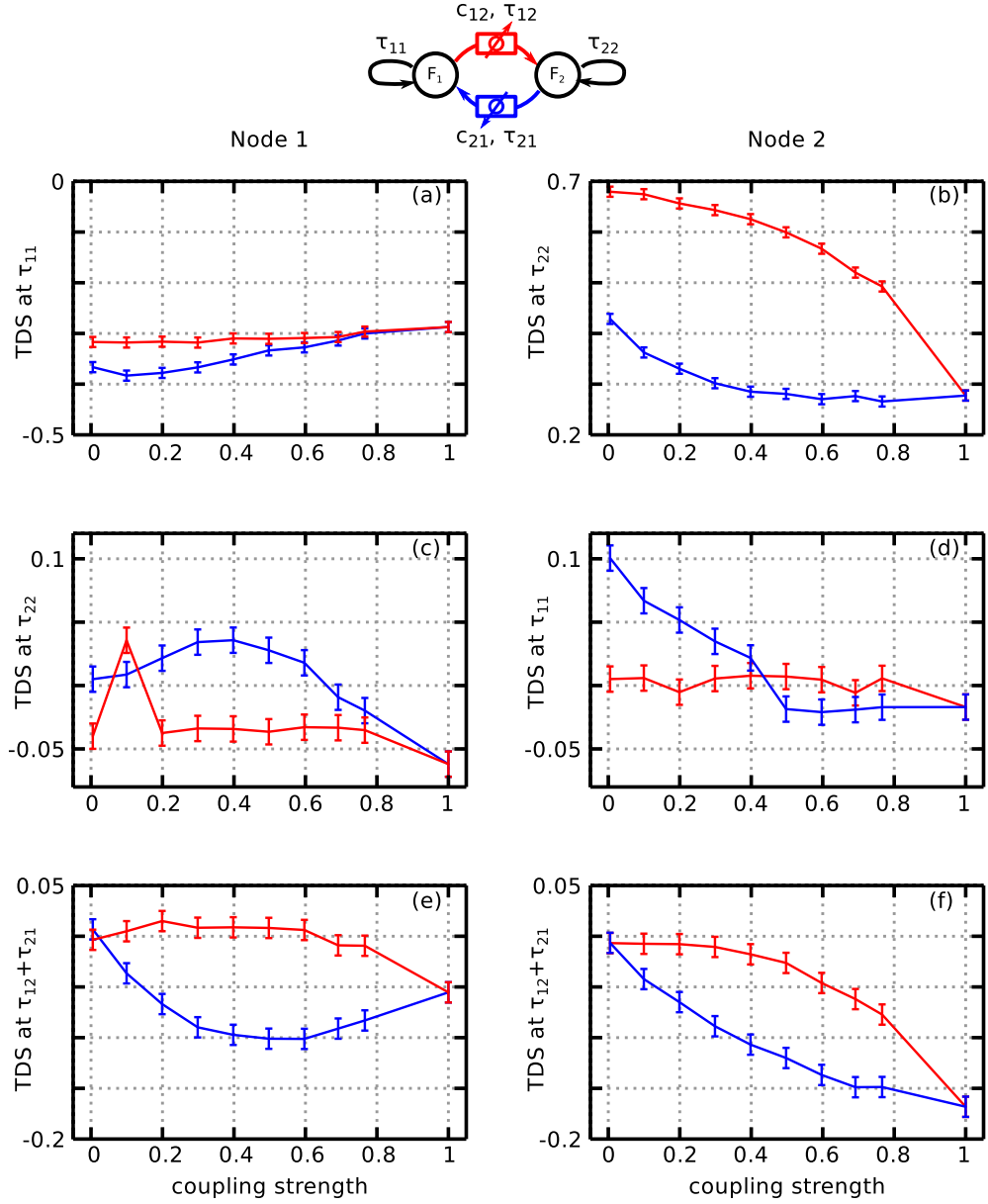


**Figure 4.7: Experiment: TDSs for  $(\Phi_1, \Phi_2) = (0.08\pi, -0.06\pi)$ .** Data for both nodes is shown. The red data points correspond to the situation where  $c_{12}$  varying (with  $c_{21} = 1$ ) and the blue data points are for  $c_{21}$  varying (with  $c_{12} = 1$ ). TDSs at (a,b)  $\tau_{\text{self}}$ , (c,d)  $\tau_{\text{other}}$ , and (e,f)  $\tau_{\text{coupling}}$  are shown. The errors bars represent a statistical error of 0.01, estimated with the standard deviation of several measurements of TDSs with the same parameters. Note that the vertical scales for side-by-side plots are chosen to be the same for ease of comparison, although the maximum and minimum values may be shifted so that all of the data is displayed.

**Table 4.3:** Changes in TDSs for  $(\Phi_1, \Phi_2) = (0, -0.08\pi)$ 

Node	Link	$\tilde{\Delta}$ TDS $\tau_{\text{self}}$	$\tilde{\Delta}$ TDS $\tau_{\text{other}}$	$\tilde{\Delta}$ TDS $\tau_{\text{coupling}}$
1	2 $\rightarrow$ 1	-52	26	30
1	1 $\rightarrow$ 2	0	-23	29
2	1 $\rightarrow$ 2	-24	5	31
2	2 $\rightarrow$ 1	8	-23	33

**Table 4.4:** Changes in TDSs for  $(\Phi_1, \Phi_2) = (0.08\pi, -0.06\pi)$ 

Node	Link	$\tilde{\Delta}$ TDS $\tau_{\text{self}}$	$\tilde{\Delta}$ TDS $\tau_{\text{other}}$	$\tilde{\Delta}$ TDS $\tau_{\text{coupling}}$
1	2 $\rightarrow$ 1	8	-7	-6
1	1 $\rightarrow$ 2	3	-2	-5
2	1 $\rightarrow$ 2	-40	-2	-16
2	2 $\rightarrow$ 1	-15	-12	-16

this works using the experiment with  $(\Phi_1, \Phi_2) = (0, -0.08\pi)$ . If the OEOs are initially fully coupled and the coupling strength along one of the links is decreased, this leads to changes in the TDSs of both OEOs, as described in the previous section. To track any changes in the coupling strength along either link, one could, for example, monitor the TDS at  $\tau_{22}$  of node 1, ignoring for the moment the many other TDSs present in the ACF. This particular TDS has a value of  $0.26 \pm 0.01$  when the network is fully coupled ( $c_{12} = c_{21} = 1$ ). If  $c_{12}$  changes, then the TDS at  $\tau_{22}$  increases, but if  $c_{21}$  changes, it decreases. Using the criterion that the TDSs have to separate (and stay separated) by an amount greater than twice their experimental uncertainty to be considered different, I require that the coupling strength of one of the links be attenuated by at least 23% ( $c = 77\%$ , which is the next highest value of the coupling strength after full coupling) in order to resolve which link was effected. Due to the fact that most of the data points are separated by roughly  $\pm 10\%$ , I take this to be my experimental uncertainty in the minimum attenuation (or maximum coupling strength) required to distinguish the af-

affected and unaffected links. (See Appendix A for details about changing the coupling strength along each link.)

Once I have determined which link has been attenuated, I approximate the value of the new coupling strength by inverting the appropriate graph in Fig. 4.6(c). However, this only works if, like as in this case, the TDS change monotonically with coupling strength. If this criterion is met, then the precision with which I determine the coupling strength depends on the slope of the inverted graph in the vicinity of the measured TDS. As one can see from Figs. 4.6 and 4.7, this can vary greatly. I therefore use the change in TDSs (rescaled by their uncertainties) as each link goes from fully open to fully blocked as a measure of how precise the coupling strength can be determined (with higher values corresponding to better precision). For the case shown in Fig. 4.6(c), those values are  $-24 \times \delta_{\text{TDS}}$  for the input link and  $5 \times \delta_{\text{TDS}}$  for the output link.

As the discussion above indicates, this method has limited applicability. First, it fails to distinguish which link is attenuated for some choices of TDSs. For example, if I choose to monitor the TDS at  $\tau_{12} + \tau_{21}$  of either node, the ranges for when  $c_{12}$  and  $c_{21}$  vary overlap, making distinguishability impossible. Second, it fails to provide a unique value for the coupling strength when behavior is non-monotonic or has a slope of zero (within experimental uncertainty). For example, if choose to monitor the TDS at  $\tau_{11}$  for node 1, then it is impossible to detect that there is a change in coupling strength when  $c_{12}$  changes.

Using these two metrics, an observer can detect changes to the network's coupling strengths by monitoring: (1) the TDS at  $\tau_{\text{other}}$  of node 1, (2) the TDS at  $\tau_{\text{self}}$  of node 2, and (3) the TDS at  $\tau_{\text{other}}$  of node 2. The network's ability to sense changes is worse for the experiment with  $(\Phi_1, \Phi_2) = (0.08\pi, -0.06\pi)$ . As shown in Fig. 4.7), each of the three TDSs at both nodes either has overlapping ranges (making distinguishability impossible), non-monotonic behavior (making determining the coupling strength

impossible), or both.

## 4.4 Using multiple TDSs for sensing

I saw in the previous section that the value of one TDS alone was not always enough to determine the two quantities that characterize the changes to the network parameters: the location of the attenuated link and the value of its new coupling strength. For example, if the TDS takes on similar values regardless of which link is altered (*i.e.*, if the ranges overlap), then it is impossible to distinguish which link is affected no matter how great the change in coupling strength. Or, if the TDS undergoes a non-monotonic change, then the coupling strength is also impossible to determine since one value of the TDS corresponds to multiple values of the coupling strength.

Because it is two quantities I want to determine, however, it is natural to extend the number of TDSs I rely on to determine the desired information from one to two. This idea is best illustrated graphically. Figure 4.8 shows the data from the experiment with  $(\Phi_1, \Phi_2) = (0, -0.08\pi)$ , where I use a three-dimensional plot to show the relationship between the values of two TDSs for given coupling strengths,  $c_{12}$  and  $c_{21}$ . Viewed in this way, changing the coupling strength from 0 to 1 along one of the links traces out a “strand” in the three dimensional space. (Due to experimental uncertainty, this curve actually has a finite volume.) Changing the coupling strength along the other link produces a strand that starts at the same location as the first strand, but takes a different path through the TDS<sub>1</sub>-TDS<sub>2</sub>-coupling strength space.

An observer using this network to sense changes in coupling strengths would only have knowledge of the TDSs measured. The measured TDSs would then need to be compared to the projection of the strands in the TDS<sub>1</sub>-TDS<sub>2</sub> plane, shown in Fig. 4.9, to determine if any of the links have been attenuated, and, if so, by how much. Due

to the fact that the strands (and their projections) must start at the same location and have some experimental uncertainty, there always exists a minimum change in coupling strength below which it is impossible to determine which of the two links was attenuated. If the attenuation is great enough that the affected link can be determined, then it is possible to determine the approximate coupling strength of the link (with varying precision) by inverting the graph with the largest change in TDS.

This method is just a higher-dimensional version of what I discussed in the previous section, where Figs. 4.6(a-f) are projections of the strands onto the appropriate TDS-coupling strength plane. Expanding to higher dimensions can increase the sensing capabilities of the network by circumventing issues caused by overlapping ranges. For example, with these nodal parameters, only three of the six sensing scenarios can distinguish link location and approximate coupling strength using one TDS. Using two TDSs, all six possible combinations of TDSs provide this information, as can be seen by the separation of the projection of the strands in Fig. 4.9.

For the experiment with  $(\Phi_1, \Phi_2) = (0.08\pi, -0.06\pi)$ , I see that sensing with only one TDS is impossible for each of the six scenarios shown. Applying the method with two TDSs helps to alleviate some of the issues, as shown in Figs. 4.10 and 4.11. With the higher-dimensional method, sensing is now possible for two of the six scenarios for attenuations greater than 40% (TDSs at  $\tau_{\text{self}}$  and  $\tau_{\text{coupling}}$  for (1) node 1 and (2) node 2), and four of the six for attenuations greater than 60% (node 2 TDSs at (3)  $\tau_{\text{self}}$  and  $\tau_{\text{other}}$  and (4)  $\tau_{\text{other}}$  and  $\tau_{\text{coupling}}$ ).

## 4.5 General sensing method

In the previous sections I discuss two ways to use TDSs to calibrate a two-node network so that it can sense changes in the network parameters (*i.e.*, which link is attenuated

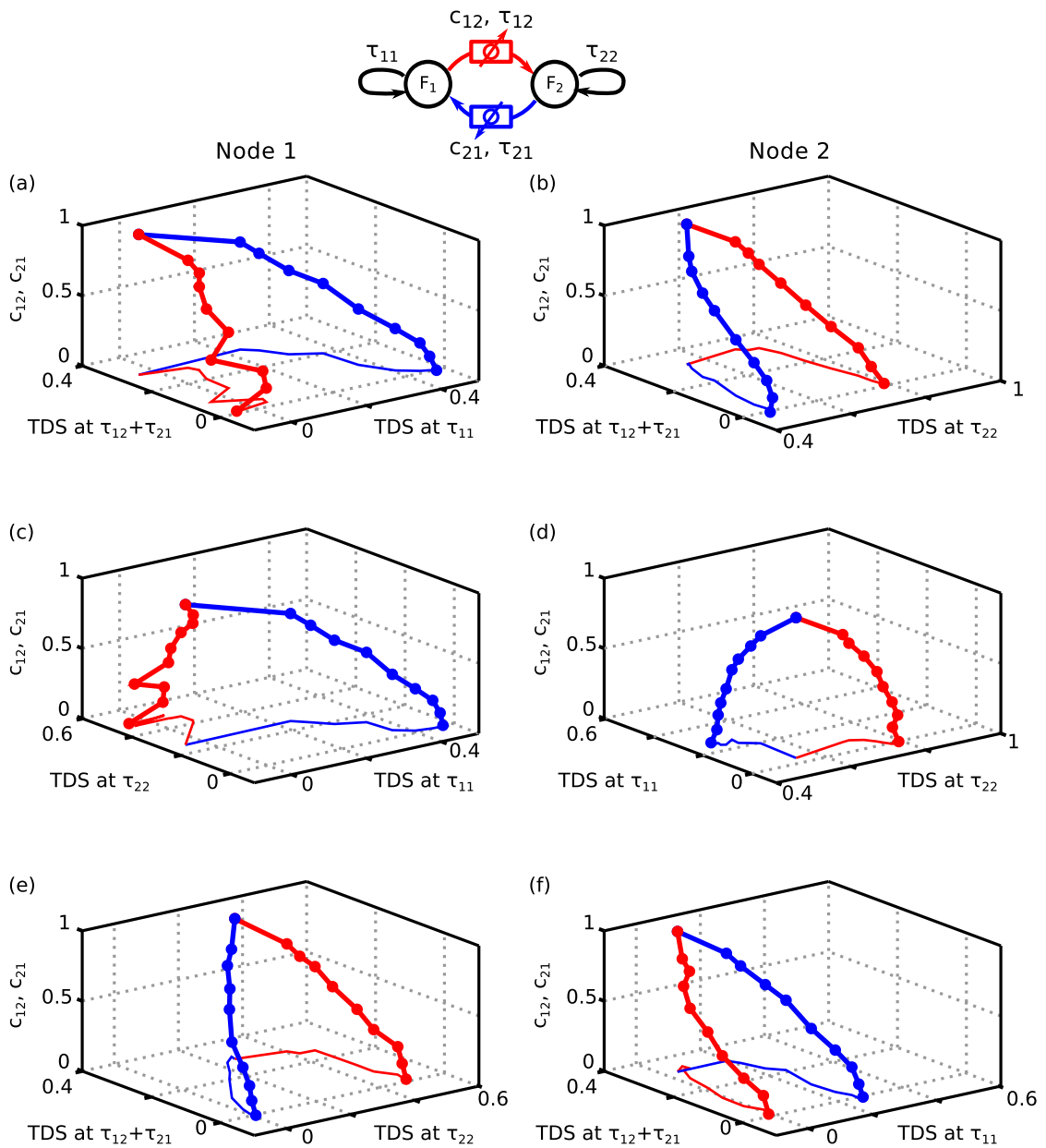


**Figure 4.8: Experiment: Strands in TDS-coupling strength space.** The TDSs were taken from the experiment with  $(\Phi_1, \Phi_2) = (0, -0.08\pi)$  and  $c_{12}$  (red) and  $c_{21}$  (blue) varied from 0 to 1. The projections of the strands onto the TDS plane are also shown.

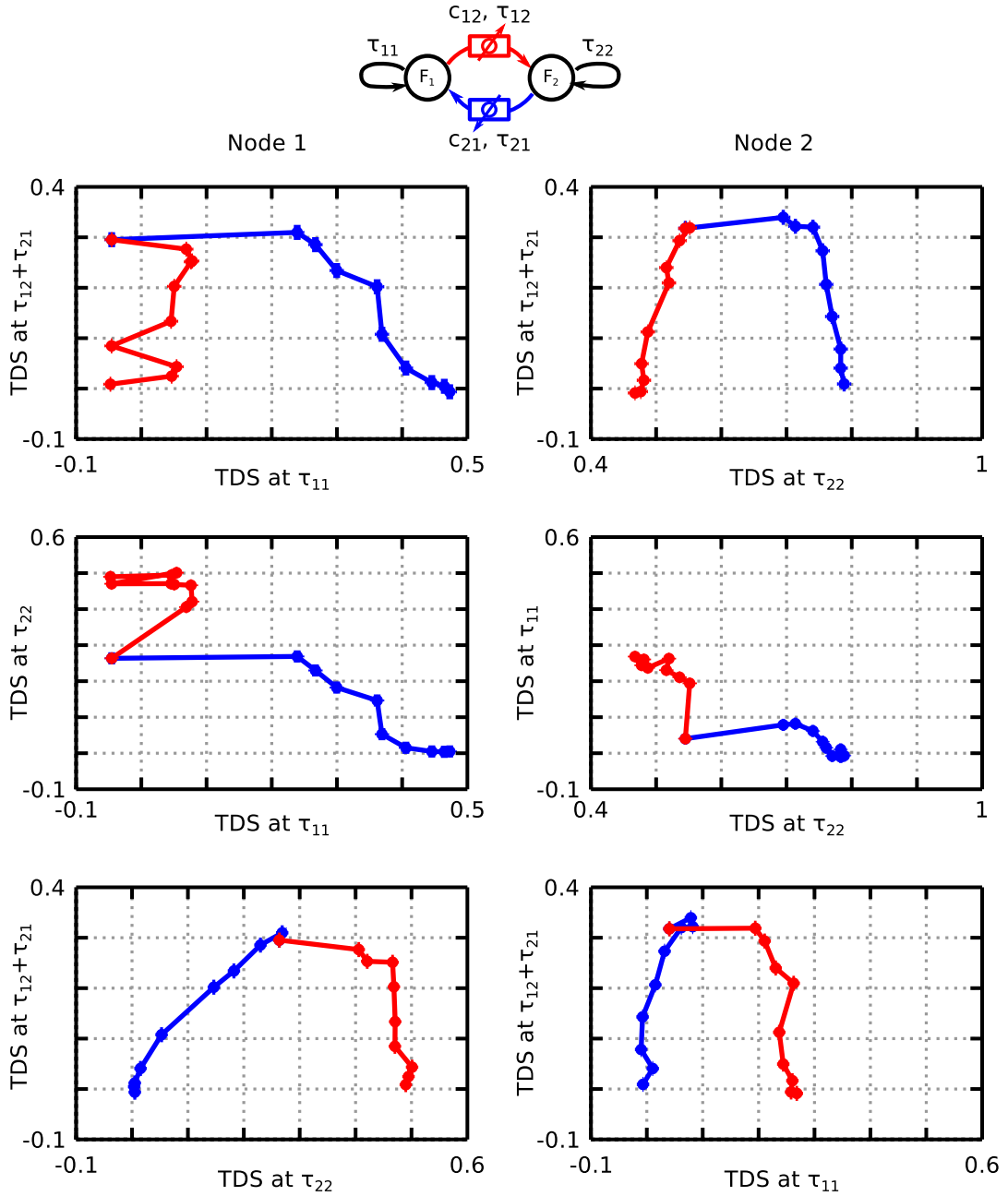


**Figure 4.9: Experiment: Projection of strands in  $TDS_1$ - $TDS_2$  plane.** The TDSs were taken from the experiment with  $(\Phi_1, \Phi_2) = (0, -0.08\pi)$  and  $c_{12}$  (red) and  $c_{21}$  (blue) varied from 0 to 1. The minimum attenuation necessary to distinguish the links (if it exists) is approximated by the first value of the coupling strength were the projections are distinct (taking into account experimental uncertainty, shown with error bars).

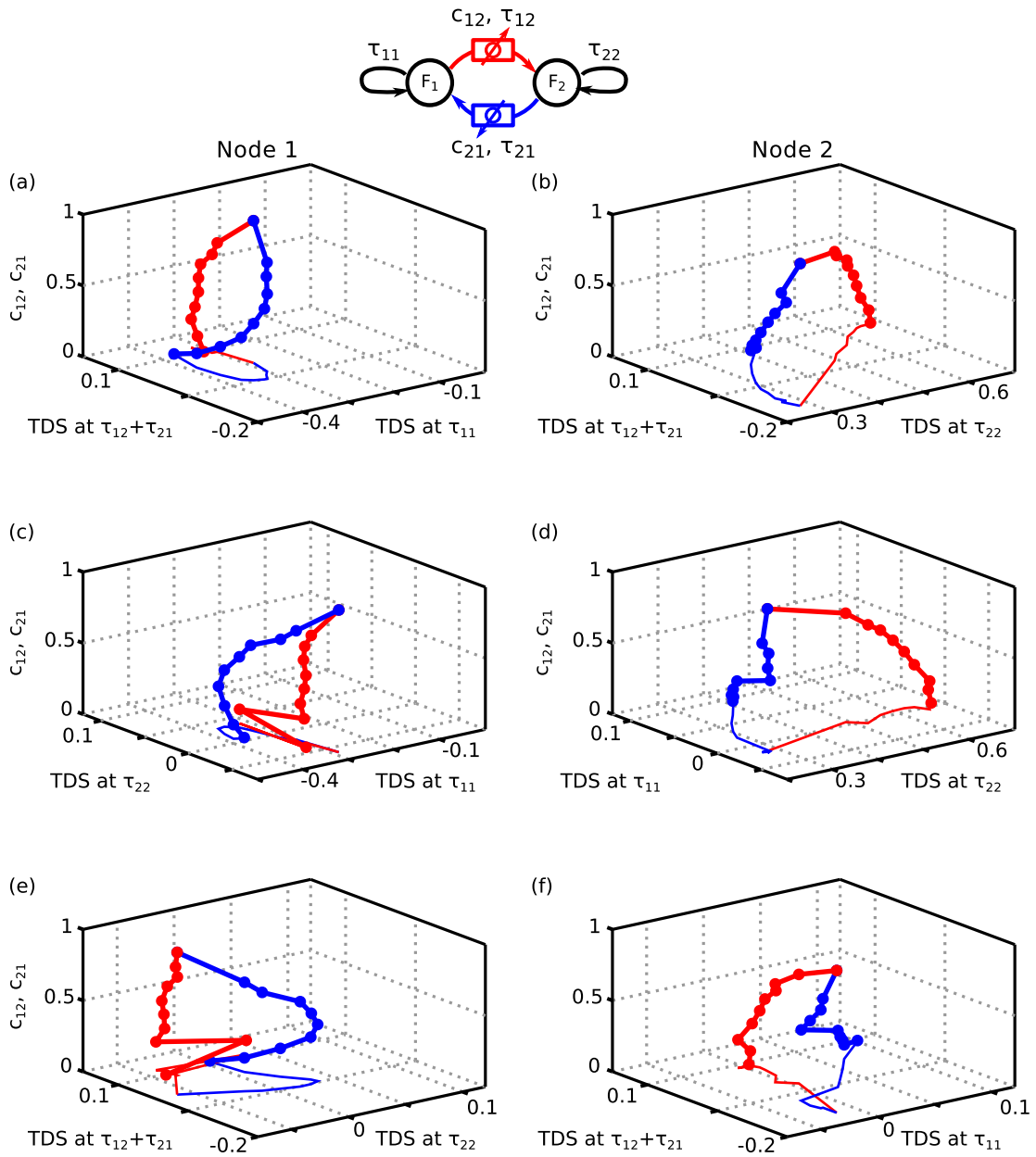


**Figure 4.10: Experiment: Strands in TDS-coupling strength space.** The TDSs were taken from the experiment with  $(\Phi_1, \Phi_2) = (0.08\pi, -0.06\pi)$  and  $c_{12}$  (red) and  $c_{21}$  (blue) varied from 0 to 1. The projections of the strands onto the TDS plane are also shown.

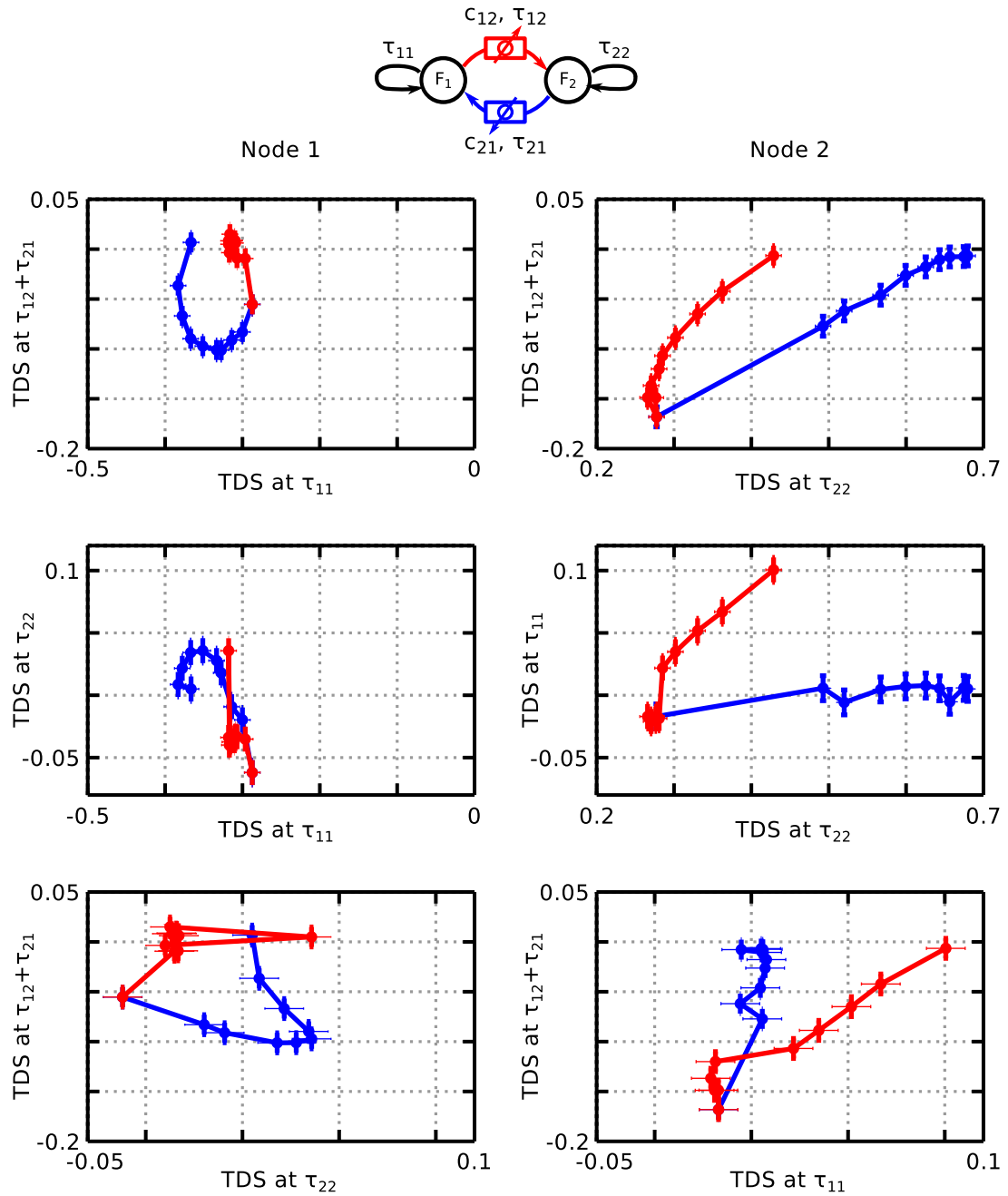


**Figure 4.11: Experiment: Projection of strands in  $TDS_1$ - $TDS_2$  plane.** The TDSs were taken from the experiment with  $(\Phi_1, \Phi_2) = (0.08\pi, -0.06\pi)$  and  $c_{12}$  (red) and  $c_{21}$  (blue) varied from 0 to 1. The minimum attenuation necessary to distinguish the links (if it exists) is approximated by the first value of the coupling strength where the projections are distinct (taking into account experimental uncertainty, shown with error bars).

and by how much) for sufficiently large changes in coupling strength. These two schemes can be thought of as one- and two-dimensional versions of a more general sensing method: To calibrate the network,  $D$  different “observables” are monitored as the coupling strength along each of the  $L$  links is changed from its minimum to its maximum value. Here, I define an observable to be any number that quantifies some aspect of a single time series. After proper calibration, these same  $D$  observables are continually monitored and compared against the calibration to sense any potential changes in network parameters. The measured observables lie closest to the projection of the strand that corresponds to the attenuated link. The coupling strength is then determined from the height of the strand at the values of the measured observables. A cartoon illustration of this method shown in Fig. 4.12.

As I saw in the previous sections, extending to higher values of  $D$  can improve the network’s sensing capabilities by making the links more distinguishable, but at the expense of added complexity of the analysis and decreased ease of visualization. It is important to note, however, that all of the observables are taken from the same time series, so the  $D$ -dimensional method still only relies on limited dynamical measurements (and  $D$  calculations) and can still be implemented with high-speed dynamical systems.

I find experimentally that the TDSs at  $\tau_{\text{self}}$ ,  $\tau_{\text{other}}$ , and  $\tau_{\text{coupling}}$  can be used as observables in this sensing method with mixed success depending on the parameters of the nodes in the network. In principle, any quantity that can be calculated from a single time series and that changes with the properties of the network can be used. For example, one could use the largest  $D$  TDSs, rather than those that occur at these three “special” time lags, as observables. Alternatively, one could integrate the absolute value of the ACF in either the vicinity of the TDS or over its entire extent, which would effectively incorporate the magnitude of all TDSs into one observable. Initial

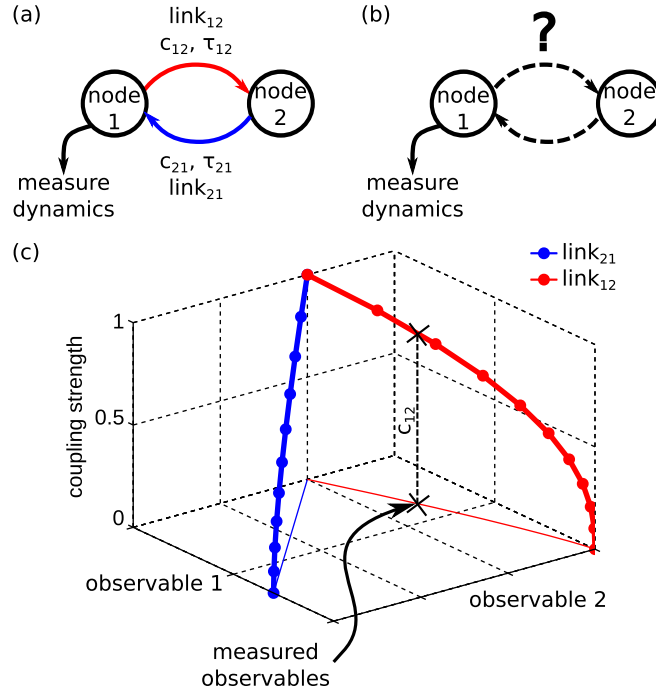


**Figure 4.12: Illustration of sensing method with a two-node network.** (a) The coupling strength along each link is varied from 0 to 1 and representative time series of the dynamics of one node are recorded. This serves to calibrate the network for sensing. (b) The dynamics of the same node are recorded as an unknown change to one of the network parameters is made. (c) The observables extracted from the measured time series are compared against the calibration and used to determine link location and coupling strength.

investigations show, however, that in the cases where sensing with one or two TDSs failed, none of these new choices of observables were successful. Other examples of observables include: maximum and minimum signal amplitudes, permutation entropy [50], and statistical complexity [51, 52]. I choose to use TDSs as observables because, for my experimental system, I find that they are more sensitive to the network's parameters and more robust to experimental noise than the maximum and minimum signal amplitudes, as shown in Fig. 4.13, and are much faster to compute than permutation entropy and statistical complexity. An example of an analysis using permutation entropies as observables is shown in Appendix B.

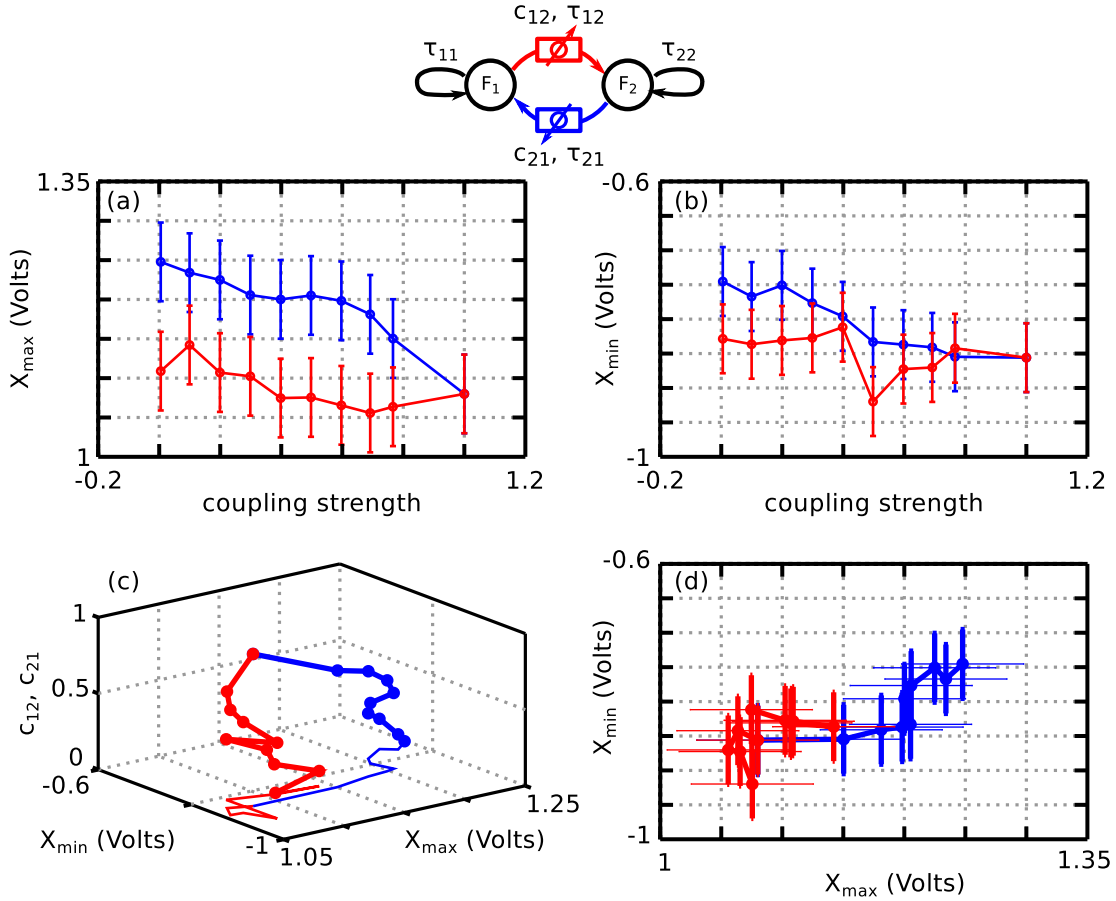


**Figure 4.13: Experiment: Maximum and minimum signal amplitudes.** The (a) maximum and (b) minimum signal amplitudes were taken from the experiment with  $(\Phi_1, \Phi_2) = (0, -0.08\pi)$  and  $c_{12}$  (red) and  $c_{21}$  (blue) varied from 0 to 1. The (c) strands in observable-coupling strength space and (d) projections onto the observables plane are also shown. Note that the changes relative to the experimental measurement uncertainty are much lower than in the cases where TDSs are used as observables.

My proof of principle experiment is conducted with a two-node network with two links. The same method can be used to analyze a network with a higher number of nodes and links. For example, with  $D = 2$ , the number of strands in the observable-coupling strength space would be equal  $L$ , the number of links. Increasing  $L$  makes the observables-coupling strength space more crowded, which can be alleviated by using a higher value of  $D$ . Another potential problem is that links that are too “distant”

from the node being measured may not cause the observables to undergo statistically significant changes. This can be circumvented by acquiring time series, and hence observables, from more than one node in the network.

## 4.6 Toward optimization

While I have shown that, under appropriate conditions, my sensing method can be implemented experimentally in two-node network of OEOs, it remains unclear what choice of nodal parameters are optimal for sensing the network parameters. Even with just this simple two-node network, the parameter space for which this method can be implemented is large. In addition, the sensing capabilities depend on two metrics, the maximum coupling strength at which the links are distinguishable and the precision with which the coupling strength can be determined, which are not necessarily optimized for the same choice of nodal parameters. It is therefore difficult to answer questions like: Is it better to use nodes with the same parameter values, different parameter values, or does it depend on the parameter?

To begin to answer the question of what nodal parameters yield the best possible determination of the coupling strength, I record time series for a range of values of  $(\Phi_1, \Phi_2)$ , with all other nodal parameters held fixed. I do this with the network fully coupled ( $c_{12} = 1, c_{21} = 1$ ), one link blocked ( $c_{12} = 0, c_{21} = 1$ ), and the other link blocked ( $c_{12} = 1, c_{21} = 0$ ). I then compare how the value of each observable  $o_i$  changes (relative to its corresponding measurement uncertainty  $\delta o_i$ ) when one of the two links is blocked for each value of  $(\Phi_1, \Phi_2)$  using

$$\tilde{\Delta}o_{i,12} = \frac{o_{i,c_{12}=1,c_{21}=1} - o_{i,c_{12}=0,c_{21}=1}}{\delta o_i}, \quad (4.1)$$

$$\tilde{\Delta}o_{i,21} = \frac{o_{i,c_{12}=1,c_{21}=1} - o_{i,c_{12}=1,c_{21}=0}}{\delta o_i}. \quad (4.2)$$

In terms of precision with which the coupling strength can be determined, sensing is generally improved for larger values of  $|\tilde{\Delta}o_{i,12}| + |\tilde{\Delta}o_{i,21}|$ , which corresponds to larger changes in the observables. An example of this analysis is shown in Fig. 4.14. One can see that, for each node and all combinations of observables, the optimal operating point according to this metric is  $(\Phi_1, \Phi_2) = (0, -0.08\pi)$ . It is interesting to note that the greatest changes in observables in this (already heterogeneous) network occur for  $\Phi_1 \neq \Phi_2$ , lending credence to the idea that sensing can not only take place despite nodal heterogeneities, but might also be improved by them.

## 4.7 Summary

In this chapter, I demonstrate a proof of principle experiment of a novel sensing method with high-speed ( $> 10$  GHz) dynamical systems with non-identical nodes and non-negligible delays in the interactions. My method exploits the fact that correlation properties of the nodal dynamics in an experimental nonlinear, delayed network are sensitive to changes in the network parameters in a statistically significant and reproducible way. The TDSs, which I first introduce in Ch. 2, are one such example. I also explore ways to optimize the method by choice of parameters and observables. I find that, for the optimal choice of nodal parameters, an observer can determine which link is affected for an attenuation of roughly 20% or greater by monitoring two of the three TDSs at  $\tau_{\text{self}}$ ,  $\tau_{\text{other}}$ , and  $\tau_{\text{coupling}}$ . In addition, the maximum changes in these TDSs,

when either the input or output link to the observed node is blocked, are on the order of 10 times greater than their experimental uncertainties, making approximation of the coupling strength possible.

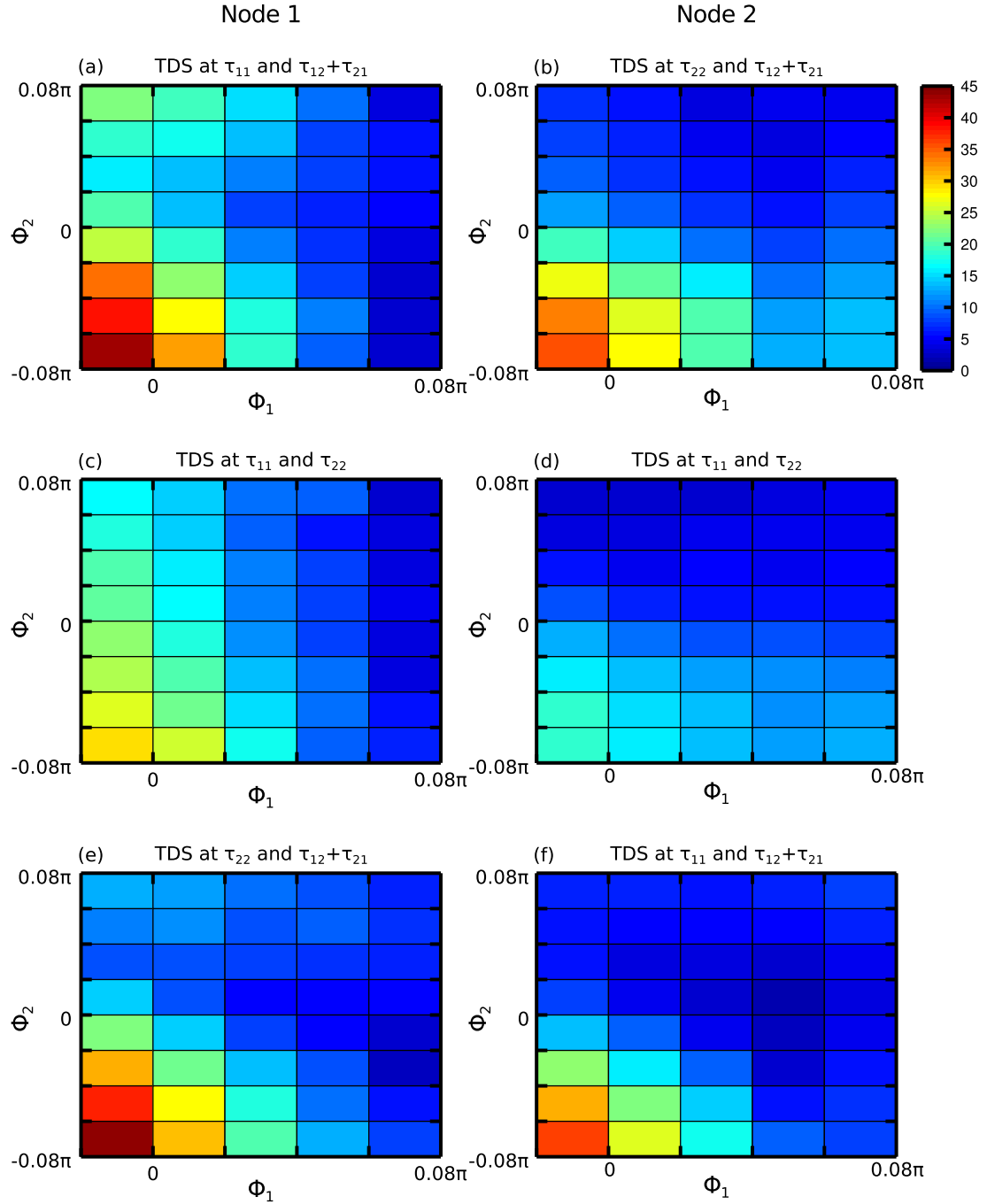


**Figure 4.14: Determining optimal parameters for sensing.** Data from both nodes using all combinations of the three TDSs as observables. For each value of  $(\Phi_1, \Phi_2)$ ,  $|\tilde{\Delta}o|$  is computed for both observables using Eqs. 4.1 and 4.2 and then averaged. Higher values (red) correspond to improved sensing performance, with respect to determining the coupling strength.

# Chapter 5

## Numerical implementation of the sensing method

In Ch. 4, I demonstrate experimentally how to calibrate a two-node network of OEOs so that an observer can sense changes to the network parameters by monitoring the dynamics of a single node. In this chapter, I confirm qualitatively my experimental findings by numerically integrating a DDE model describing the coupled OEOs. I then investigate the performance of the sensing network when the four time delays, which are originally taken to be distinct, are successively made identical. Finally, I explore the necessity of deterministic chaos as the dynamics on the nodes in my sensor network by replacing it with dynamics generated by a linear stochastic map.

To numerically integrate the DDE models describing the OEOs, I use a multi-step predictor-corrector method known as the four-point Adams-Bashforth-Moulton method, which is described in Ref. [53]. The code for the integrator I use was originally written by Dr. Damien Rontani, and I modify it to suit my purposes, with details given in Appendix C.

### 5.1 Model and integration

In Ch. 2, I introduce a DDE model for the single OEOs used in my experiments,

$$\dot{V}(t) = \Delta \{-V(t) - U(t) + F[V(t - \tau_d)]\}, \quad (5.1)$$

$$\dot{U}(t) = \Delta \epsilon V(t), \quad (5.2)$$

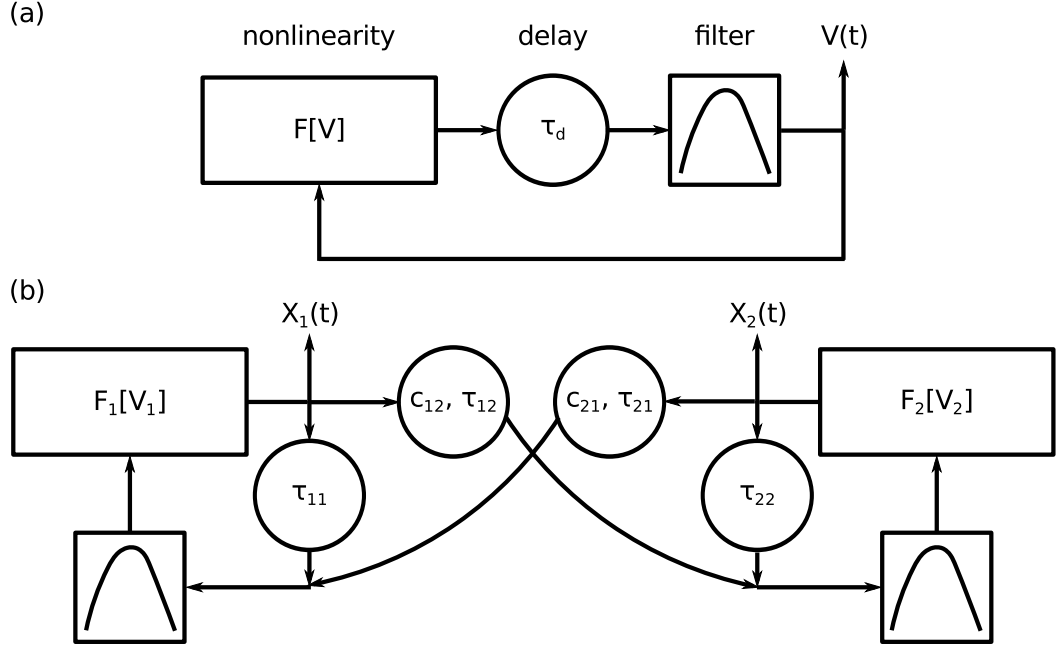


**Figure 5.1: Mathematical block diagram.** (a) Single OEO. (b) Two coupled OEOs.

where the nonlinear function  $F[V]$  is given by

$$F[V] = \frac{\gamma g}{d} \left\{ \cos^2 \left[ \Phi + d \tanh \left( \frac{V}{g} \right) \right] - \cos^2 [\Phi] \right\}. \quad (5.3)$$

Recall that  $V(t)$  denotes the voltage directly at the output of the bandpass filter, which is approximately equal to the voltage I measure in the experiments with a single OEO. Also,  $U(t)$  is introduced as an auxiliary variable to account for the integral term (due to the high-pass filter), which cannot be measured physically. A mathematical block diagram of corresponding to Eqs. 5.1 and 5.2 is shown in Fig. 5.1(a).

To determine how well my model captures the behavior of the TDSs, I integrate Eqs. 5.1 and 5.2 for a range of values of  $\Phi$ . Since many of my experimental parameters have rather large fractional uncertainties (see Table 4.1), I use a gradient descent method [54] to more precisely determine the model parameters that yield the best

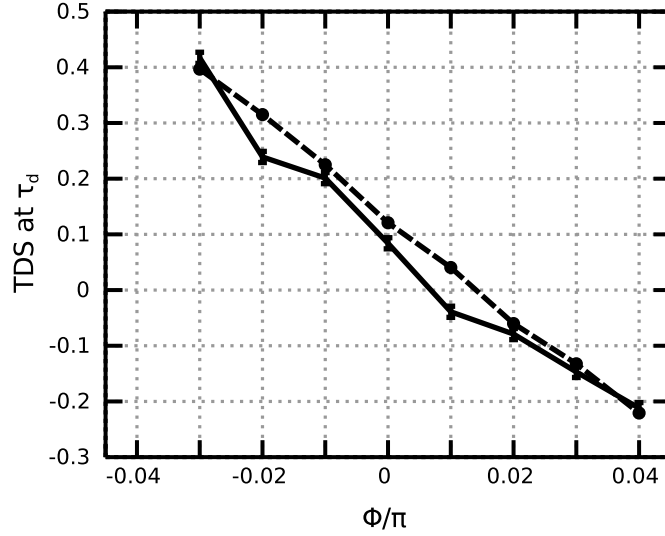


**Figure 5.2: Single OEO comparison between experiment and simulation.** The experimental TDSs at  $\tau_d$  (solid line) for  $\gamma = 5.5 \pm 0.5$ ,  $d = 1.1 \pm 0.07$ ,  $g = -0.22 \pm 0.02$  is used as an input to a gradient descent algorithm to find the parameters that yield the best agreement with the numerical TDSs at  $\tau_d$  (dashed line). The parameters obtained are  $\gamma = 5.38$ ,  $d = 1.1242$ ,  $g = -0.2188$ , which fall within the experimental uncertainty.

match between the TDSs at  $\tau_d$  in the simulation and the experiment. The results are shown in Fig. 5.2. While the trend and asymmetry about  $\Phi = 0$  are clearly similar, the average difference between the experimental and numerical TDSs is approximately  $3 \times \delta_{\text{TDS}}$ , indicating that the precise values of the TDSs cannot be matched because there is either something important is missing from the model, or an unknown systematic experimental error, or both. However, since I am mostly interested in changes in TDSs and not their absolute values, this model suffices for my purposes.

Building upon Eqs. 5.1 and 5.2, I find that the model for the two OEOs coupled in the block diagram configuration shown in Fig. 5.1(b) is given by a set of four coupled

DDEs

$$\dot{V}_1(t) = \Delta_1 \{-V_1(t) - U_1(t) + F_1[V_1(t - \tau_{11})] + c_{21}F_2[V_1(t - \tau_{21})]\}, \quad (5.4)$$

$$\dot{U}_1(t) = \Delta_1 \epsilon_1 V_1(t), \quad (5.5)$$

$$\dot{V}_2(t) = \Delta_2 \{-V_2(t) - U_2(t) + F_2[V_2(t - \tau_{22})] + c_{12}F_1[V_2(t - \tau_{12})]\}, \quad (5.6)$$

$$\dot{U}_2(t) = \Delta_2 \epsilon_2 V_2(t). \quad (5.7)$$

Here, the subscripts 1 (2) refer to the variables and parameters of OEO<sub>1</sub> (OEO<sub>2</sub>), the subscripts 11 (22) refer to parameters characterizing the link from OEO<sub>1</sub> (OEO<sub>2</sub>) to itself, and the subscripts 12 (21) refer to parameters characterizing the link from OEO<sub>1</sub> (OEO<sub>2</sub>) to OEO<sub>2</sub> (OEO<sub>1</sub>). Note that each OEO is driven by two time-delayed nonlinear feedback terms: one corresponding to the self-feedback loop, and the other corresponding to the signal coming from the nonlinearity of the other OEO, which may or may not be attenuated.

## 5.2 Proof of principle numerical simulation

To see if my sensing results from the previous chapter are captured by the model, I first numerically integrate Eqs. 5.4–5.7 with  $c_{12} = c_{21} = 1$  and calculate the ACFs of  $V_1(t)$  and  $V_2(t)$ . As described in Appendix C, the integrator uses a fixed timestep of 0.005 ns, and the IHF is a 2-ns FWHM Gaussian pulse, with an amplitude large enough to cause the system to leave the basin of attraction of the fixed point. For this simulation, I take the fixed parameters of both OEOs to be equal to the experimentally determined parameters of OEO<sub>1</sub> (given in Table 4.1). For the adjustable parameters, I take  $\gamma_1 = \gamma_2 = 5$ ,  $\Phi_1 = 0.03\pi$ ,  $\Phi_2 = 0$ , and set the time delays to be equal to their experimental counterparts. Thus, the only differences between the two OEOs are the

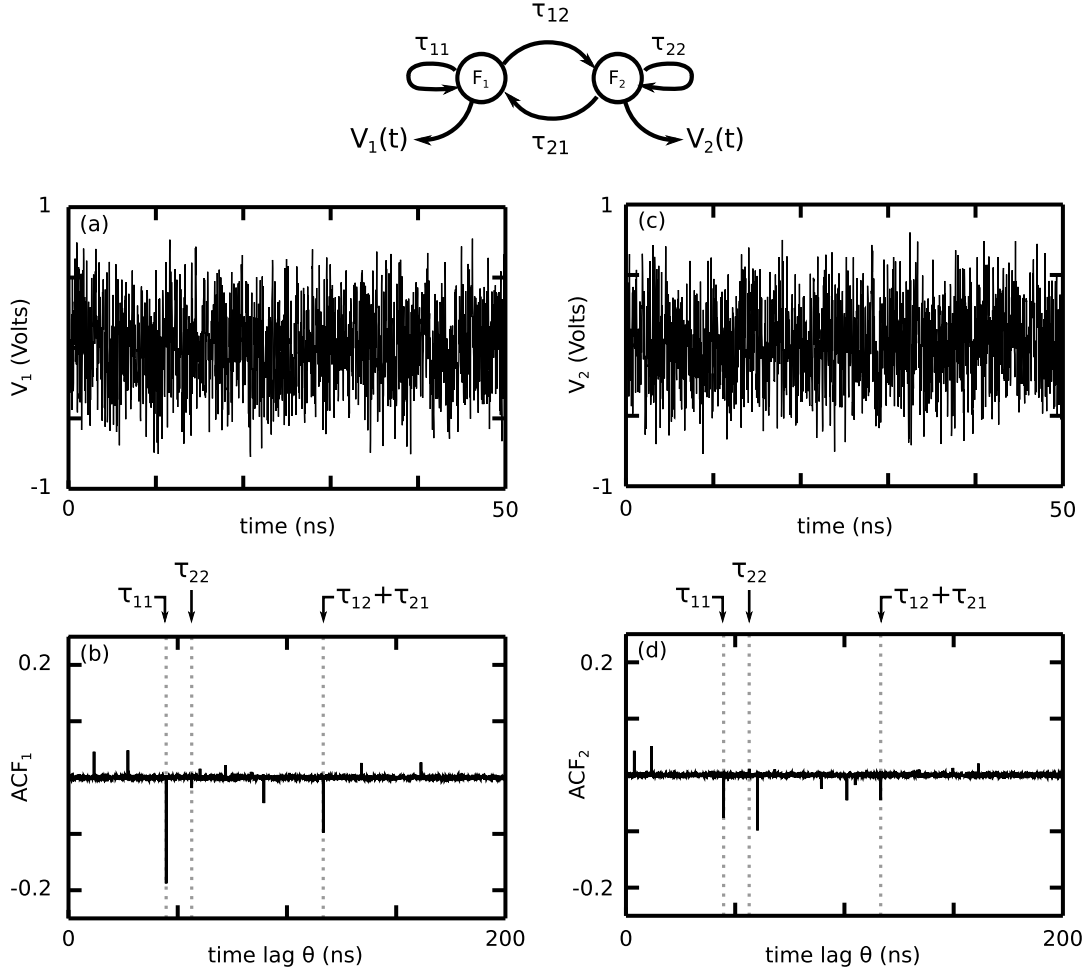


**Figure 5.3: Simulation time series and ACF of two coupled OEOs.** The numerical time series (a,c) and ACF (b,d) of two coupled OEOs with  $\gamma_{11} = \gamma_{22} = 5$ ,  $(\Phi_1, \Phi_2) = (0.03\pi, 0)$ ,  $c_{12} = c_{21} = 1.00$ ,  $\tau_{11} = 44.7$  ns,  $\tau_{22} = 56.4$  ns, and  $\tau_{12} + \tau_{21} = 116.6$  ns. The simulation is initialized with a sufficiently large amplitude pulse for the IHF. The step size is 0.005 ns, and 10  $\mu$ s of data are analyzed after discarding the first 200  $\mu$ s of data to ensure that the steady-state has been reached. Only every fifth point has been plotted to improve clarity and match the experimental sampling rate.

values of their self-feedback time delays and MZM operating points. The results of the simulation are shown in Fig. 5.3.

As with the experiment, there are sharp peaks in the ACFs at time lags equal to integer multiples of:  $\tau_{11}$ ,  $\tau_{22}$ ,  $\tau_{12} + \tau_{21}$ , and sums and differences of these three

timescales. In this case, the TDSs at  $\tau_{11}$  and  $\tau_{12} + \tau_{21}$  are much more prominent than those at  $\tau_{22}$ . This is another indication that the TDSs depend sensitively on the system's parameters, as the two OEOs only differ in their values of  $\Phi$  and  $\tau_{\text{self}}$ . It is also interesting to note that, unlike the case for the single OEO, the TDSs corresponding to the self-feedback time of each OEO are completely eliminated for  $\Phi_1 = \Phi_2 = 0$ . It is still an open question why the coupled OEOs obey this symmetry, while the single OEO does not.

I then successively decrease the coupling strength along one of the links with the other held fixed at unity, using the end of the time series at the previous step as the IHF for the next simulation. The results of the one-dimensional and two-dimensional calibrations are shown in Figs. 5.4, 5.5, and 5.6. The one-dimensional sensing method fails to differentiate between the two links and provide an approximation of the coupling strength in all cases shown in Fig. 5.4, as either the ranges of the TDSs overlap, the slope is zero, or the behavior is non-monotonic. The two-dimensional method, however, can differentiate between links for high enough attenuation in five of the six cases shown in Figs. 5.5 and 5.6. It only fails if the observer relies on the TDSs from node 2 at  $\tau_{\text{self}}$  and  $\tau_{\text{coupling}}$ , as their projections lie on top of one another, making distinguishability impossible. For all other choices of two TDSs as observables, however, the affected link can be determined for sufficiently large attenuations. Also, the maximum changes in the TDSs, when either the input or output link to the observed node is blocked, are also on the order of 10 times greater than the experimental uncertainties.

While this shows qualitative agreement for changes in the TDSs between the experiment and model, this model does not show quantitative agreement between the two. Most notably, the range of  $(\Phi_1, \Phi_2)$  values for which the dynamics have the desired correlation properties (well-defined sharp peaks superimposed on a delta function-like background) is much smaller in the simulation than in the experiment. In addition,

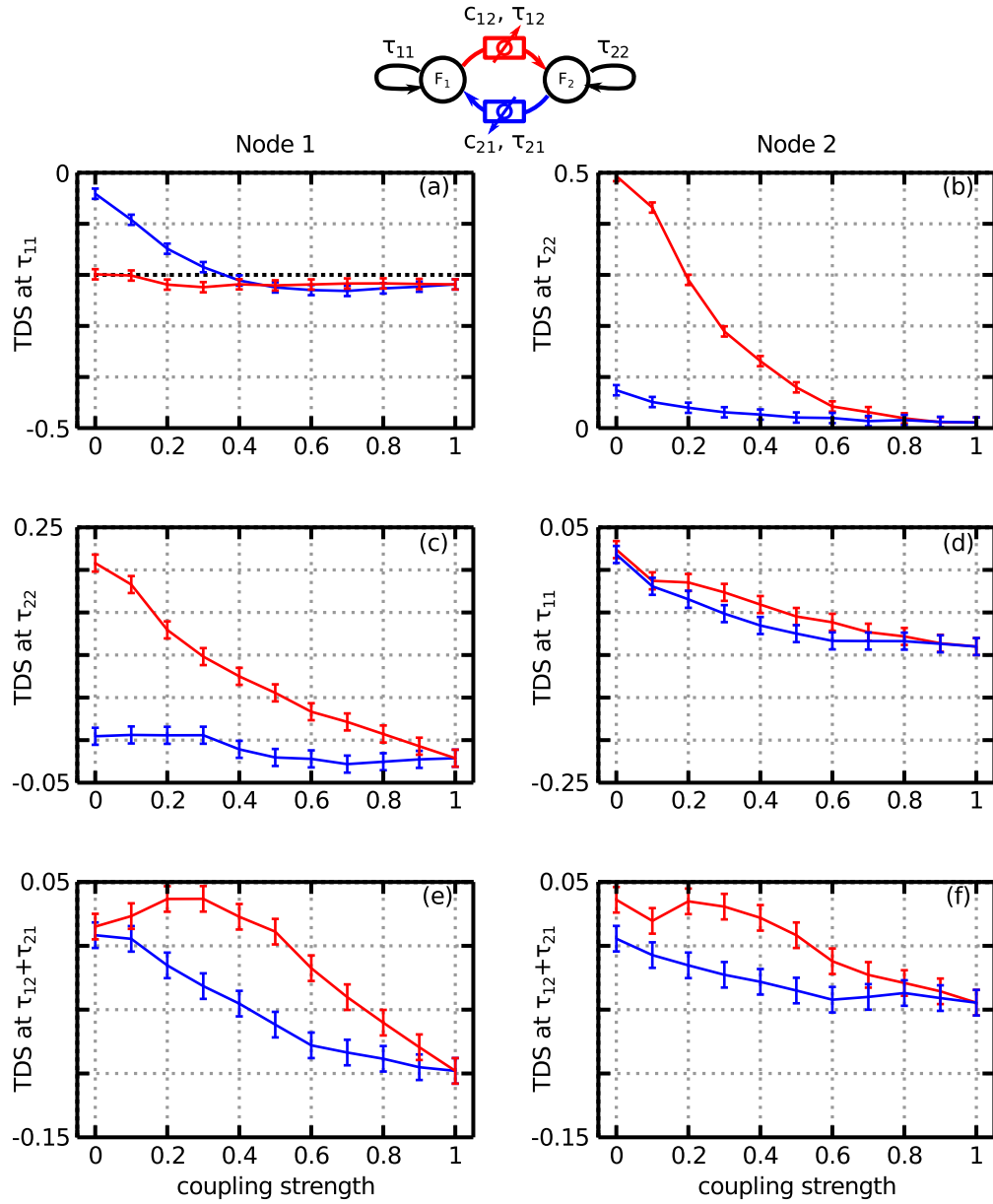


**Figure 5.4: Simulation: TDSs for  $(\Phi_1, \Phi_2) = (0.03\pi, 0)$ .** Data for both nodes is shown. The red data points correspond to  $c_{12}$  varying (with  $c_{21} = 1$ ) and the blue data points to  $c_{21}$  varying (with  $c_{12} = 1$ ). TDSs at (a,b)  $\tau_{\text{self}}$ , (c,d)  $\tau_{\text{other}}$ , and (e,f)  $\tau_{\text{coupling}}$  are shown. For consistency of comparison, the error bars represent the experimental statistical error of 0.01, which is about a factor of five greater than the estimated numerical error. Note that the vertical scales for side-by-side plots are chosen to be the same for ease of comparison, although the maximum and minimum values may be shifted so that all of the data are displayed.

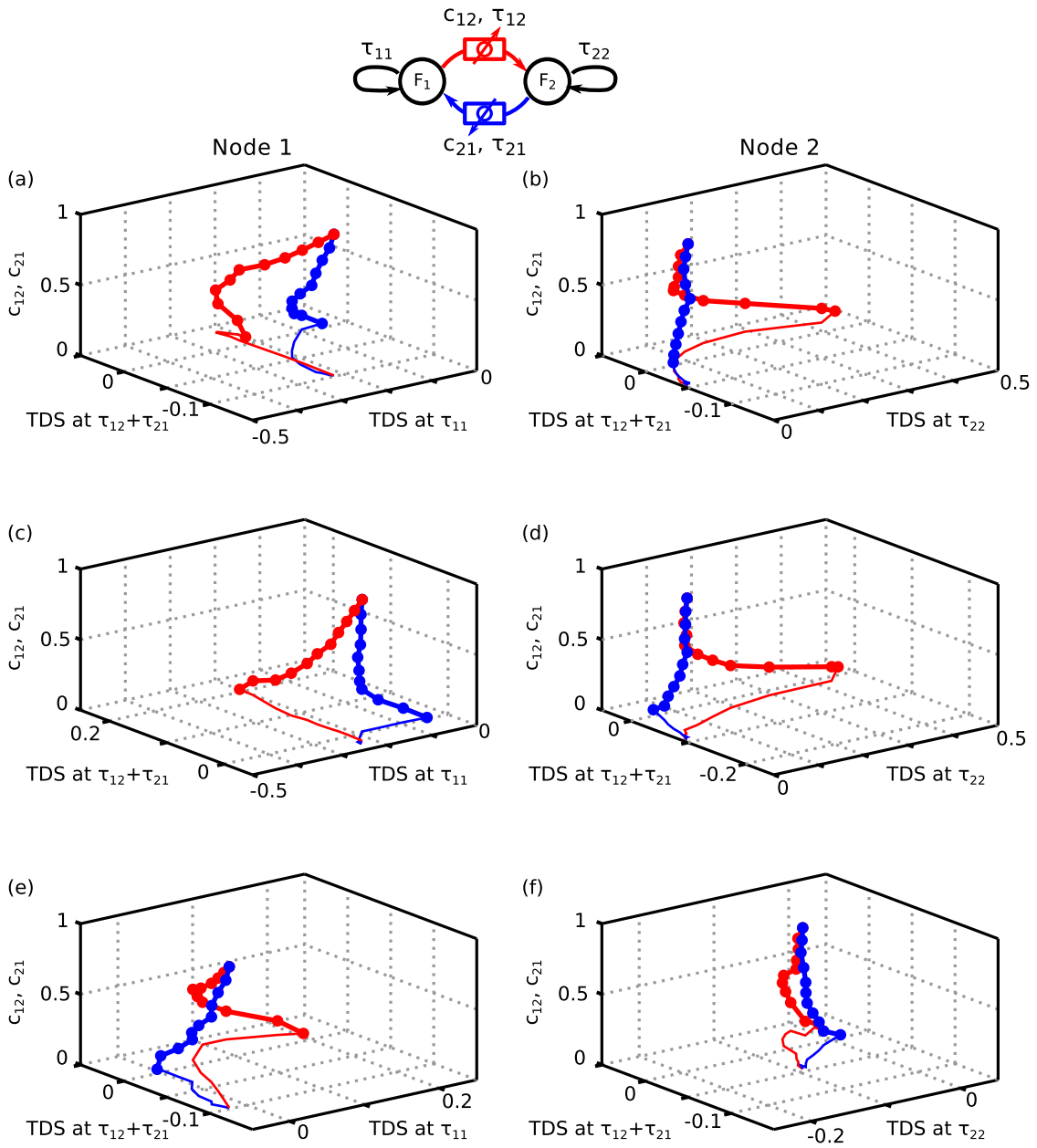


**Figure 5.5: Simulation: Strands in TDS-coupling strength space.** The TDSs were taken from the simulation with  $(\Phi_1, \Phi_2) = (0.03\pi, 0)$  and  $c_{12}$  (red) and  $c_{21}$  (blue) varied from 0 to 1. The projections of the strands onto the TDS plane are also shown.

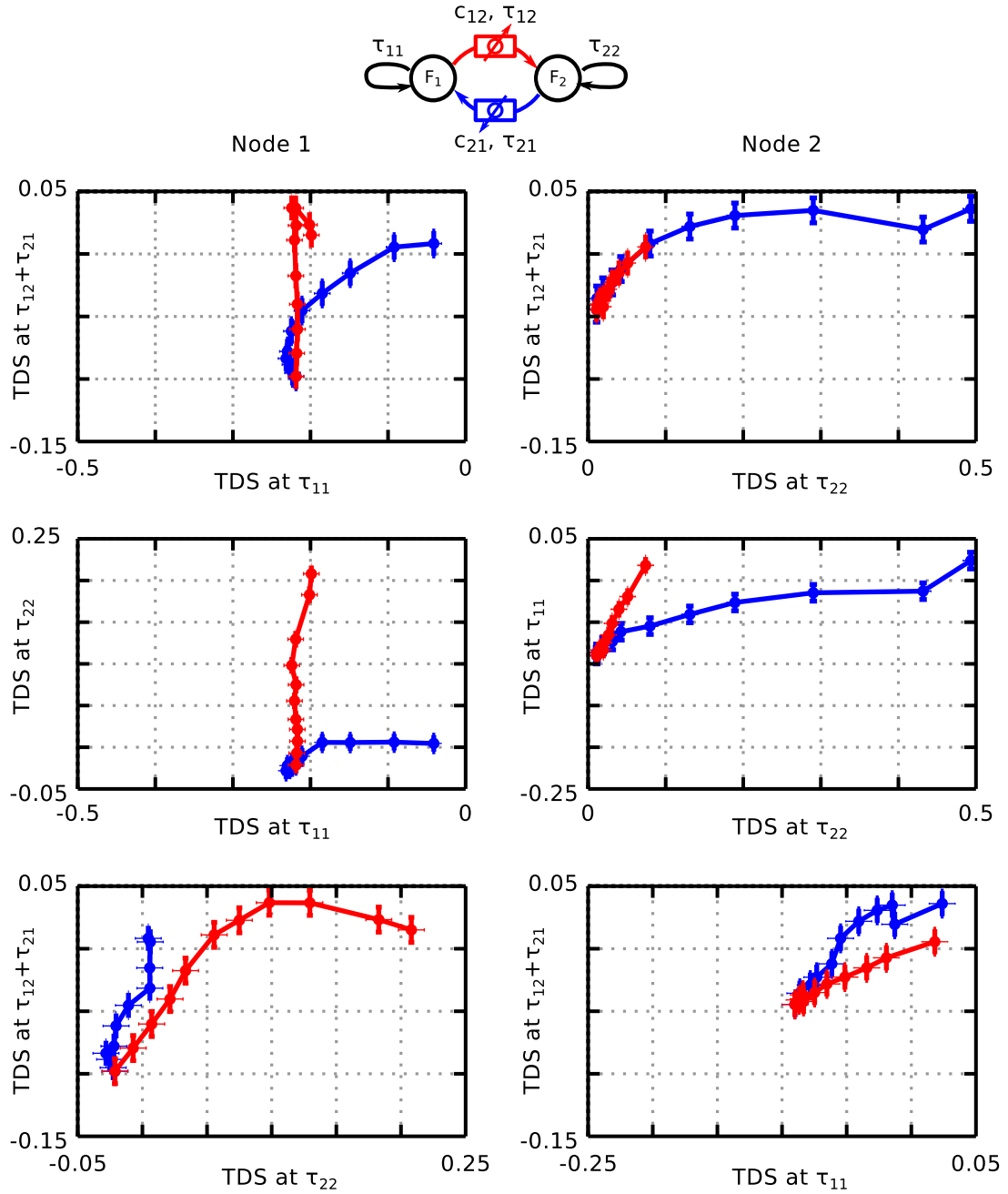


**Figure 5.6: Simulation: Projection of strands in  $TDS_1$ - $TDS_2$  plane.** The TDSs were taken from the simulation with  $(\Phi_1, \Phi_2) = (0.03\pi, 0)$  and  $c_{12}$  (red) and  $c_{21}$  (blue) varied from 0 to 1. The minimum attenuation necessary to distinguish the links (if it exists) is approximated by the first value of the coupling strength were the projections are distinct (taking into account the experimental uncertainty, shown with error bars).

the dynamics that I measure in the experiment with two coupled OEOs (denoted  $X_1(t)$  and  $X_2(t)$ ) are not  $V_1(t)$  and  $V_2(t)$ , but rather a bandpass filtered version of  $F_1 [V_1(t)]$  and  $F_2 [V_2(t)]$ . However, I find that taking this into account suppresses many of the TDSs and actually makes the agreement between experiment and simulation worse.

The differences between experimental and numerical results for the coupled OEOs could be due to several reasons, some of which are: the model greatly simplifies behavior of each component (see Appendix A); the model does not include any effects of noise; and there is a greater chance of multistability when the number of time delays is increased, which may impact the experimental and numerical systems differently.

### 5.3 Other types of observables

In Ch. 4, I state that TDSs are not the only choice of observables. In principle, any number that can be calculated from a single time series and that changes with the properties of the network can be used. The simplest quantities to track are the global maximum and minimum signal amplitudes. One would expect that, if the signal input to a node in a network is being attenuated, then the amplitude of the measured signal would also change. How it changes, however, depends on where the signal is being measured. While the experimentally accessible values  $X_{\max}$  and  $X_{\min}$  (at the output of the nonlinearity) do not change enough to be useful for sensing, I find numerically that  $V_{\max}$  and  $V_{\min}$  (at the output of the bandpass filter) experience relatively large changes, as shown in Fig. 5.7. For the case shown, the one dimensional sensing method using  $V_{\max}$  as an observable can distinguish between links for attenuations as low as 10%.

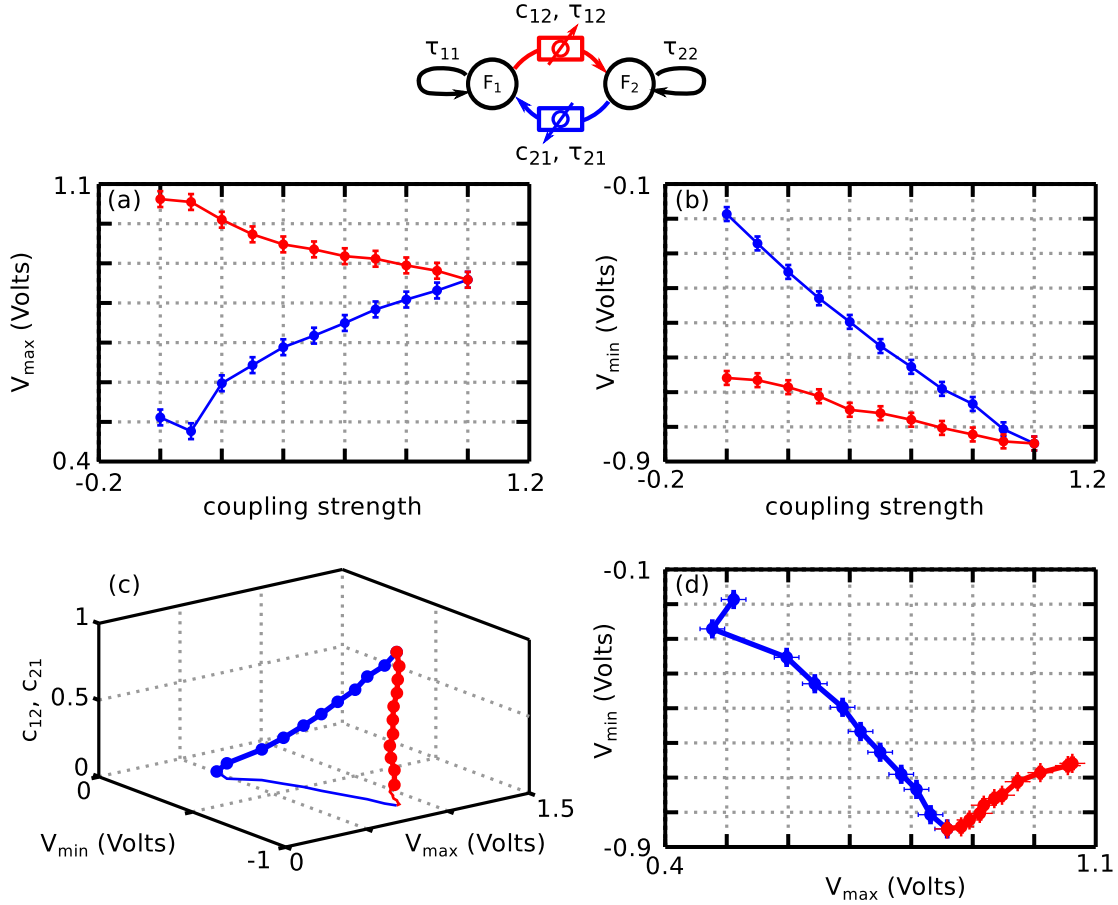


**Figure 5.7: Simulation: Maximum and minimum signal amplitudes.** The (a) maximum and (b) minimum signal amplitudes are taken from the dynamics of node 1 in the simulation with  $(\Phi_1, \Phi_2) = (0.03\pi, 0)$  and  $c_{12}$  (red) and  $c_{21}$  (blue) varied from 0 to 1. The (c) strands in observable-coupling strength space and (d) projections onto the observables plane are also shown.

## 5.4 Impact of the relative values of the time delays

In Ch. 4, I hypothesize that keeping the time delay of each link different improves the network's ability to sense changes with my method using TDSs as observables. This hypothesis is based on the ideas that (1) there are more distinct TDSs to observe allowing for higher-dimensional sensing methods and (2) the changes in different TDSs are more likely to be independent from one another if the corresponding time delays

**Table 5.1:** Values of the time delays in each of the four scenarios

Scenario	$\tau_{11}$ (ns)	$\tau_{22}$ (ns)	$(\tau_{12} + \tau_{21})/2$ (ns)
1	44.7	56.4	58.3
2	44.7	58.3	58.3
3	44.7	44.7	58.3
4	44.7	44.7	44.7

are incommensurate, allowing for improved distinguishability. To investigate the impact that the heterogeneities in the propagation delays have on the network's ability to sense changes, I numerically integrate Eqs. 5.4–5.7 and perform a two-dimensional calibration for four different scenarios:

1.  $\tau_{11} \neq \tau_{22} \neq (\tau_{12} + \tau_{21})/2$ ,
2.  $\tau_{11} \neq \tau_{22} = (\tau_{12} + \tau_{21})/2$ ,
3.  $\tau_{11} = \tau_{22} \neq (\tau_{12} + \tau_{21})/2$ ,
4.  $\tau_{11} = \tau_{22} = (\tau_{12} + \tau_{21})/2$ .

Note that in the homogeneous case, where all of the links have identical propagation delays, the round-trip coupling time delay is still different from the self-feedback time delays. The values of the time delays I use are shown in Table 5.1. I again use two metrics to quantify the quality of sensing: the average change in observables when each link is blocked, given by Eqs. 4.1 and 4.2; and the coupling strength at which the affected link is first distinguishable. I calculate both quantities for each pair of observables and each node for all four scenarios. The results are shown in Figs. 5.8 and 5.9.

A few conclusions can be drawn from this analysis. First, as the delay times are made successively identical for both nodes, the average change in the TDSs at  $\tau_{\text{self}}$ ,

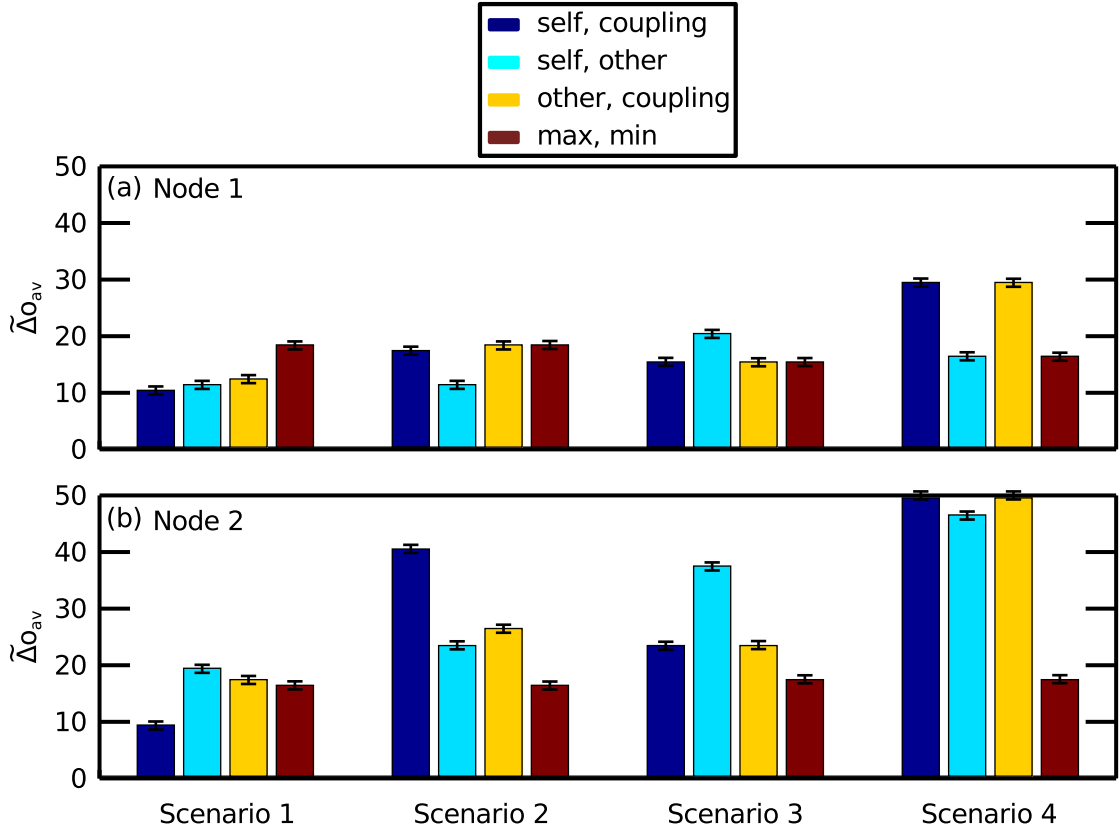


**Figure 5.8: Simulation: Average change in observables.** The change in each observable (TDSs at  $\tau_{\text{self}}$ ,  $\tau_{\text{other}}$ , and  $\tau_{\text{coupling}}$ ; maximum and minimum amplitude) are calculated for when each link is blocked using Eqs. 4.1 and 4.2 and then averaged. These quantities are then taken in pairs and averaged again to give a sense of how well each combination of observables performs. Due to the different values of  $\Phi_1$  and  $\Phi_2$ , the average change in observables are different for (a) node 1 and (b) node 2.

$\tau_{\text{other}}$ , and  $\tau_{\text{coupling}}$  undergo statistically significant increases from the completely heterogeneous case. This contradicts my original hypothesis that sensing is optimized when the time delays are distinct, in the sense that a larger change in observables allows for better resolution of the coupling strength. This is likely because making the time delays commensurate with one another increases the correlation at one particular time lag, which makes it more sensitive to changes. However, for the completely identical case, the ability to use TDSs to distinguish which link is attenuated vanishes, as

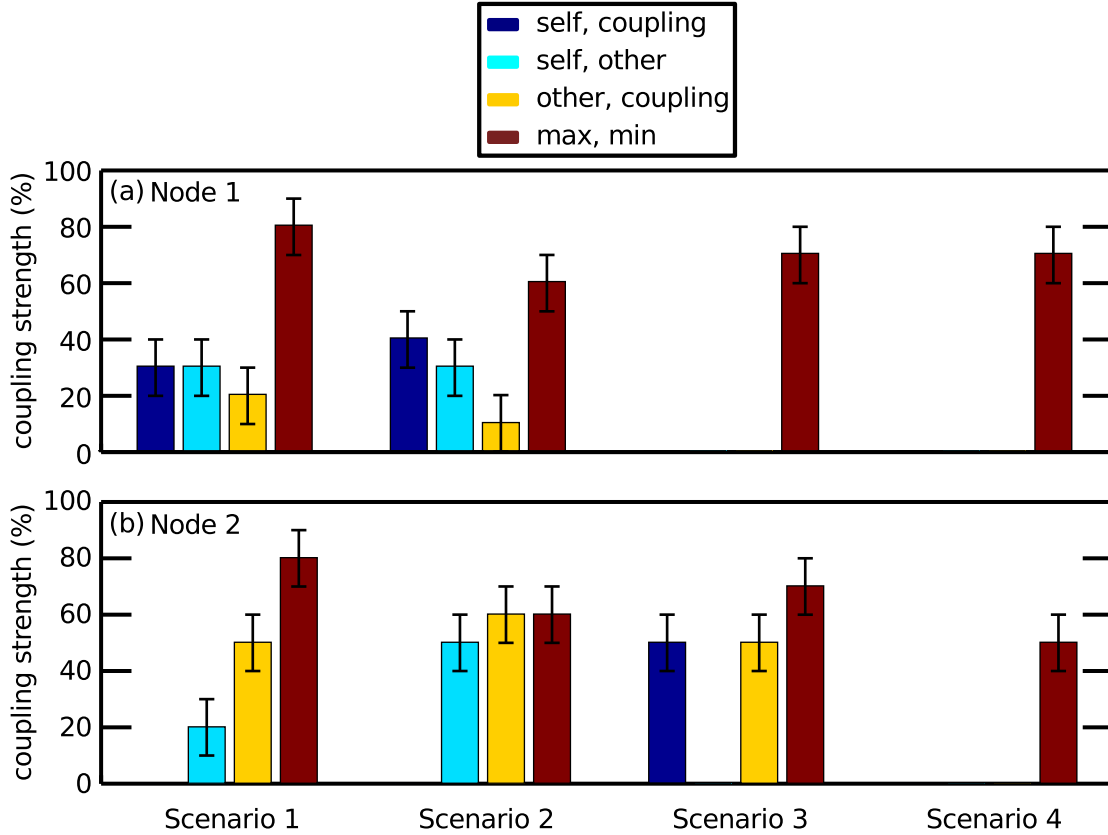


**Figure 5.9: Simulation: Coupling strength necessary to distinguish link.** This is approximated ( $\pm 10\%$ ) with the criterion that the projection of the observables for each strand have to separate by an amount greater than their experimental uncertainty to be considered distinct. Due to the different values of  $\Phi_1$  and  $\Phi_2$ , these values are different for (a) node 1 and (b) node 2.

can be seen in Fig. 5.9. This supports my hypothesis, in the sense that distinguishability is decreased for identical time delays. In fact, even though the TDSs in Scenario 4 undergo the greatest changes, sensing via my method fails because the projections of the strands never separate. Therefore, it seems that, when using TDSs as observables in this type of network, a balance must be struck between optimizing the resolution of the coupling strength and the distinguishability of the links. Based on this analysis, the best way to implement my sensing method with two numerical OEOs is to use Scenario 2 (where  $\tau_{11} \neq \tau_{22} = (\tau_{12} + \tau_{21})/2$ ) and monitor the TDSs of node 2. This results in a

relatively high measure of distinguishability ( $c = 60\%$ ) between the TDSs at  $\tau_{\text{other}}$  and  $\tau_{\text{coupling}}$ , and a high average change in observables for  $\tau_{\text{self}}$  and  $\tau_{\text{coupling}}$ .

The performance of the method using  $V_{\text{max}}$  and  $V_{\text{min}}$  as observables with regard to either metric is not affected by changes to the time delays in a statistically significant way. An advantage of using these as observables instead of TDSs is that the links remain distinguishable in all four scenarios. However, in my experiment, I do not have access to  $V$  due to the nonlinearity and filtering effects, which may very well be the case in many experimental realizations, making TDSs a more attractive observable due to their apparent sensitivity to changes in network parameters despite experimental measurement effects.

## 5.5 Replacing deterministic chaos with stochasticity

While I show that my method is able to determine changes in the network properties of delay-coupled nonlinear dynamical nodes, it remains unclear whether these sensing capabilities are due to the nonlinear dynamics, the particular network topology, or both. In Ref. [55], the authors show that delay-coupled unidirectional rings with chaotic nodes have correlation properties that obey the same scaling laws as those composed of linear stochastic nodes. In particular, they demonstrate that one can construct the correlation properties of a node in the network from the correlation properties of a collection of single nodes with time-delayed self-feedback. This works in both the deterministic and stochastic cases. One conclusion they draw from this is that emergent properties of the nodal dynamics can result solely from the network topology. Motivated by this work, I investigate to what extent the nonlinearity provides the sensitivity in my sensing scheme by implementing my method using a network with same coupling topology as in my experiment and previous numerical simulations, but

where the dynamics of the nodes are based on a linear stochastic process.

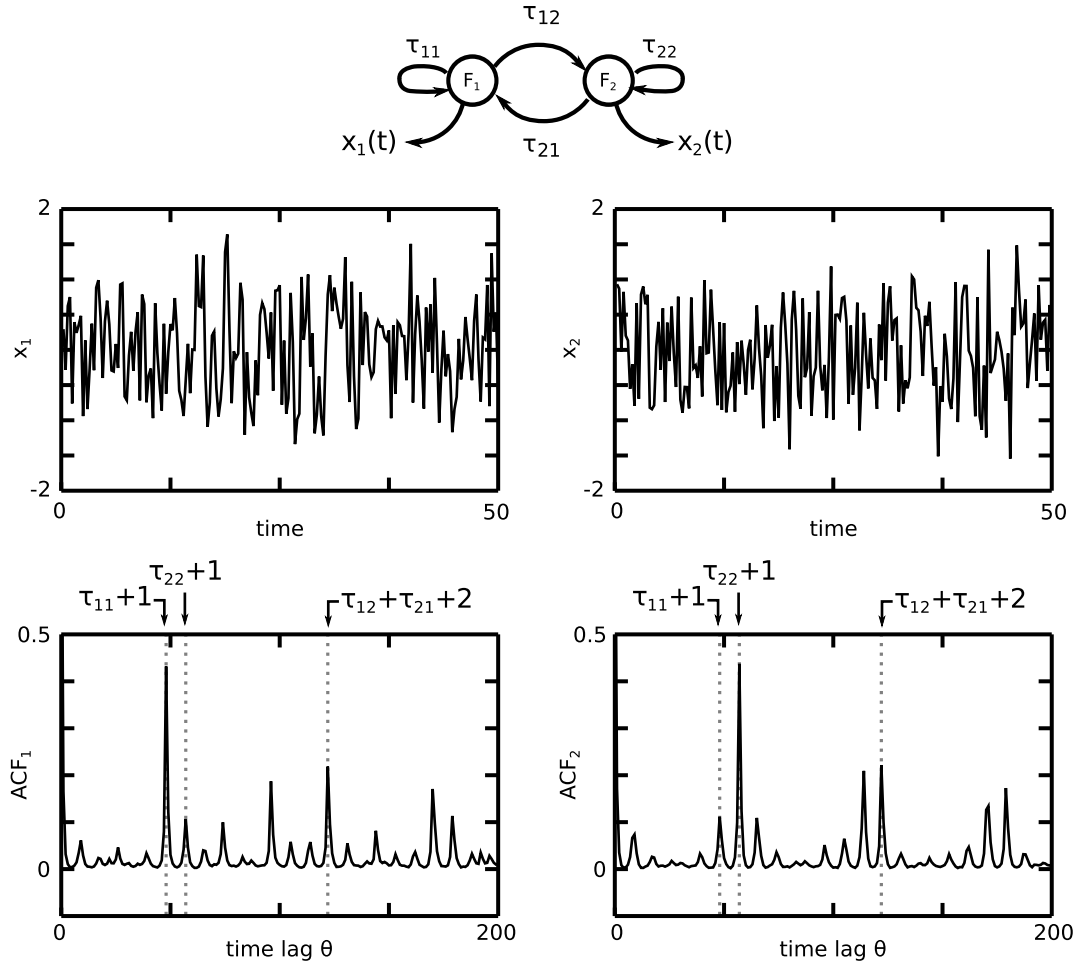
The two dynamical systems compared in Ref. [55] are a discrete-time linear stochastic map and a continuous-time chaotic Stuart-Landau oscillator. Again, since they found that the correlation properties of each type of system obeyed the exact same scaling laws, it seems reasonable to use the same linear stochastic map for my purposes. I modify the topology to include not only delay-coupling, but also time-delayed self-feedback. In particular, I investigate a two-node network with linear stochastic dynamics given by

$$x_1(t+1) = \alpha_1 x_1(t) + \xi_1(t) + \beta_1 x_1(t - \tau_{11}) + c_{21} \beta_2 x_2(t - \tau_{21}), \quad (5.8)$$

$$x_2(t+1) = \alpha_2 x_2(t) + \xi_2(t) + \beta_2 x_2(t - \tau_{22}) + c_{12} \beta_1 x_1(t - \tau_{12}). \quad (5.9)$$

Here,  $x_i(t)$  is the dynamic variable of node  $i$  at the discrete time step  $t$ ;  $\alpha_i$  is a parameter that accounts for node  $i$ 's dynamics;  $\xi_i$  is an independent white noise term; and  $\beta_i$  is a parameter characterizing the self-feedback gain of node  $i$ . As with the coupled OEOs,  $\tau_{ii}$  is the self-feedback time delay,  $\tau_{ij}$  is the coupling time delay between node  $i$  and node  $j$ , and  $c_{ij}$  is the normalized coupling strength between node  $i$  and  $j$ .

An example of the dynamics produced for  $\alpha_1 = \alpha_2 = 0.1$ ,  $\beta_1 = \beta_2 = 0.4$ ,  $\tau_{11} = 47$ ,  $\tau_{22} = 56$ , and  $\tau_{12} + \tau_{21} = 120$  is shown in Fig. 5.10. The correlation properties are qualitatively similar to those of two coupled (nonlinear) OEOs, where sharp peaks are superimposed on a delta function-like background. The peaks are located near multiples of:  $\tau_{11} + 1$ ,  $\tau_{22} + 1$ ,  $\tau_{12} + \tau_{21} + 2$ , and sums and differences of these three timescales. Note that the peaks are shifted by one time step from the self-feedback time delays (two time steps from the round-trip coupling time delay) due to the fact that correlations arise between  $x_i(t+1)$  and  $x_i(t - \tau_{ii})$  ( $x_j(t - \tau_{ij})$ ) in this discrete time system. I still refer to these peaks, however, as the TDS at  $\tau_{ij}$ .



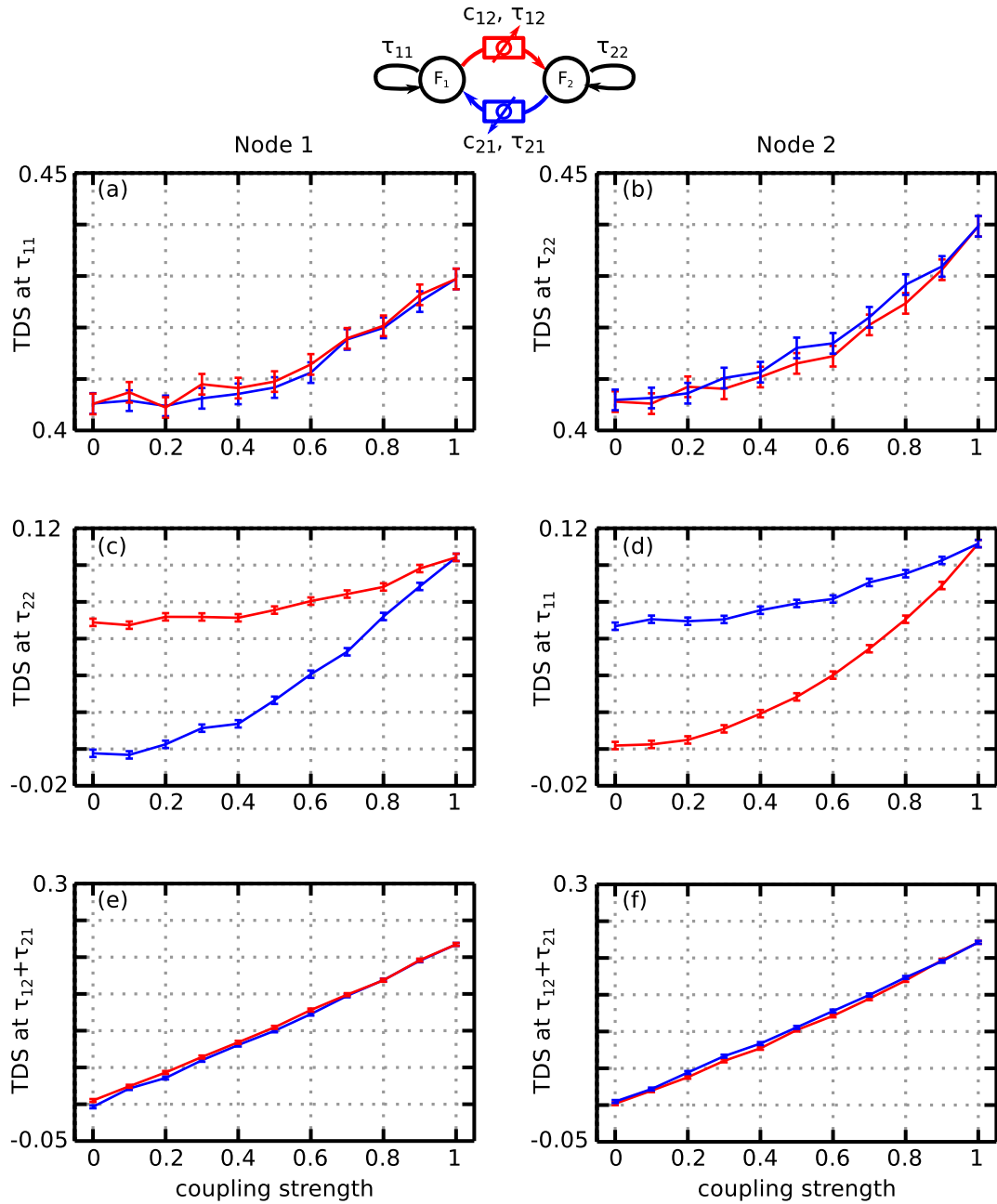
**Figure 5.10: Two coupled linear stochastic maps.** The time series (a,c) and ACF (b,d) of two coupled linear stochastic maps with  $\alpha_1 = \alpha_2 = 0.1$ ,  $\beta_1 = \beta_2 = 0.4$ ,  $c_{12} = c_{21} = 1.00$ ,  $\tau_{11} = 47$ ,  $\tau_{22} = 56$ , and  $\tau_{12} + \tau_{21} = 120$ . The coupled maps are initialized with a random IHF and then iterated for  $10^6$  time steps.

Figure 5.11 shows the TDSs as the coupling strength along each link is varied, and Figs. 5.12 and 5.13 show the strands and projections that the TDSs make in the  $TDS_1$ - $TDS_2$  plane. One-dimensional sensing is impossible with these observables, due to the fact that the ranges overlap in all six cases shown in Fig. 5.11. Two-dimensional sensing, however, is possible in four of the six cases shown in Figs. 5.12 and 5.13. This demonstrates that sensing can be achieved in a two-node network with stochas-

tic dynamics that do not involve any nonlinear effects, due to the fact that changes in the network properties result in statistically significant changes in the correlation properties.

Interestingly, the four cases where two-dimensional sensing is successful all involve using the TDS at  $\tau_{\text{other}}$ , as this is the only TDS that responds differently depending on which link is attenuated. In the cases with the experimental and numerical nonlinear nodes, however, the TDSs at both  $\tau_{\text{self}}$  and  $\tau_{\text{other}}$  often have different behavior depending on which link is attenuated. This could be due to the fact that, in the nonlinear cases, some of the nodal parameters were different, whereas in the linear case they are all identical, with the exception of the self-feedback time delays.

As with the numerical simulation of the OEOs, I investigate the impact that the relative values of the time delays in the network have on my sensing method. I use the same four scenarios described in the previous section, and the results are shown in Figs. 5.14 and 5.15. Comparing this analysis to that of the numerical simulation of nonlinear nodes, there are some similarities. First, the average change in the TDSs at  $\tau_{\text{self}}$ ,  $\tau_{\text{other}}$ , and  $\tau_{\text{coupling}}$  increase from the completely heterogeneous case as the time delays are made successively identical, indicating that this is a generic trend of networks with this topology. Second, the distinguishability vanishes for Scenarios 3 and 4 when the TDSs at  $\tau_{\text{self}}$  and  $\tau_{\text{other}}$  are used as observables, which it has to since  $\tau_{\text{self}} = \tau_{\text{other}}$  in these cases. However, unlike the nonlinear case, the distinguishability does not vanish for these two scenarios when the TDSs at  $\tau_{\text{self}}$  and  $\tau_{\text{coupling}}$  are used. This is particularly surprising because, in the heterogeneous case (Scenario 1), I see that only the TDS at  $\tau_{\text{other}}$  has different behavior for different links. One might think that setting  $\tau_{\text{other}} = \tau_{\text{self}} = \tau_{\text{coupling}}$  would eliminate its distinguishability, but this is not the case, as shown in Fig. 5.16.



**Figure 5.11: Stochastic map: TDSs as coupling strength varies.** Data for both nodes is shown. The red data points correspond to  $c_{12}$  varying (with  $c_{21} = 1$ ) and the blue data points to  $c_{21}$  varying (with  $c_{12} = 1$ ). TDSs at (a,b)  $\tau_{\text{self}}$ , (c,d)  $\tau_{\text{other}}$ , and (e,f)  $\tau_{\text{coupling}}$  are shown. The errors bars of 0.002 represent the standard deviation of the TDSs obtained from iterating the coupled maps for  $10^6$  time steps starting with random IHFs several times.

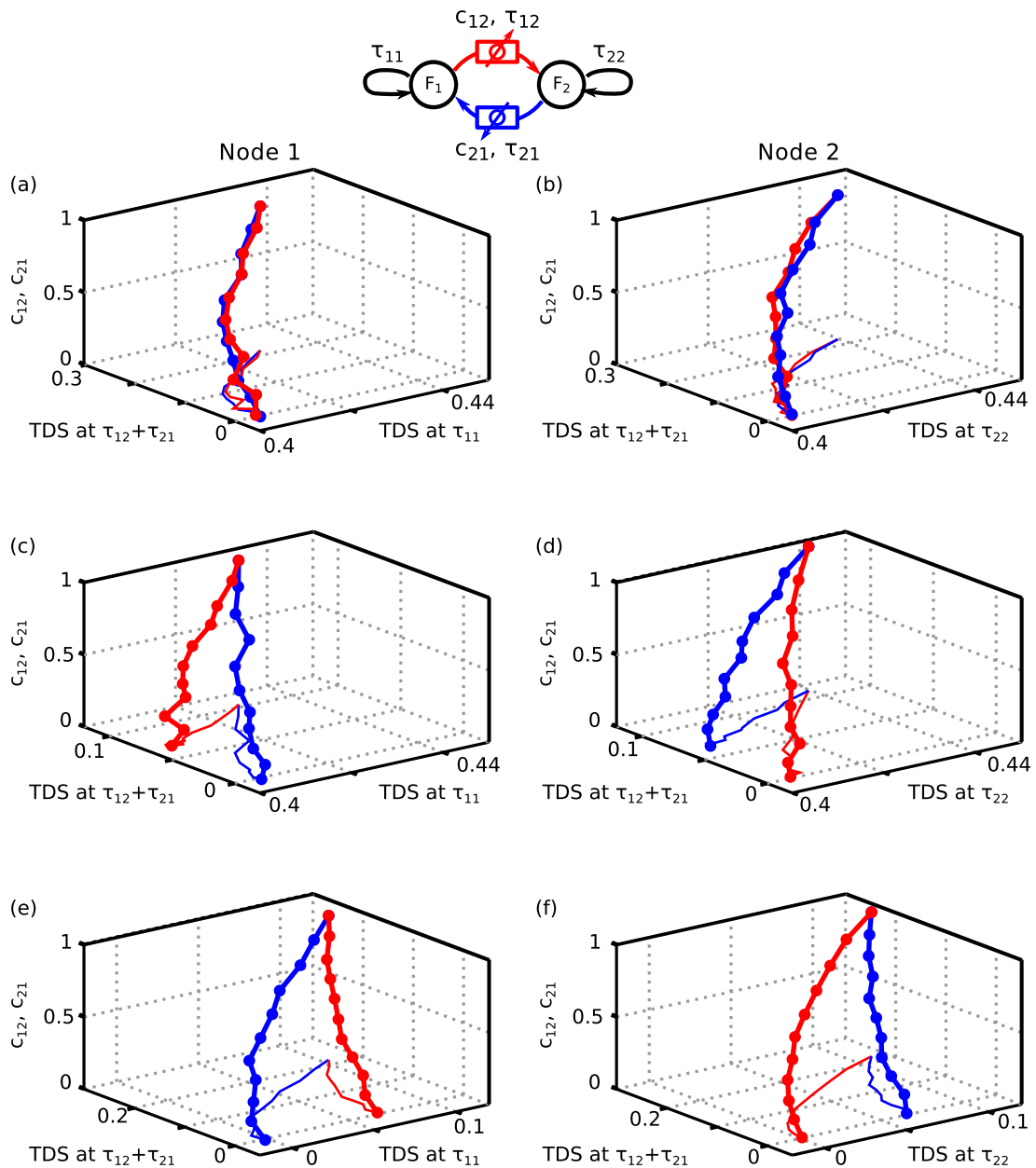


**Figure 5.12: Stochastic map: Strands in TDS-coupling strength space.** The TDSs were taken from the stochastic map with  $c_{12}$  (red) and  $c_{21}$  (blue) varied from 0 to 1. The projections of the strands onto the TDS plane are also shown.

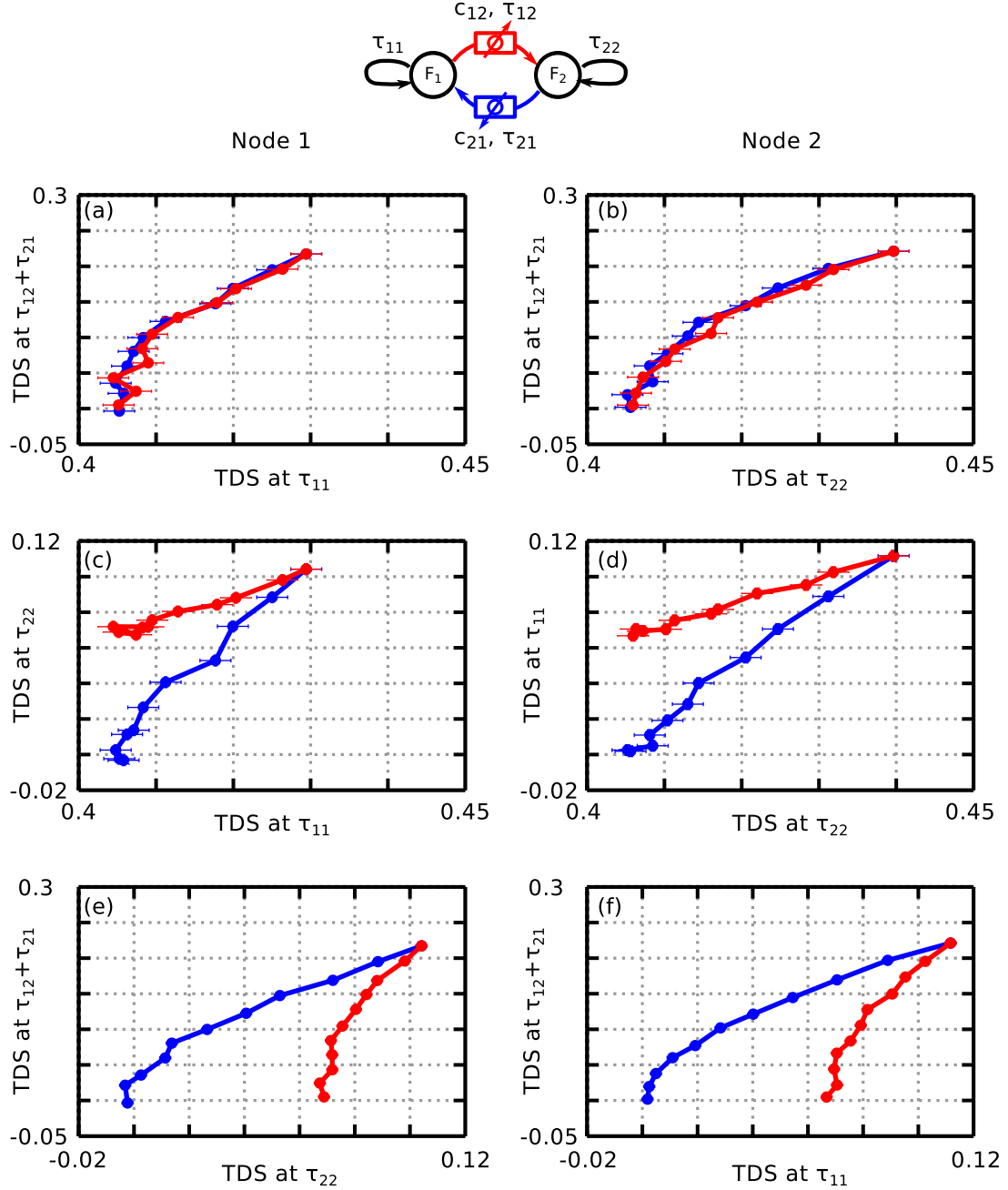


**Figure 5.13: Stochastic map: Projection of strands in  $TDS_1$ - $TDS_2$  plane.** The minimum attenuation necessary to distinguish the links (if it exists) is approximated by the first value of the coupling strength were the projections are distinct (taking into account statistical uncertainty, shown with error bars).

$V_{\max}$  and  $V_{\min}$  cannot be used as observables in the stochastic case, however, because distinguishability fails in all four scenarios. In the nonlinear case, the maximum and minimum signal amplitudes are mostly determined by the saturations of the nonlinearity and the auxiliary variable  $U$ . There is no saturation in the stochastic case, however, making the maximum and minimum signal amplitudes behave more erratically.

Thus, this analysis shows that sensing can be achieved without any nonlinear effects, as long as the topology includes time-delayed coupling and feedback. However, the observables and relative values of the time delays must be chosen differently depending on the type of dynamics (nonlinear or linear) on the nodes in the network.

## 5.6 Summary

In this chapter, I demonstrate two proof of principle simulations of my sensing method: one with a deterministic DDE model describing the nonlinear dynamics of two coupled OEOs, and one with a linear stochastic map. I use these models to investigate the roles that heterogeneities in the time delays and different types of nodal dynamics play in my sensing scheme. In doing so, I find that equating the different time delays increases the average change in the TDSs, which in turn increases the precision with which the coupling strength can be determined, but only if the links are distinguishable. In the case with nonlinear dynamics, making the time delays identical erases distinguishability, but this does not happen in the case with linear stochastic dynamics. Therefore, my method can be applicable to networks with heterogeneous or homogeneous time delays and linear or nonlinear nodes, but the performance must be optimized differently for each type of network.

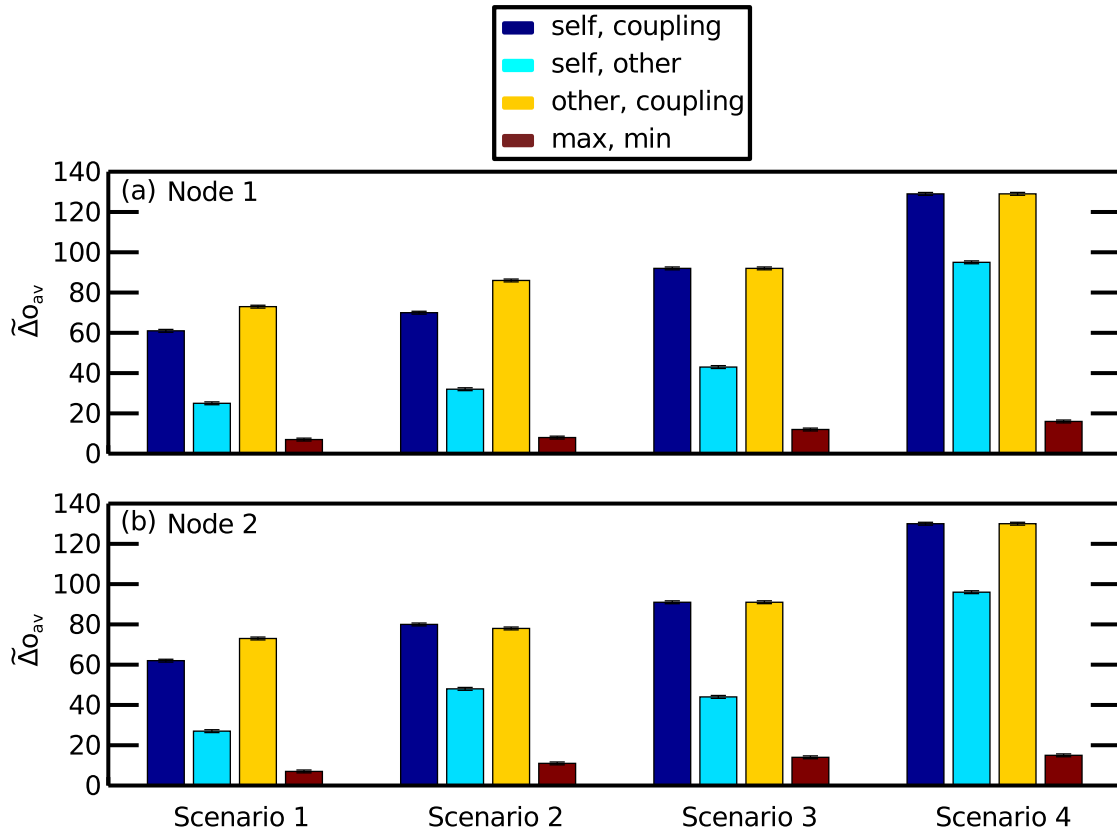


**Figure 5.14: Stochastic map: Average change in observables.** The change in each observable (TDSs at the measured node’s self-feedback delay time, the other node’s self-feedback delay time, and round-trip coupling delay time; maximum and minimum amplitude) are calculated for each link using Eqs. 4.1 and 4.2 and then averaged. These quantities are then taken in pairs and averaged again to give a sense of how well each combination of observables performs. Due to the different values of the time delays, the average change in observables can be different for (a) node 1 and (b) node 2.

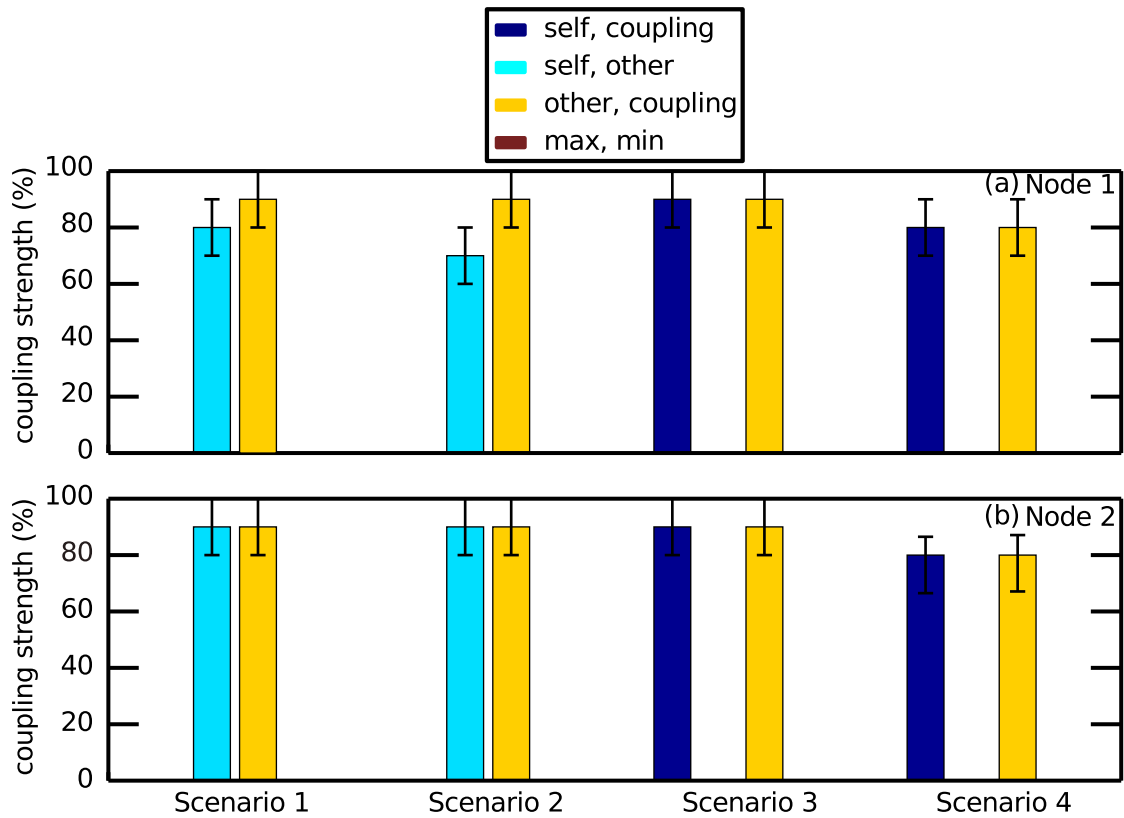


**Figure 5.15: Stochastic map: Coupling strength necessary to distinguish link.** This is approximated ( $\pm 10\%$ ) with the criterion that the projection of the observables for each strand have to separate by an amount greater than their experimental uncertainty to be considered distinct. Due to the different values of the time delays, these values can be different for (a) node 1 and (b) node 2.

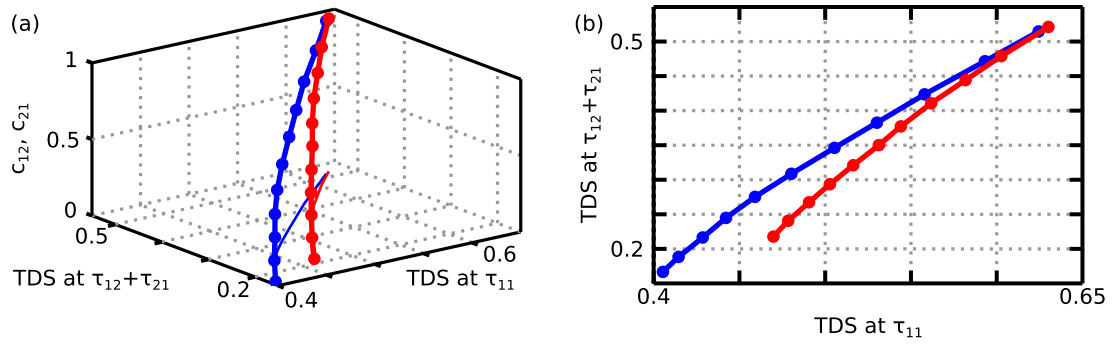


**Figure 5.16: Stochastic map: Identical delays.** (a) The strands in observable-coupling strength space and (b) projections of the strands onto the observables plane are shown for  $\tau_{11} = \tau_{22} = \tau_{12} = \tau_{21} = 47$ . The observables are the TDSs at  $\tau_{11}$  and  $\tau_{12} + \tau_{21}$ .

# Chapter 6

## Conclusions

In this dissertation, I develop and perform a proof of principle demonstration of a method to infer changes in the properties of a network by monitoring characteristics of the chaotic dynamics of one of its nodes. In this chapter, I summarize the main contributions from each chapter and provide an outlook for future research.

### 6.1 Summary of results

In the first chapter, I provide the necessary background information on chaotic dynamics and networks to motivate my research question. I then briefly introduce the well-studied experimental device, an OEO, which I make use of throughout the rest of the dissertation.

In Ch. 2, I give an overview of the characteristics of nonlinear, time-delayed dynamical systems. OEOs belong to this class of systems, and I provide highlights of recent research with OEOs, including my own published and unpublished work. My finding that, for a particular choice of parameters, an OEO generates nearly featureless, broadband chaos appears in Refs. [8–10]. My subsequent discovery, however, that this chaos contains TDSs with values that depend sensitively on a particular parameter of the OEO has yet to be reported in the literature. The behavior of these TDSs are important for my proposed sensing method.

Other researchers have proposed potential solutions to the research question I am interested in, and I present one particular approach in Ch. 3. This approach is also

implemented with a small network of OEOs, but is done using dynamics with speeds that are six orders of magnitude slower than the dynamics used in my work. Furthermore, this approach relies on chaos synchronization, which often requires that the nodal parameters be nearly identical. This motivates my search for a method that can be implemented with high-speed and heterogeneous dynamical nodes.

In Ch. 4, I return to studying the behavior of TDSs, only now in an experimental network of two coupled OEOs as the coupling strengths along each of the links are varied. I find that TDSs at the self-feedback time delay of each node, denoted  $\tau_{11}$  and  $\tau_{22}$ , are sensitive to which of the two links is attenuated. While the TDS at the round-trip coupling time,  $\tau_{12} + \tau_{21}$ , also changes with coupling strength, it is not necessarily sensitive to which link is attenuated. In general, I find that the behavior of the TDSs depend not only on the network parameters, but also on the parameters of each node.

I then propose and demonstrate a method to use one or two TDSs to track potential changes in coupling strength along either of the links. I generalize this method to use  $D$  observables, which can be TDSs or other quantities computed from the time series of one of the nodes, and find that the sensing capabilities can be improved by increasing  $D$ , but at the expense of additional computations and decreased ease of visualization. I quantify the performance of my sensing network with two metrics: (1) the average change in observables, which relates to the precision with which the coupling strength can be determined; and (2) the minimum attenuation necessary to distinguish which link is affected. I find that the first metric is optimized when a particular parameter of the nodes is made to be heterogeneous. For this choice of parameters, I find that the affected link can be determined for changes in coupling strength greater than  $20\% \pm 10\%$ . Also, if the coupling strength along either link is changed from fully coupled to fully attenuated, then, on average, the TDSs change by approximately 40 times their experimental uncertainty, making it feasible to approximate the new coupling strength

for large enough perturbations. It is important to note that these measurements are based solely on  $\sim 10 \mu s$  worth of data collected from a single node generating chaos with a bandwidth of  $\sim 10$  GHz.

To verify that the behavior of the TDSs are captured by simple models describing an isolated OEO and two coupled OEOs, I perform numerical integrations of both models in Ch. 5. I then use the model for two coupled OEOs to demonstrate a proof of principle of my sensing method numerically and to explore its performance as the time delays are successively made identical. In contrast to my original hypothesis, the average change in TDSs is greatest for the completely identical time delay scenario, which corresponds to improved precision in determining the coupling strength. In this scenario, however, it is impossible to determine which link was attenuated, indicating that a balance must be struck between the network's ability to discern the new coupling strength and the affected link.

I also test my method numerically with a network of linear stochastic maps. I find that, as long as the topology includes time-delayed coupling and feedback, sensing can be achieved without nonlinear effects. The performance, however, is optimized differently than in the nonlinear, deterministic case. For example, unlike the numerical OEO case, in the scenario where all of the time delays are identical it is possible to determine both the coupling strength and the attenuated link.

Finally, I conclude here with a graphical comparison of the performance of all three implementations of my method (experimental OEOs, numerical OEOs, and numerical stochastic maps) in Figs. 6.1 and 6.2. By these metrics, when the TDSs at  $\tau_{\text{other}}$  and  $\tau_{\text{coupling}}$  are used as observables, the numerical simulations of the stochastic map outperform both implementations with the OEO in terms of ability to precisely determine the coupling strength. This is likely due to the small uncertainty in the TDSs that can be achieved numerically, and it remains unclear what the uncertainty and performance

would be in an experimental realization with stochastic nodes. It is also interesting to note that, when TDSs are used as observables, the OEO experimental implementation outperforms that of the OEO numerical implementation in terms of distinguishability.

In the experimental implementation with deterministic chaos, all three combinations of TDSs allow the observer to determine which link was attenuated, while only two of the three combinations are successful in the numerical stochastic case. This could be due to the effects of the nonlinearity or of the different nodal parameters. Distinguishability is also achieved in the numerical OEO implementation, but for lower values of coupling strength (higher attenuation). In the experimental and stochastic implementations, the maximum and minimum signal amplitudes fail to determine which link is affected, indicating that this is a poor choice for observables in certain settings. All of these observations show that TDSs, which are relatively simple to compute, can be used to infer changes to the properties (coupling strengths along the links) of a two-node network. In addition, the success and similarities of my sensing method in all the three different implementations indicate that the dynamical properties of a network of high-dimensional chaotic systems are not all that different than those of a network composed of stochastic nodes.

## 6.2 Future directions

While I successfully demonstrate a method to detect sufficiently large changes in the coupling strength along one of the links in a two-node network, this is only a modest step toward the potential realization of a high-speed sensing network and answers to the broader questions I present at the beginning of this dissertation (e.g. the network inverse problem and information flow in networks).

To continue to push forward, understanding how my method scales with the size of

the network is the next important step. I know that each additional link corresponds to an additional strand in observable-coupling strength space. In theory, these  $L$  strands should be distinct. Experimentally, however, it is unclear whether additional strands will be distinct when taking into account experimental uncertainty and if the observables corresponding to “distant” links will change enough for the coupling strength to be determined. Initial investigations into three-node networks of numerical OEOs and stochastic maps show that the third strand can be made distinct, but that the changes in observables decrease relative to those of the corresponding two-node networks.

Additionally, this method needs to be modified to detect multiple intruders (or changes in coupling strength along multiple links). One possibility is that, instead of using calibration strands for changes in the properties of one link, surfaces will be formed when calibrating the network for simultaneous changes along two links. This analysis will be aided with the use of a “statisticians” model, where the value of each observable has both an average value and a probability spread for each choice of the network’s parameters.

After these issues have been addressed, a wireless rf prototype that responds to attenuations due to water-based intruders should be built and analyzed. This will allow for the investigation of how additional complications (such as changes in propagation delay between the nodes due to the presence of an intruder and reflections off of the environment) impact the network’s ability to sense intruders. It will also be interesting to build a stochastic prototype and test it against the deterministic one.

Beyond building a real sensor network, it remains to be seen if and how knowledge of the response of TDSs to changes in network properties corresponds to changes in information theoretical measures, such as transfer entropy [56]. If such a correspondence could be established, then measuring TDSs could prove to be a much simpler way to analyze information flow in networks with chaotic dynamics and time delays.

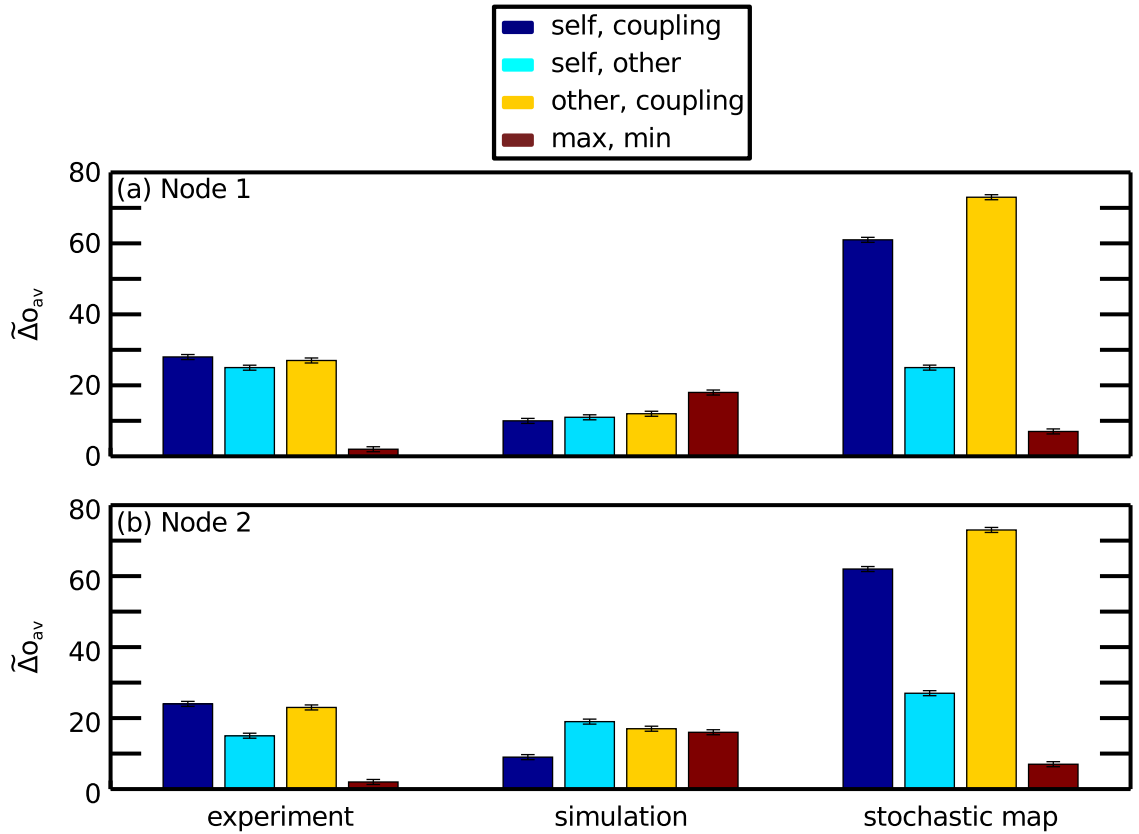


**Figure 6.1: Comparison: Average change in observables.** The results from the OEO experiment (with  $(\Phi_1, \Phi_2) = (0, -0.08\pi)$ ,  $\tau_{11} = 44.7$  ns,  $\tau_{22} = 56.4$  ns, and  $\tau_{12} + \tau_{21} = 116.6$  ns), OEO simulation (with  $(\Phi_1, \Phi_2) = (0.03\pi, 0)$ ,  $\tau_{11} = 44.7$  ns,  $\tau_{22} = 56.4$  ns, and  $\tau_{12} + \tau_{21} = 116.6$  ns), and stochastic map simulation (with  $\alpha_1 = \alpha_2 = 0.1$ ,  $\tau_{11} = 47$ ,  $\tau_{22} = 56$ , and  $\tau_{12} + \tau_{21} = 120$ ) are shown. Due to differences in the parameter values, the average change in observables are different for (a) node 1 and (b) node 2.

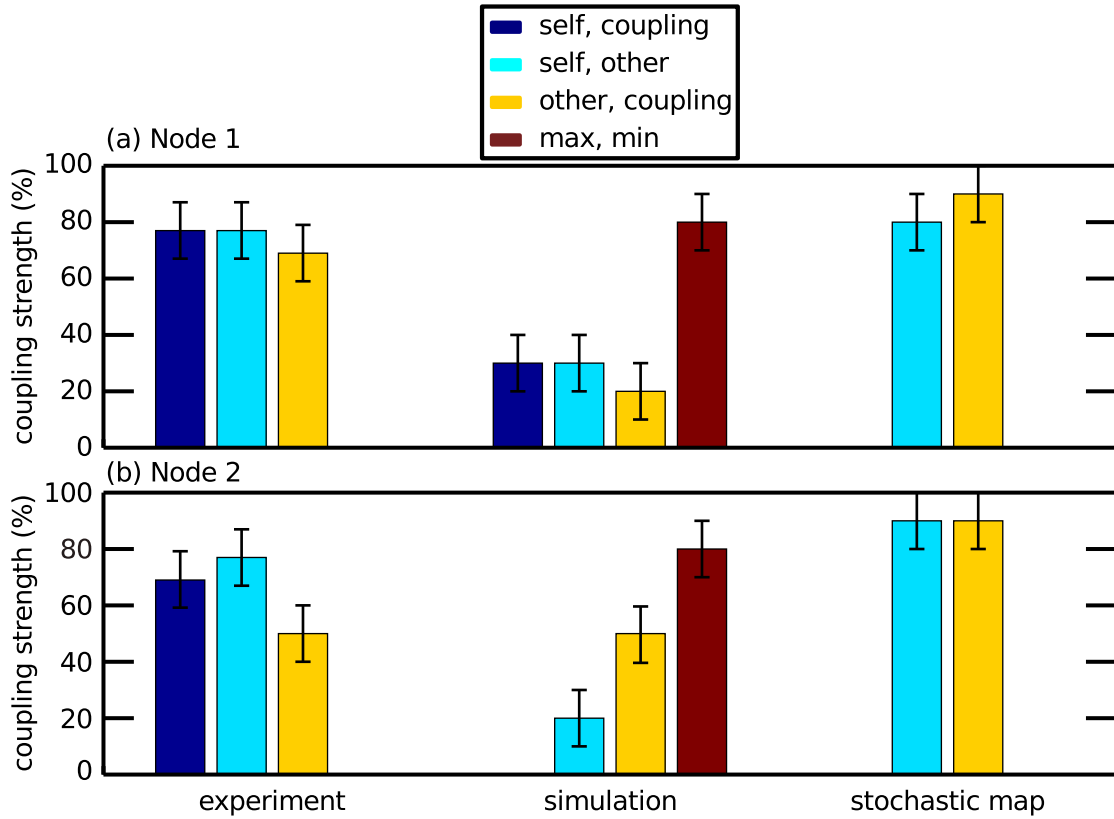


**Figure 6.2: Comparison: Coupling strength necessary to distinguish link.** The results from the OEO experiment (with  $(\Phi_1, \Phi_2) = (0, -0.08\pi)$ ,  $\tau_{11} = 44.7$  ns,  $\tau_{22} = 56.4$  ns, and  $\tau_{12} + \tau_{21} = 116.6$  ns), OEO simulation (with  $(\Phi_1, \Phi_2) = (0.03\pi, 0)$ ,  $\tau_{11} = 44.7$  ns,  $\tau_{22} = 56.4$  ns, and  $\tau_{12} + \tau_{21} = 116.6$  ns), and stochastic map simulation (with  $\alpha_1 = \alpha_2 = 0.1$ ,  $\tau_{11} = 47$ ,  $\tau_{22} = 56$ , and  $\tau_{12} + \tau_{21} = 120$ ) are shown. Due to differences in the parameter values, these values are different for (a) node 1 and (b) node 2.

# Appendix A

## Experimental apparatus

The experimental results presented in this dissertation are obtained with a network of two high-speed optoelectronic oscillators (OEOs) that I developed. In this chapter, I describe and characterize the components that comprise each of the OEOs.

*This chapter is based partly on Ref. [8].*

### A.1 OEO overview and components

The optoelectronic network under investigation is comprised of commercially available high-speed components which, due to the presence of a delayed-feedback, delayed-coupling and nonlinear elements, can display a variety of behaviors. As shown in Fig. A.1, the setup of each OEO is as follows: light with a wavelength of 1550 nm generated in a semiconductor laser propagates through a single mode optical fiber, a polarization controller, and a Mach-Zehnder modulator (MZM). The light exiting  $MZM_i$  is split by an optical coupler, and half of the power is split again and incident on two photodetectors: one to measure the dynamical variable  $X_i(t)$  and the other to determine relevant properties of  $MZM_i$  (to be described later). The other half of the signal is also split again, so that half can continue through the self-feedback loop of  $OEO_i$  and the other half can be sent to  $OEO_j$  via a variable optical attenuator. The signals from  $OEO_i$  and  $OEO_j$  are then combined by a fourth optical coupler, incident on a high-speed photodetector, and the resulting voltage is amplified by a modulator driver and fed back into  $MZM_i$  via a radio-frequency (rf) port. By adjusting the gain in each feedback loop, the operating point of the nonlinearity, the lengths of the four time delays, and the coupling strengths along the links from  $OEO_i$  to  $OEO_j$ , the dynamics

of the system can be tuned. The following subsections describe each of the system components in greater detail.

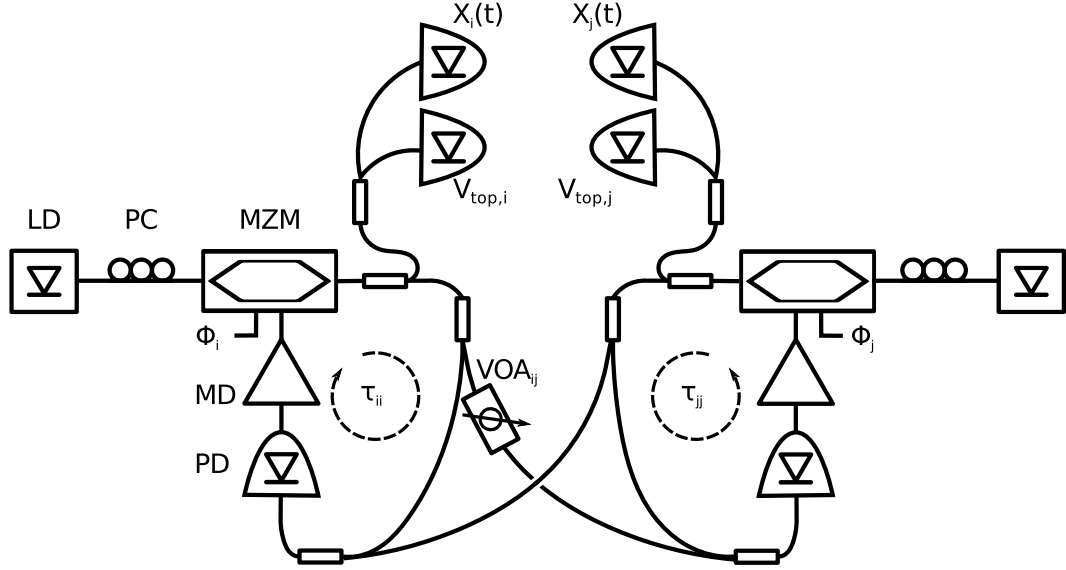


**Figure A.1: Detailed experimental setup.** Each OEO consists of a laser diode (LD), polarization controller (PC), Mach-Zehnder modulator (MZM), four 50/50 optical couplers, two high-speed photodiodes (PD), one slow-speed photodiode, and a modulator driver (MD). The signal exiting  $MZM_i$  is split such that a quarter is measured by a high-speed photodiode ( $X_i(t)$ ), a quarter is used to determine  $V_{top,i}$ , a quarter is sent to  $OEO_j$ , and a quarter is fed back to itself. A variable optical attenuator (VOA) can be placed between the couplers connecting  $OEO_1$  to  $OEO_2$  or  $OEO_2$  to  $OEO_1$ .

### A.1.1 The laser diodes

Laser diodes are an essential element of many optoelectronic systems [57, 58]. Lasers of this type can produce radiation with wavelengths anywhere from 0.3 to 100  $\mu\text{m}$ . Due to the low-loss transmission window in optical fibers at 1550 nm, many laser diodes are designed to emit infrared radiation at this wavelength. The Sumitomo InGaAsP/InP distributed-feedback multi-quantum-well laser diode used in my experimental setup (model SEI SLT5411) emits at this wavelength.

One can derive rate equations that govern the optical power emitted by a laser diode as a function of the injection current,  $I$  [57]. Linear stability analysis of these equations shows that, beyond a threshold  $I_{\text{th}}$ , the laser emits steady-state power that increases linearly with  $I$ . To verify this dependence, I measured the output power with a photoreceiver (Thorlabs DET01CFC) for several values of the current, as shown in Fig. A.2. I find that, above  $\sim 10$  mA, the measured steady-state power  $P_{\text{LD}}$  (in milliwatts) as a function of current  $I$  (in milliamperes) for one my lasers is approximately given by

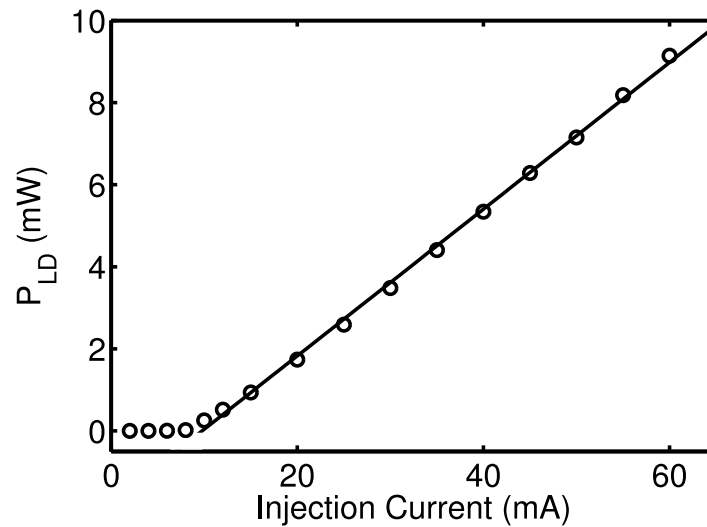


**Figure A.2: Characterizing laser diode.** A least-squares-fit of the linear regime is superimposed.

$$P_{\text{LD}} \approx 0.179 \text{ [mW/mA]}(I - I_{\text{th}}), \quad (\text{A.1})$$

with  $I_{\text{th}} = 9.77$  mA, based on a least-squares fit for the data points in the linear regime.

### A.1.2 The polarization controllers

The MZM (described in the next section) is a polarization sensitive device and only functions properly for light linearly polarized along a particular direction. The light exiting the laser diode is linearly polarized, but the polarization can change along the optical fiber due to birefringence. This can be understood by noting that the index of refraction of glass decreases when it is compressed and increases when it is expanded [59]. Bending the fiber compresses the glass one direction and expands it in another, which induces birefringence and leads to a change in the polarization state.

The polarization controller I use consists of a quarter-waveplate, half-waveplate, and another quarter-waveplate connected in series. The waveplates are constructed by simply looping fiber around a spool (with the half-waveplate having twice as many loops as the quarter-waveplates) to compress the glass in the direction parallel to the plane of the spool and expanding it in the plane perpendicular to the spool, thus inducing birefringence. The quarter-waveplates introduce a  $\pi/4$  phase shift between the two polarization axes and convert linearly polarized light into elliptically polarized light or vice versa. The half-waveplate introduces a  $\pi/2$  phase shift, which causes the direction of polarization to flip about the fast axis. By manually rotating the fast axis of each of the waveplates, I can adjust the polarization state of the light exiting the polarization controller and incident on the MZM.

### A.1.3 The Mach-Zehnder modulators

The MZMs I use are 10 Gb/s Integrated Optic Intensity Modulators. An MZM modulates the intensity of an incident optical signal by exploiting Pockels electrooptic effect in a Lithium Niobate crystal situated in one arm of a Mach-Zehnder interferometer. The Pockels effect causes the index of refraction for a particular polarization state to

depend linearly on the applied electric field [59]. By splitting an optical signal with a 50/50 splitter and passing one beam through the crystal, which is sandwiched by a parallel plate capacitor, one can control the phase difference between the two beams. To control the phase difference, one simply varies the voltage across the capacitor, which alters the optical path length for one of the beams. Upon recombination, the resulting optical signal can have an intensity anywhere from zero up to the intensity of the incoming signal multiplied by the insertion loss of the device (which is around 25% for the MZMs I use).

In Ch. 2, I describe the output power  $P_{\text{out}}$  of an MZM with

$$P_{\text{out}} = P_{\text{in}} \cos^2 \left[ \frac{\pi}{2} \left( \frac{V_B}{V_{\pi,\text{dc}}} + \frac{V_{\text{in}}(t)}{V_{\pi,\text{rf}}} \right) \right], \quad (\text{A.2})$$

where  $P_{\text{in}}$  is the power incident on the MZM,  $V_B$  is a constant bias voltage applied to the dc port,  $V_{\text{in}}(t)$  is a time-varying voltage applied to the rf port, and  $V_{\pi,\text{dc}}$  and  $V_{\pi,\text{rf}}$  characterize the widths of the interference fringe corresponding to each of the two ports. Equation A.2, however, neglects the insertion loss of the device and a (generally nonzero) phase shift term. Taking these effects into account, I obtain

$$P_{\text{out}} = g_{\text{IL}} P_{\text{in}} \cos^2 \left[ \frac{\pi}{2} \left( \frac{V_B - V_{\text{top}}}{V_{\pi,\text{dc}}} + \frac{V_{\text{in}}(t)}{V_{\pi,\text{rf}}} \right) \right], \quad (\text{A.3})$$

where  $g_{\text{IL}}$  is the insertion loss of the MZM and  $V_{\text{top}}$  is the dc voltage that corresponds to the top of the interference fringe (*i.e.*, yields maximum transmission). Thus, the operating point  $\Phi$  is now given by

$$\Phi = \frac{\pi}{2} \left( \frac{V_B - V_{\text{top}}}{V_{\pi,\text{dc}}} \right). \quad (\text{A.4})$$

I find experimentally that  $V_{\text{top}}$ , and hence  $\Phi$ , changes with temperature. Thus, it

is important that each component has a proper heat sink to stabilize the temperature and that  $V_{\text{top}}$  is measured repeatedly to ensure that the desired operating point is maintained. To do this, I use a National Instruments 68-Pin Shielded Desktop Connector Block (model number SCB-68) and a LabVIEW program (written with the help of David Rosin) to slowly scan ( $< 1$  kHz) the voltage across the dc port of the MZM and measure the output power. This has to be done with the system at the fixed point ( $V(t) = 0$ ) and with a gain  $\gamma < \gamma_H$  for all values of  $\Phi$ . This data is recorded with a slow-speed photodiode (New Focus 2011-FC, bandwidth dc–200 kHz), as shown in Fig. A.1, and is then fit with a cosine-squared function to simultaneously determine  $V_{\text{top}}$  and  $V_{\pi,\text{dc}}$ . The result of one such measurement is shown in Fig. A.3. After allowing enough time for the components to warm up and reach an approximately constant temperature, I repeatedly implement this protocol to determine how much  $V_{\text{top}}$  fluctuates on average. Based on the standard deviation of these repeated measurements, I estimate my uncertainty in  $\Phi$  to be  $\delta_\Phi = 0.005\pi$ .

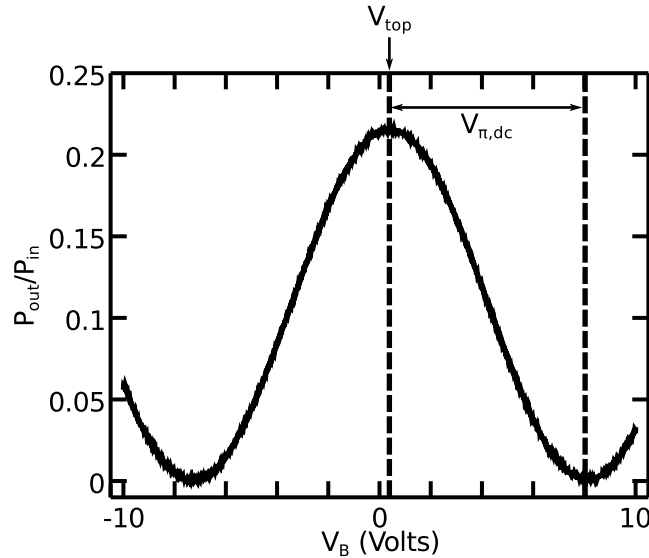


**Figure A.3: Characterizing  $V_{\pi,\text{dc}}$ .** The experimental data (blue) and cosine-squared fit (red) are shown for MZM<sub>2</sub>. Only every 50 experimental data points are shown.

To determine  $V_{\pi,\text{rf}}$ , I apply a 1 MHz ramp voltage to the rf port of the MZM for a fixed value of  $P_{\text{in}}$  and measure  $P_{\text{out}}$ . I do this for several values of  $\Phi$ , and piece the data together to construct a plot of  $P_{\text{out}}$  versus  $V_{\text{in}}$ , as shown in Fig. A.4. By fitting this data to a cosine-squared function, I determine the values of  $V_{\pi,\text{rf}}$  for each MZM. The 95% confidence intervals are small (fractional uncertainty of  $< 0.1\%$ ), however I find that the value of  $V_{\pi,\text{rf}}$  experiences larger changes (fractional uncertainty of  $\sim 1\%$ ) with frequency changes of a few MHz. I therefore use this as an estimate of the fractional uncertainty of  $V_{\pi,\text{rf}}$ .

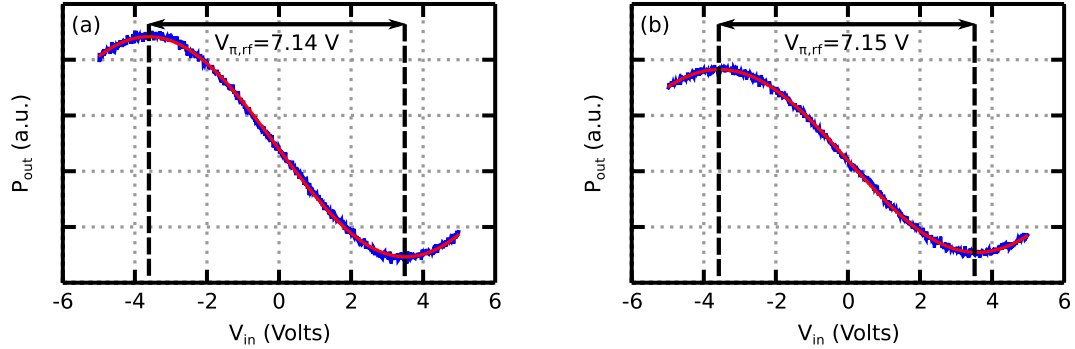


**Figure A.4: Characterizing  $V_{\pi,\text{rf}}$ .** The experimental data (blue) and cosine-squared fit (red) are shown for (a) MZM<sub>1</sub> and (b) MZM<sub>2</sub>. Only every 50 experimental data points are shown. The 95% confidence intervals of the fit do not extend beyond the fit curve shown, so are not plotted.

#### A.1.4 The photodetectors

To convert the optical signals to electrical signals, I use optical receivers manufactured by Miteq (model DR-125G). Like laser diodes, photodiodes are essentially p-n junctions with an applied potential difference [60]. Unlike laser diodes, however, the junction is typically reversed biased so that the width of the depletion region is extended. When radiation within a particular frequency range is incident on this region, electron-hole pairs are created and swept out of the region in opposite directions due to the external

bias. This photocurrent is proportional to the intensity of the light. In these particular photodetectors, the optical signal is coupled to the photodiode via a single-mode optical fiber, making it ideal for my purposes. Additionally, the large bandwidth (30 kHz to 13 GHz) allows for the high speed dynamics I am interested in.

### A.1.5 The bandpass filters

The electronics that comprise the OEOs are bandpass filtered by the inherent bandwidth limitations of each device. For simplicity, I model the entire feedback loop of each OEO as if there is one high-pass and one low-pass corner frequency (*i.e.*, a two-pole bandpass filter placed at the output of the photodetector). The transfer function for such a filter with angular bandwidth  $\Delta$  and angular frequency of maximum transmission  $\omega_0$  can be expressed in the frequency domain as

$$H(s) = \frac{\Delta s}{s^2 + \Delta s + \omega_0^2}, \quad (\text{A.5})$$

where  $s = i\omega$ . In terms of the high-pass and low-pass corner frequencies,  $\Delta = 2\pi(f_l - f_h)$  and  $\omega_0^2 = (2\pi)^2 f_l f_h$ .

By definition, the transfer function is the ratio of the output signal to the input signal in the frequency domain. I am interested, however, in how the input and output to the filter relate in the time domain. In the time domain, the bandpass-filtered signal  $V_{BP}$  is given by

$$V_{BP} + \frac{1}{\Delta} \frac{dV_{BP}}{dt} + \frac{\omega_0^2}{\Delta} \int_0^t V_{BP}(l) dl = V_{PD}, \quad (\text{A.6})$$

where  $V_{PD}$  is the input voltage to the bandpass filter. To verify that this is equivalent to Eq. A.5, one can simply take the Laplace transform of Eq. A.6 and recover  $H(s)$ .

To find the approximate values of  $f_h$  and  $f_l$ , I open up the feedback loop, set  $\Phi = \pi/4$  and  $\gamma < \gamma_H$ , and inject a small sinusoidal voltage into the modulator driver. Using an Agilent PSA Spectrum Analyzer (E4440A) and PSG Vector Signal Generator, I vary the frequency of the input signal while monitoring the amplitude of the output signal. This generates a transfer function of the entire feedback loop, as shown in Fig. A.5. I fit Eq. A.5 to this data, which is clearly an oversimplification. In Ch. 2, however, I

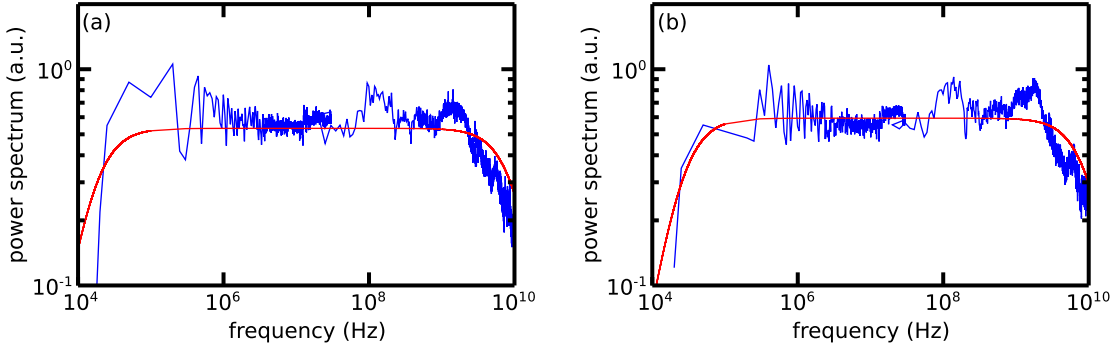


**Figure A.5: Characterizing bandpass filter.** The experimental data (blue) and fit (red) are shown for (a)  $\text{OEO}_1$  and (b)  $\text{OEO}_2$ .

find that modeling a single OEO with a two-pole bandpass filter such as this yields good agreement between experiment, numerical simulation, and analytics. I take the 95% confidence intervals of the fits of  $f_h$  and  $f_l$  as estimates of their experimental uncertainty. I measure  $\gamma$  by injecting a single frequency sine wave ( $f = 4$  MHz) into the same open-loop setup, and therefore take the 95% confidence intervals on the value of the maximum transmission of the transfer function to be an estimate of the experimental uncertainty for  $\gamma$ .

### A.1.6 The modulator drivers

I use 10 Gb/s JDSU optical modulator drivers (model H301) to amplify the rf signal used to drive the MZMs. Each driver has a bandwidth ranging from approximately 75

kHz to 10 GHz and a nonlinear response - the response saturates at high drive voltage. In greater detail, for sinusoidal inputs with low amplitude, the output of the driver is also sinusoidal. As the amplitude of the input is increased, the driver saturates and the output begins to square off. I model the output voltage  $V_{\text{out}}$  as a function of input voltage  $V_{\text{in}}$  with

$$V_{\text{out}} = V_{\text{sat}} \tanh \left[ \frac{g_{\text{MD}} V_{\text{in}}}{V_{\text{sat}}} \right], \quad (\text{A.7})$$

where  $g_{\text{MD}}$  is the linear gain of the driver (which is a negative quantity since the amplifier is inverting) and  $V_{\text{sat}}$  is the saturation voltage of the driver.

To determine  $g_{\text{MD}}$  and  $V_{\text{sat}}$  for each driver, I input a sinusoidal signal with varying amplitude. Given the large bandwidths of the device and dynamics I am interested in, I do this for two different frequencies (1 MHz and 1 GHz). The results are shown in Fig. A.6. I find that the saturation characteristics are frequency dependent: higher

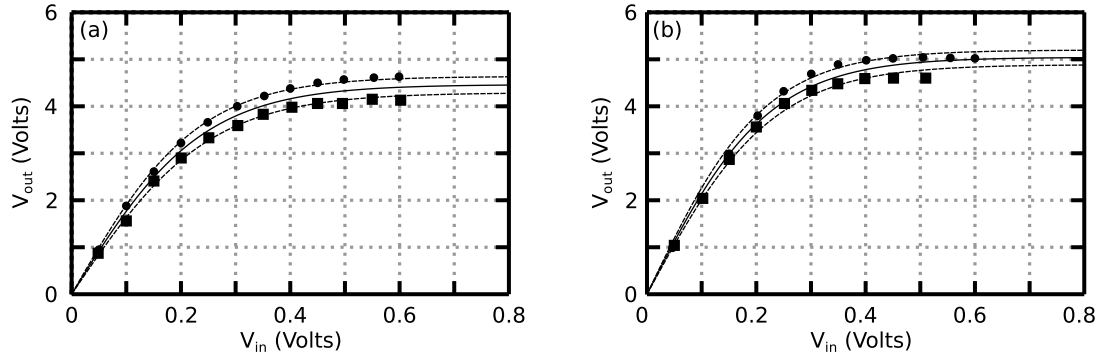


**Figure A.6: Characterizing modulator driver.** The output voltage as a function of input voltage for (a)  $\text{MD}_1$  and (b)  $\text{MD}_2$ . Input frequencies of 1 MHz (circles) and 1 GHz (squares) have different saturation characteristics. The fit (solid) and 95% confidence intervals (dashed) are also shown.

frequencies saturate at a lower voltage than lower frequencies. Rather than further complicate the model, I fit a curve to both sets of data, knowing that this is an over-

simplification. The good agreement between experiment and model in Ref. [8, 9] help to validate this assumption in the case of a single OEO.

### **A.1.7 The variable optical attenuator**

To change the value of the coupling strength along the link from OEO<sub>1</sub> to OEO<sub>2</sub> or OEO<sub>2</sub> to OEO<sub>1</sub>, I use a JDS Uniphase VCB Voltage Controlled Attenuator (VCB-Z013). This attenuator uses as graded neutral density filter, which translates using a step motor and an internal precision potentiometer, to provide attenuation ranging from 1 to 30 dB. To control the attenuation I use a National Instruments 68-Pin Shielded Desktop Connector Block (model number SCB-68) and a LabVIEW program (written with the help of David Rosin). Due to the non-negligible insertion loss, I only place an attenuator along one of the links in order to keep the coupling along the other link at full strength.

### **A.1.8 The time delays**

There are three time delays that are important in my analysis: the self-feedback time delays  $\tau_{11}$  and  $\tau_{22}$ , and the round-trip coupling time delay  $\tau_{12} + \tau_{21}$ . I found in Ch. 2 that the broadband chaotic dynamics generated by a single OEO have TDSs at integer multiples of the self-feedback delay time. Therefore, to estimate the two self-feedback delay times, I record chaotic dynamics for each OEO when uncoupled, compute the corresponding ACFs, and determine the location of the peaks. To estimate the round-trip coupling time delay, I fully couple the OEOs and block the self-feedback loops and repeat the same experiment. Numerical simulations show that the TDSs can be shifted by at most 45 ps from the true value of the time delay. Since the oscilloscope I use to measure the dynamics (Agilent DSO90804A) has a maximum sampling rate of 40

GSa/s, I take my systematic experimental uncertainty in each of the time delays to be 50 ps (two time bins).

Since the variable optical attenuator has an insertion loss of around 20%, I cannot achieve full coupling with it in place. Therefore, to achieve full coupling, I completely remove it from the setup, which changes the value of  $\tau_{12} + \tau_{21}$  from 116.6 ns to 88.3 ns. This is important to note, since numerical simulations show that the values of the TDSs have a slight dependence on the values of the round-trip coupling time delay. This could explain the non-smooth behavior in the vicinity of  $c_{12} = c_{21} = 1$  in the experimental measurements of TDSs versus coupling strength.

## A.2 Summary

In this chapter, I describe and characterize the components that comprise my network of two delay-coupled OEOs that are used in Ch. 4 to implement my sensing method. The values and corresponding experimental uncertainties of each are given in Tables 4.1 and 4.2. In order to keep a tractable model for the two OEO network, I simplify many of the non-ideal behaviors in a similar manner to the approaches taken in Refs. [8, 9, 27], which deal with chaotic and excitable dynamics in single OEOs.

# Appendix B

## Permutation entropies of experimental dynamics

Throughout this dissertation, I characterize the correlation properties of chaotic and stochastic time series with TDSs. I then use these quantifiable changes in correlation properties to sense changes in the properties of a network of dynamical nodes. In this appendix, I introduce the notion of permutation entropy (PE), which is a quantity that is proposed to characterize the complexity of a time series. I then investigate how this complexity metric changes with the network properties, and thus determine how it performs as an observable in my sensing method. The idea to incorporate this metric was suggested to me by Dr. Damien Rontani.

### B.1 Definition of PE

Bandt and Pompe introduce PE as a complexity measure for a time series, where this measure is based on comparisons between neighboring values [50]. They argue that this metric is faster to compute and more robust to noise than other proposed complexity metrics, such as entropies, fractal dimensions, and Lyapunov exponents. It is interesting to note that, for some chaotic systems, this metric has been shown to exhibit similar behavior to that of the largest Lyapunov exponent, which is far more resource-intensive to calculate.

To understand how to calculate PE with order  $n$  and time-delay embedding  $\tau_{\text{emb}}$ , consider a discrete time series  $\{x_t\}_{t=1,\dots,T}$ . Then select  $n$  points from the time series separated by a time  $\tau_{\text{emb}}$  (i.e.,  $\{x_i, x_{i+\tau_{\text{emb}}}, \dots, x_{i+(n-1)\tau_{\text{emb}}}\}$ ) and assign each point a number

based on its relative value to the other points in the set (i.e., 1 = largest, 2 = second largest, ...,  $n$  = smallest). This number assignment is called an ordinal pattern  $\pi$  and is calculated for all  $\{x_i, x_{i+\tau_{\text{emb}}}, \dots, x_{i+(n-1)\tau_{\text{emb}}}\}$ . After calculating the relative frequency with which each ordinal pattern is observed  $p(\pi)$ , the PE with order  $n$  and time-delay embedding  $\tau_{\text{emb}}$  is then given by

$$\text{PE}(n, \tau_{\text{emb}}) = - \sum p(\pi) \log p(\pi), \quad (\text{B.1})$$

where the sum is over all  $n!$  possible ordinal patterns  $\pi$ . This value should fall in the range  $0 \leq \text{PE}(n, \tau_{\text{emb}}) \leq \log n!$ , and, for the calculations that follow, I normalize the PE by its maximum possible value. Note that what makes PE more robust to noise than other entropies is that only the relative order of the values, and not the absolute values, enter into the calculation. Noise is less likely to have an effect on the relative values than it is on the absolute values.

## B.2 Using PEs as observables

I take the same experimental time series for  $(\Phi_1, \Phi_2) = (0, -0.08\pi)$  that I analyze in Ch. 4 with TDSs and maximum and minimum signal amplitudes, and instead calculate PEs to see if sensing is improved with this new choice of observables. I take the embedding dimension  $n = 4$ , which is within the range of recommended values ( $3 \leq n \leq 7$ ) [50] and yields a reasonable computation time. Repeated measurements of the PE with fixed  $n$  and  $\tau_{\text{emb}}$ , the same experimental parameters, and different IHFs, yield a standard deviation of  $4 \times 10^{-4}$ , which I take to be my statistical experimental uncertainty  $\delta_{\text{PE}}$  in measuring PEs.

I find that the value of the PE is sensitive to the embedding time  $\tau_{\text{emb}}$ , as shown

in Fig. B.1. For most values of  $\tau_{\text{emb}}$ , I find that the PE does not change much with changes in coupling strength. Changing  $\tau_{\text{emb}}$  to match the time lag corresponding to a TDS, however, results in a statistically significant change in PE with coupling strength. Note that for the optimal embedding time (magenta curve), the change in PE is only around 0.07, but this is approximately 170 times greater than the associated experimental uncertainty.

It seems reasonable that the PE would only experience appreciable changes for proper embedding times because, as the delta function-like nature of the ACFs indicate, there is essentially no correlation between nearby neighbors in the chaotic time series I am interested in. Therefore, it makes sense to group points together that are separated by a timescale over which correlations are known to occur, as indicated by the appreciable TDSs at these times. To the best of my knowledge, this apparent relationship between TDSs and PEs in time-delayed systems has yet to be explored in the literature.

As with TDSs, I choose to calculate the PE of each time series corresponding to three special values:  $\tau_{\text{self}}$ ,  $\tau_{\text{other}}$ , and  $\tau_{\text{coupling}}$ . Figure B.2 shows the PEs as the coupling strength along each link is varied, and Figs. B.3 and B.4 show the strands and projections that the PEs make in the  $\text{PE}_1$ - $\text{PE}_2$  plane. One-dimensional sensing is possible for two of the six scenarios shown, but two-dimensional sensing is possible for all six scenarios. Furthermore, in all six of these two-dimensional scenarios, the links are distinguishable with the minimum change in coupling strength (23%).

I also calculate the change in each observable (rescaled by  $\delta_{\text{PE}}$ ) for both nodes, as shown in Table B.1. These values should be compared to those in Table 4.3. One can see that the PE at  $\tau_{\text{self}}$  undergoes much larger changes than the corresponding TDS.

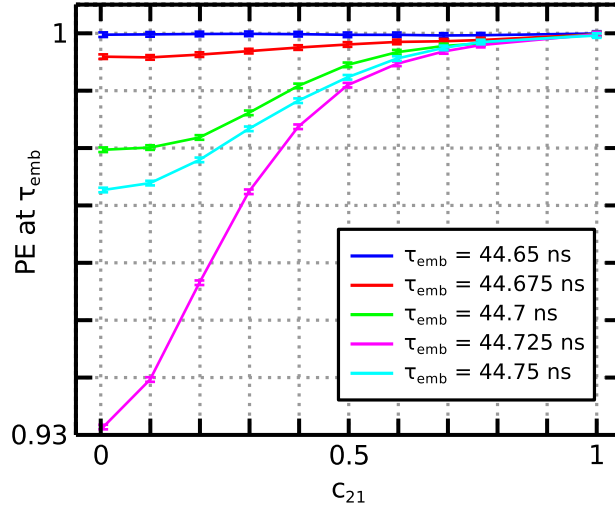


**Figure B.1: PE for different values of the embedding time.** The sensitivity of PE to changes in coupling strength  $c_{21}$  is maximized for  $\tau_{\text{emb}} = 44.725$  ns, which is the time lag corresponding to the TDS at  $\tau_{11}$ . The experimental data for node 1 and  $(\Phi_1, \Phi_2) = (0, -0.08\pi)$  is used in this analysis with embedding dimension  $n = 4$ .

**Table B.1: Changes in PEs for  $(\Phi_1, \Phi_2) = (0, -0.08\pi)$**

Node	Link	$\tilde{\Delta}$ PE $\tau_{\text{self}}$	$\tilde{\Delta}$ PE $\tau_{\text{other}}$	$\tilde{\Delta}$ PE $\tau_{\text{coupling}}$
1	2 $\rightarrow$ 1	170	-6	-14
1	1 $\rightarrow$ 2	0	14	-14
2	1 $\rightarrow$ 2	200	0	-22
2	2 $\rightarrow$ 1	-7	3	-22

### B.3 Summary

The advantages of using PEs as opposed to TDSs as observables are that (1) distinguishability is improved and (2) one of the observables (corresponding to  $\tau_{\text{self}}$ ) undergoes much larger changes over the course of fully blocking the input link. The main disadvantage, however, is that PE, while intended to be faster to compute than other complexity measures, takes longer to compute than a TDS. For example, using standard Matlab functions the difference in computation time is a factor of about 10.

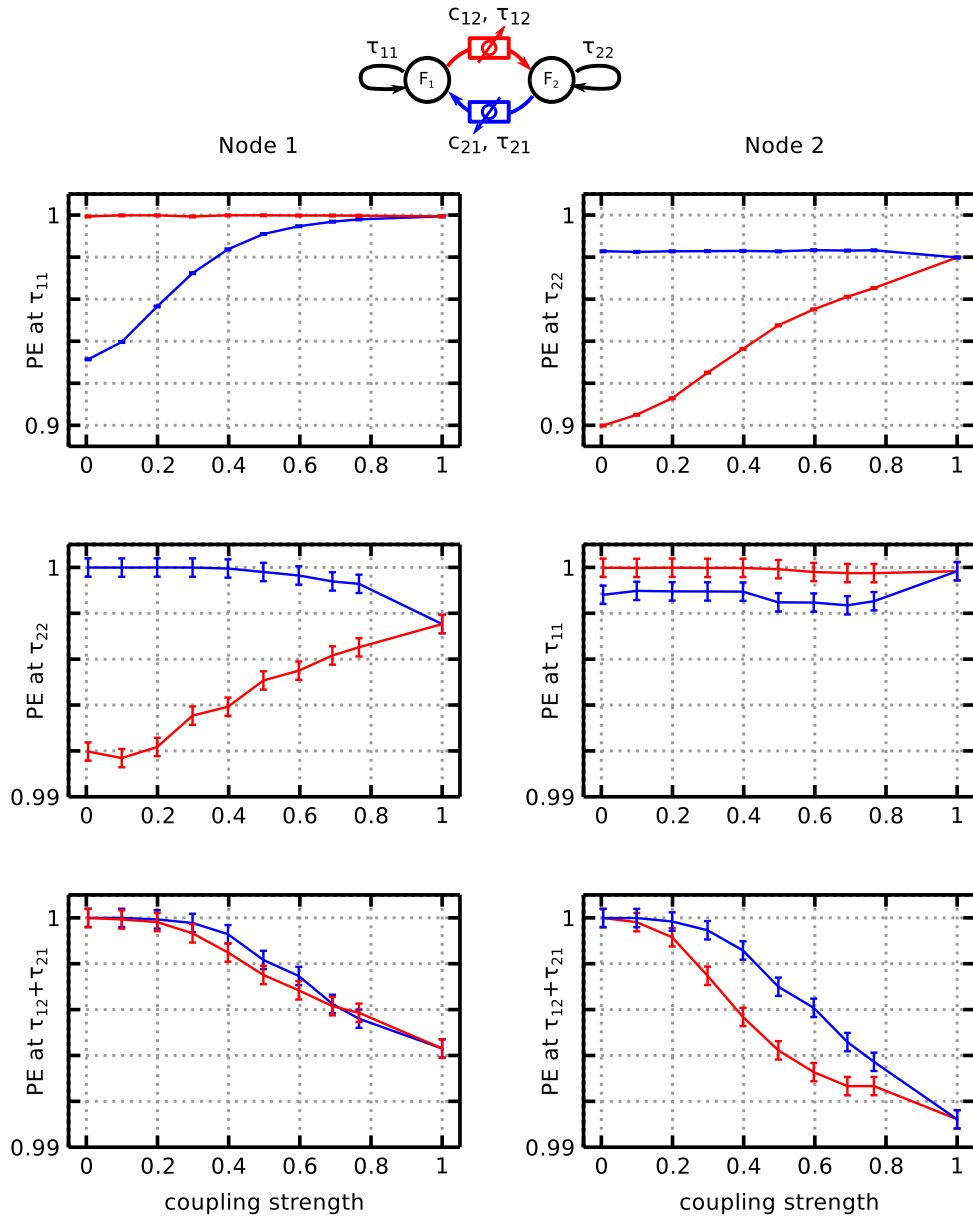


**Figure B.2: Experiment: PEs for  $(\Phi_1, \Phi_2) = (0, -0.08\pi)$ .** Data for both nodes is shown. The red data points correspond to  $c_{12}$  varying (with  $c_{21} = 1$ ) and the blue data points to  $c_{21}$  varying (with  $c_{12} = 1$ ). PEs at (a,b)  $\tau_{\text{self}}$ , (c,d)  $\tau_{\text{other}}$ , and (e,f)  $\tau_{\text{coupling}}$  are shown. The errors bars represent a statistical error of  $4 \times 10^{-4}$ , estimated with the standard deviation of several measurements of the PEs with the same parameters. Note that the vertical scales for side-by-side plots are chosen to be the same for ease of comparison.

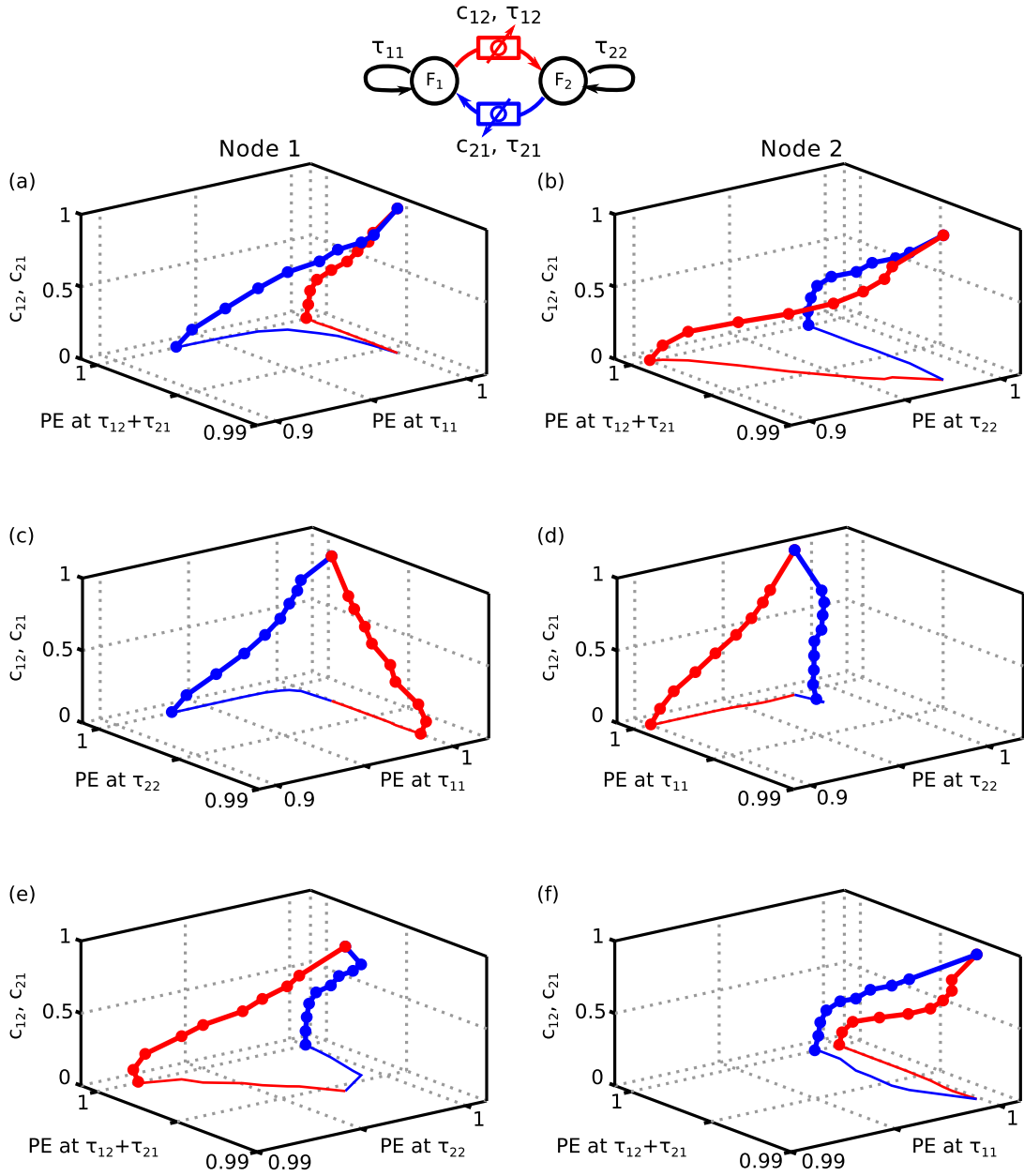


**Figure B.3: Experiment: Strands in PE-coupling strength space.** The PEs were taken from the experiment with  $(\Phi_1, \Phi_2) = (0, -0.08\pi)$  and  $c_{12}$  (red) and  $c_{21}$  (blue) varied from 0 to 1. The projections of the strands onto the PE plane are also shown.

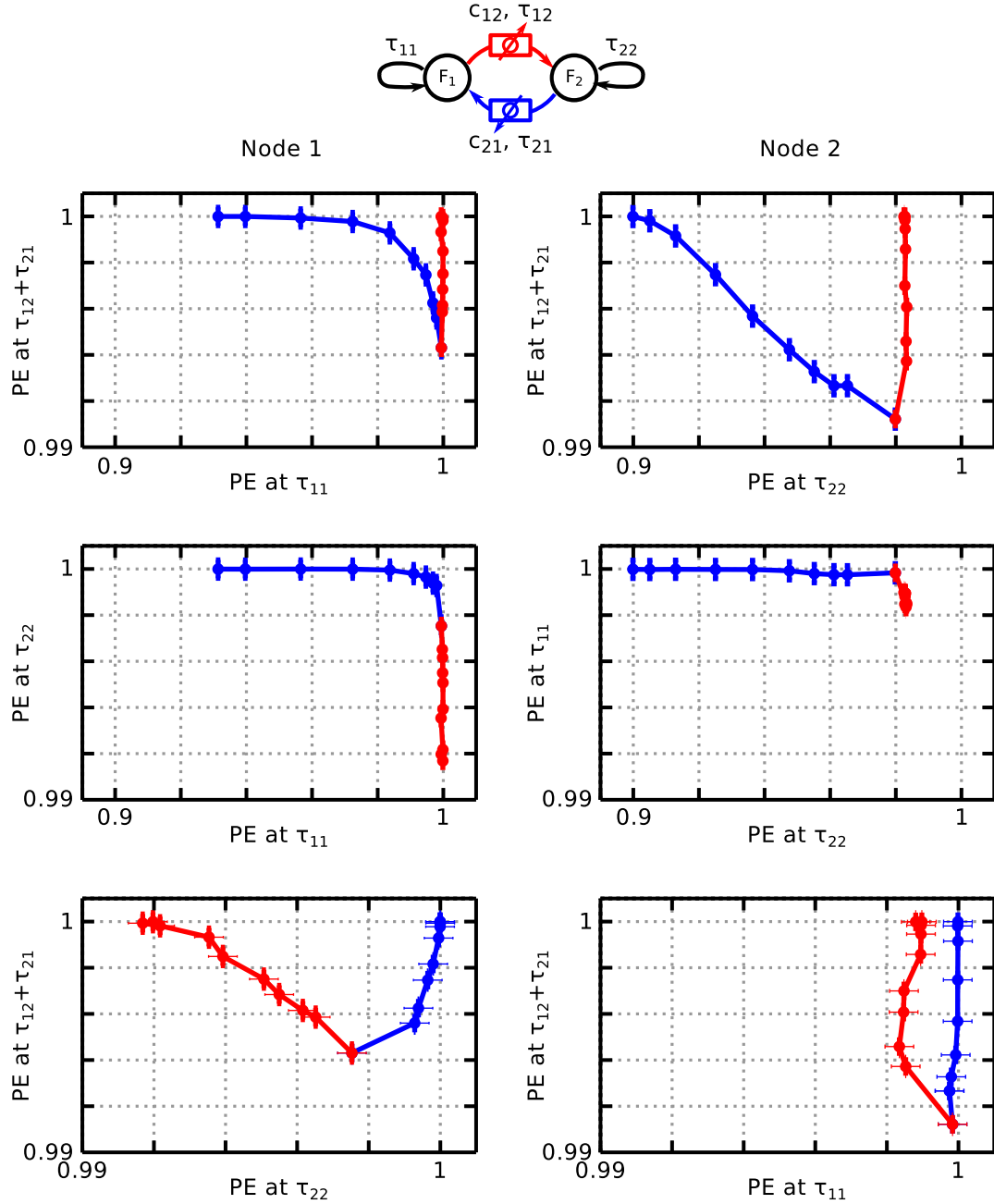


**Figure B.4: Experiment: Projection of strands in  $PE_1$ - $PE_2$  plane.** The PEs were taken from the experiment with  $(\Phi_1, \Phi_2) = (0, -0.08\pi)$  and  $c_{12}$  (red) and  $c_{21}$  (blue) varied from 0 to 1. The minimum attenuation necessary to distinguish the links is approximated by the first value of the coupling strength where the projections are distinct (taking into account the experimental uncertainty, shown with error bars).

Furthermore, in order to calculate a maximally sensitive PE, one needs to first compute the time lag values corresponding to the TDSs.

An interesting byproduct of this analysis is that there seems to be a previously unexplored relationship between TDSs and PEs. Since PE has been shown to be a reliable complexity metric, this lends credence to the idea that TDSs in coupled chaotic oscillators could also be a relevant measure of complexity.

# Appendix C

## Numerical analysis and code

### C.1 ABM Integration

To numerically integrate the DDE models describing the OEOs, I use a multi-step predictor-corrector method known as the four-point Adams-Bashforth-Moulton method [53]. The code for the integrator was written by Dr. Damien Rontani in C, and then compiled using a MEX function so that it could be implemented in MATLAB (see below). The details of the simulations are: the fixed time step is 0.005 ns; the IHF is a 2-ns FWHM Gaussian pulse, with a length equal to the length of the longest time delay; I discard the first 200  $\mu$ s worth of data, which is  $\sim 3$  times longer than the slowest time scale ( $\tau_h$ ); I keep the last 10  $\mu$ s worth of data (2 million points); and each simulation takes  $\sim 2$  minutes.

```
// Adams-Bashforth-Moulton Method for 2 OEOs with time-delay
// Copyright 2012, Damien Rontani for
// Qelectron Lab at Duke University

#include "mex.h"
#include "math.h"
#include "stdlib.h"

double a[4] = { 55.0/24.0 , -59.0/24.0 , 37.0/24.0 , -9.0/24.0};
double b[4] = { 9.0/24.0 , 19.0/24.0 , -5.0/24.0 , 1.0/24.0};

int maxidelay,
    idelay11, idelay12,
    idelay21, idelay22,
    M, S = 4, NDIM=4, D;
```

```

// Parameters OEO #1
double Delta1, epsilon1, d1, g1, gamma11, phi1, tau11;

// Parameters OEO #2
double Delta2, epsilon2, d2, g2, gamma22, phi2, tau22;

// Parameters Coupling
double gamma12, gamma21, tau12, tau21;

// Parameters Simulation
double h, tf, ti;
double *Xvals, *Xinit, *dX, *Corr,
        *param1, *param2, *paramc, *params;

// Nonlinear function associated with thOEO

double FNL11(double X){
    return gamma11*g1/d1*(pow( cos(phi1+d1*tanh(X/g1)), 2)
        -pow(cos(phi1), 2));
}

double FNL22(double X){
    return gamma22*g2/d2*(pow( cos(phi2+d2*tanh(X/g2)), 2)
        -pow(cos(phi2), 2));
}

double FNL12(double X){
    return gamma12*g1/d1*(pow( cos(phi1+d1*tanh(X/g1)), 2)
        -pow(cos(phi1), 2));
}

double FNL21(double X){
    return gamma21*g2/d2*(pow( cos(phi2+d2*tanh(X/g2)), 2)
        -pow(cos(phi2), 2));
}

// Differential system associated with the OEO
void OEOFun(double *dX, double *X , int i, int iidelay11,
            int iidelay12, int iidelay21, int iidelay22)
{
    // OEO #1
    dX[0] = Delta1*epsilon1*X[1+NDIM*i];
}

```

```

dX[1] = Delta1*(-X[1+NDIM*i] - X[0+NDIM*i]
             + FNL11(X[1+NDIM*(iidelay11)])
             + FNL21(X[3+NDIM*(iidelay21)]));
// OEO #2
dX[2] = Delta2*epsilon2*X[3+NDIM*i];
dX[3] = Delta2*(-X[3+NDIM*i] - X[2+NDIM*i]
             + FNL12(X[1+NDIM*(iidelay12)])
             + FNL22(X[3+NDIM*(iidelay22)]));
}

void simulate(){
    int i, j, k;// imod;

    dX    = (double *)malloc(NDIM *sizeof(double));
    Corr  = (double *)malloc(NDIM *sizeof(double));

    // Initialization of vector dX
    for(j=0;j<NDIM;j++){
        dX[j]=0.0;
    }
    // Assign initial values of Xvals from Xinit
    // i stands for time step
    // j stands for the various coordinates of the state vector
    for (i=0; i<maxidelay+S; i++){
        for(j=0;j<NDIM;j++){
            Xvals[j+NDIM*(i%(D))] = Xinit[j+NDIM*(i%(D))];
        }
    }
    // Actual simulation
    for (i=maxidelay+S; i<M; i++){
        // initialize new step for Xval and Corr
        // with previous step
        for(j=0;j<NDIM;j++){
            Xvals[j+NDIM*(i%(D))] = Xvals[j+NDIM*((i-1)%(D))];
            Corr[j] = Xvals[j+NDIM*((i-1)%(D))];
        }
        // Prediction
        // uses x(i-1),x(i-2),x(i-3),x(i-4) to calculate state i
        for(k=0;k<S;k++){
            OEOFun(dX, Xvals, (i-1-k)%(D),
                  (i-1-k-idelay11)%(D), (i-1-k-idelay12)%(D),
                  (i-1-k-idelay21)%(D), (i-1-k-idelay22)%(D));

```

```

        for(j=0;j<NDIM;j++){
            Xvals[j+NDIM*(i\%(D))] += h*a[k]*dX[j];
        }
    }
    // Correction
    // step 1: using in-place value of Pred[i]:
    // stored temporarily in Xvals[i]
    for(k=0;k<S;k++){
        // uses pred(i),x(i-1),x(i-2),x(i-3)
        // to calculate state i
        OEOfun(dX, Xvals, (i-k)\%(D), (i-k-idelay11)\%(D),
            (i-k-idelay12)\%(D), (i-k-idelay21)\%(D),
            (i-k-idelay22)\%(D));
        for(j=0;j<NDIM;j++){
            Corr[j] += h*b[k]*dX[j];
        }
    }
    // step 2: replace the in-place Pred[i] value
    // by Corr[i] in Xvals[i];
    // the code used Xvals[j+NDIM*i] to store temporarily
    // Pred[j+NDIM*i] after prediction step
    // for coding symmetry purposes
    for(j=0;j<NDIM;j++){
        Xvals[j+NDIM*(i\%(D))] = Corr[j];
    }
}
free(dX);free(Corr);
}

void mexFunction (int nlhs, mxArray * plhs [ ],
                 int nrhs, const mxArray * prhs [ ])
{
    // Check number of input s and output s
    if ( nlhs != 1)
        mexErrMsgTxt ( "Wrong number of outputs ! " ) ;
    if ( nrhs != 5)
        mexErrMsgTxt ( "Wrong number of inputs ! " ) ;
    // Getting input s

    Xinit    =  mxGetPr ( prhs [0] );
    param1   =  mxGetPr ( prhs [1] );
    param2   =  mxGetPr ( prhs [2] );

```

```

paramc = mxGetPr ( prhs [3] );
params = mxGetPr ( prhs [4] );

// param OE01
Delta1 = param1[0];
epsilon1 = param1[1];
d1 = param1[2];
g1 = param1[3];
gamma11 = param1[4];
phi1 = param1[5];
tau11 = param1[6];

// param OE02
Delta2 = param2[0];
epsilon2 = param2[1];
d2 = param2[2];
g2 = param2[3];
gamma22 = param2[4];
phi2 = param2[5];
tau22 = param2[6];

// param OE02
gamma12 = paramc[0];
gamma21 = paramc[1];
tau12 = paramc[2];
tau21 = paramc[3];

// param simulation
h = params[0];
ti = params[1];
tf = params[2];
maxidelay = params[3];

// Compute delay and final instant
M = tf/h;
idelay11 = tau11/h;
idelay12 = tau12/h;
idelay21 = tau21/h;
idelay22 = tau22/h;
D = (tf-ti)/h;

if ( M\%D != 0)

```

```

        mexErrMsgTxt ("The number of points saved (D)
                        should be a multiple of the
                        total number of points M ! ");

// Defining outputs
plhs[0] = mxCreateDoubleMatrix(NDIM*D,1,mxREAL);
Xvals   = mxGetPr(plhs[0]);

simulate();
}
}

```

## C.2 Algorithm to calculate TDSs

To find the peaks in the ACF that correspond to TDSs, I first define a small time window (typically 1 ns) to look for the peaks. I then use MATLAB's standard "findpeaks" function to find all of the positive and negative peaks in this window, along with the corresponding time lags at which they occur. I then take the maximum peak amplitude (which could correspond to positive or negative peaks) to be the TDS.

```

function [maxpk,tpk] = findpk(ti,tf,ACF,Lags,dt)

% initial and final times to find peaks within
initial=max(find(ACF(:,1)<ti));
final=min(find(ACF(:,1)>tf));

% finding peak amplitudes and locations
[pks,locs] = findpeaks(ACF(initial:final,2));
locs=locs*dt+Lags(initial-1)*dt;

% finding negative peak amplitudes and locations
[npks,nlocs] = findpeaks(-ACF(initial:final,2));
nlocs=nlocs*dt+Lags(initial-1)*dt;

if ~isempty(pks)
    [maxp,ip]=max(pks);

```

```
        tp=locs(ip);

else
    maxp=0;
    tp=0;
end
if ~isempty(npks)
    [maxn,in]=max(npks);
    tn=nlocs(in);
else
    maxn=0;
    tn=0;
end

if maxp>maxn
    maxpk=maxp;
    tpk=tp;
else
    maxpk=-maxn;
    tpk=tn;
end
```

## Bibliography

- [1] A. E. Motter and D. K. Campbell. Chaos at fifty. *Phys. Today*, 66:27–33, 2013.
- [2] S. H. Strogatz. *Nonlinear Dynamics and Chaos*. Westview Press, Cambridge, MA, 1994.
- [3] M. E. J. Newman. *Networks: An Introduction*. Oxford University Press, Oxford, 2010.
- [4] M. Girvan and M. E. J. Newman. Community structure in social and biological networks. *Proc. Natl. Acad. Sci.*, 99:7821, 2002.
- [5] R. Milo, S. Shen-Orr, S. Itzkovitz, N. Kashtan, and D. Chklovskii. Network motifs: Simple building blocks of complex networks. *Science*, 298:824, 2002.
- [6] M. C. Soriano and J. García-Ojalvo. Complex photonics: Dynamics and applications of delay-coupled semiconductor lasers. *Rev. Mod. Phys.*, 85:421–470, 2013.
- [7] T. Erneux. *Applied Delay Differential Equations*. Springer, New York, NY, 2009.
- [8] K. E. Callan. Broadband chaos generated in a time-delayed opto-electronic oscillator. Master’s thesis, Duke University, 2008.
- [9] K. E. Callan, L. Illing, Z. Gao, D. J. Gauthier, and E. Schöll. Broadband chaos generated by an optoelectronic oscillator. *Phys. Rev. Lett.*, 104:1113901, 2010.
- [10] Laurent Larger and John M Dudley. Nonlinear dynamics: Optoelectronic chaos. *Nature*, 465(7294):41–2, May 2010.
- [11] A. B. Cohen, B. Ravoori, F. Sorrentino, T. E. Murphy, E. Ott, and R. Roy. Dynamic synchronization of a time-evolving optical network of chaotic oscillators. *Chaos*, 20:043142, 2010.
- [12] A. B. Cohen. *Synchronization and Prediction of Chaotic Dynamics on Networks of Optoelectronic Oscillators*. PhD thesis, University of Maryland, 2011.
- [13] K. Lüdge, editor. *Nonlinear Laser Dynamics: From Quantum Dots to Cryptography*. Wiley-VCH, Weinheim, Germany, 2012.
- [14] M. C. Mackey and L. Glass. Oscillation and chaos in physiological control systems. *Science*, 197:287–289, 1997.
- [15] Y. Kuang. *Delay Differential Equations with Applications in Population Dynamics*. Academic Press, San Diego, 1993.

- [16] H. R. Wilson. *Spikes, decisions, and actions: the dynamical foundations of neuroscience*. Oxford University Press, Oxford, UK, 1999.
- [17] K. Ikeda. Multiple-valued stationary state and its instability of the transmitted light by a ring cavity system. *Opt. Comm.*, 30:257–261, 1979.
- [18] K. Ikeda, H. Daido, and O. Akimoto. Optical turbulence: Chaotic behavior of transmitted light from a ring cavity. *Phys. Rev. Lett.*, 45:709–712, 1980.
- [19] K. Ikeda, K. Kondo, and O. Akimoto. Successive higher-harmonic bifurcations in systems with delayed feedback. *Phys. Rev. Lett.*, 49:1467–1470, 1982.
- [20] K. Ikeda and K. Matsumoto. High-dimensional chaotic behavior in systems with time-delayed feedback. *Physica D*, 29:223–235, 1987.
- [21] H. M. Gibbs, F. A. Hopf, D. L. Kaplan, and R. L. Shoemaker. Observation of chaos in optical bistability. *Phys. Rev. Lett.*, 46:474–477, 1981.
- [22] J. D. Farmer. Chaotic attractors of an infinite-dimensional dynamical system. *Physica D*, 4:366–393, 1982.
- [23] K. M. Cuomo and A. V. Oppenheim. Circuit implementation of synchronized chaos with applications to communications. *Phys. Rev. Lett.*, 71:65–68, 1993.
- [24] L. Larger, J. Goedgebuer, and T. Erneux. Subcritical hopf bifurcation in dynamical systems described by a scalar nonlinear delay differential equation. *Phys. Rev. E*, 69:036210, 2004.
- [25] Y. C. Kouomou, P. Colet, L. Larger, and N. Gastaud. Chaotic breathers in delayed electro-optical systems. *Phys. Rev. Lett.*, 95:203903–203907, 2005.
- [26] J. Peil, M. Jacquot, Y. K. Chembo, L. Larger, and T. Erneux. Routes to chaos and multiple time scale dynamics in broadband bandpass nonlinear delay electro-optic oscillators. *Phys. Rev. E*, 79:026208, 2009.
- [27] D. P. Rosin, K. E. Callan, D. J. Gauthier, and E. Schöll. Pulse-train solutions and excitability in an optoelectronic oscillator. *Europhys. Lett.*, 96:34001, 2011.
- [28] L. Weicker, T. Erneux, O. D’Huys, J. Danckaert, M. Jacquot, Y. Chembo, and L. Larger. Strongly asymmetric square waves in a time-delayed system. *Phys. Rev. E*, 86:055201, 2012.
- [29] L. Illing and D. J. Gauthier. Hopf bifurcations in time-delay systems with band-limited feedback. *Physica D*, 210:180–202, 2005.
- [30] A. Argyris, D. Syvridis, L. Larger, V. Annovazzi-Lodi, P. Colet, I. Fischer, J. García-Ojalvo, C. R. Mirasso, L. Pesquera, and K. A. Shore. Chaos-based communications at high bit rates using commercial fibre-optic links. *Nature*, 438:343–346, 2005.

- [31] X. S. Yao and L. Maleki. Optoelectronic microwave oscillator. *J. Opt. Soc. Am. B*, 13:1725–1735, 1995.
- [32] Y. K. Chemo, L. Larger, H. Tavernier, R. Bendoula, E. Rubiola, and P. Colet. Dynamic instabilities of microwaves generated with optoelectronic oscillators. *Opt. Lett.*, 32:2571–2573, 2007.
- [33] L. Larger, M. C. Soriano, D. Brunner, L. Appeltant, J. M. Gutierrez, L. Pesquera, C. R. Mirasso, and I. Fischer. Photonic information processing beyond turing: an optoelectronic implementation of reservoir computing. *Opt. Express*, 20:3241, 2012.
- [34] Y. Paquot, F. Duport, A. Smerieri, J. Dambre, B. Schrauwen, M. Haelterman, and S. Massar. Optoelectronic reservoir computing. *Sci. Rep.*, 2:287, 2012.
- [35] P. J. Menck, J. Heitzig, and M. Norbert J. Kurths. How basin stability complements the linear-stability paradigm. *Nature Phys.*, 9:89–92, 2013.
- [36] A. Gozolchiani and S. Havlin. New tricks for big kicks. *Nature Phys.*, 9:69–70, 2013.
- [37] S. Lepri, G. Giacomelli, A. Politi, and F. T. Arecchi. High-dimensional chaos in delayed dynamical systems. *Physica D*, 70:235–249, 1994.
- [38] R. Nguimdo, P. Colet, L. Larger, and L. Pesquera. Digital key for chaos communication performing time delay concealment. *Phys. Rev. Lett.*, 107:034103, 2011.
- [39] A. Uchida, K. Amano, M. Inoue, K. Hirano, S. Naito, H. Someya, I. Oowada, T. Kurashige, M. Shiki, S. Yoshimori, K. Yoshimura, and P. Davis. Fast physical random bit generation with chaotic semiconductor lasers. *Nature Photon.*, 2:728–732, 2008.
- [40] F. Sorrentino and E. Ott. Adaptive synchronization of dynamics on evolving complex networks. *Phys. Rev. Lett.*, 100:114101, 2008.
- [41] F. Sorrentino and E. Ott. Using synchronism of chaos for adaptive learning of time-evolving network topology. *Phys. Rev. E*, 79:016201, 2009.
- [42] S. H. Strogatz. Exploring complex networks. *Nature*, 410:268–276, 2001.
- [43] *Through-the-wall differential radar*, volume 2938 of *Command, Control, Communications, and Intelligence Systems for Law Enforcement*, Bellingham, WA, 1997. SPIE.
- [44] Y. Che, R. Li, C. Han, S. Cui, J. Wang, X. Wei, and B. Deng. Topology identification of uncertain nonlinearly coupled complex networks with delays based on anticipatory synchronization. *Chaos*, 23:013127, 2013.

- [45] W. Wang, J. Ren, Y. Lai, and B. Li. Reverse engineering of complex dynamical networks in the presence of time-delayed interactions based on noisy time series. *Chaos*, 22:033131, 2012.
- [46] L. M. Pecora and T. M. Carroll. Synchronization in chaotic systems. *Phys. Rev. Lett.*, 64:821–824, 1990.
- [47] L. M. Pecora and T. M. Carroll. Master stability functions for synchronized coupled systems. *Phys. Rev. Lett.*, 80:2109, 1998.
- [48] T. E. Murphy, A. B. Cohen, B. Ravoori, K. R. B. Schmitt, A. V. Setty, F. Sorrentino, C. R. S. Williams, E. Ott, and R. Roy. Complex dynamics and synchronization of delayed-feedback nonlinear oscillators. *Phil. Trans. R. Soc. A*, 368:343–366, 2010.
- [49] R. Autariello, R. Dzakpasu, and F. Sorrentino. Estimating the structure of small dynamical networks from the state time evolution of one node.
- [50] C. Bandt and B. Pompe. Permutation entropy : A natural complexity measure for time series. *Phys. Rev. Lett.*, 88:174102, 2002.
- [51] J. P. Crutchfield and K. Young. Inferring statistical complexity. *Phys. Rev. Lett.*, 63:105–108, 1989.
- [52] R. Lopez-Ruiz, H. L. Mancini, and X. Calbet. A statistical measure of complexity. *Phys. Lett. A*, 209:321–326, 1992.
- [53] W. H. Press, S. A. Teukolsky, W. T. Vetterling, and B. P. Flannery. *Numerical Recipes, Third Edition*. Cambridge University Press, New York, NY, 2007.
- [54] Y. Bard. *Nonlinear Parameter Estimation*. Academic Press Press, New York, 1974.
- [55] O. D’Huys, I. Fischer, J. Danckaert, and R. Vicente. Spectral and correlation properties of rings of delay-coupled elements: Comparing linear and nonlinear systems. *Phys. Rev. E*, 85:056209, 2012.
- [56] T. Schreiber. Measuring information transfer. *Phys. Rev. Lett.*, 85:461–464, 2000.
- [57] G. P. Agrawal and N. K. Dutta. *Long-Wavelength Semiconductor Lasers*. Van Nostrand Reinhold Company, New York, 1986.
- [58] K. Petermann. *Laser Diode Modulation and Noise*. Kluwer Academic Publishers, Boston, 1988.
- [59] K. Iizuka. *Elements of Phonotics, Volume I*. John Wiley and Sons, Inc., New York, 2002.
- [60] R. W. Boyd. *Radiometry and the Detection of Optical Radiation*. John Wiley and Sons, New York, 1983.

## Biography

Kristine Elizabeth Callan was born in Bend, Oregon, on June 28, 1983. As a child, she enjoyed playing with Cabbage Patch Kids, memorizing TV commercials, and talking to her fingers as a means of entertainment. Her creativity and ability to memorize lengthy dialogue served her well at Bend Senior High School, where she was a captain of the basketball and powder puff football teams, a valedictorian of her class, and known for being able and willing to quote lines from “Tommy Boy” on demand. In 2001 she matriculated at Pacific University, where she was encouraged to take her first physics class. While graduating *summa cum laude* with a B.S. in physics and mathematics, Kristine also earned awards such as Outstanding Student in the Natural Sciences and runner-up in the campus-wide Halloween costume contest, in addition to averaging a team-high 3.4 fouls per game and fouling out of six contests as a promising freshman point guard.

In 2005, Kristine made the 2,842-mile drive from Oregon to North Carolina to begin her graduate studies in physics at Duke University. After telling her surprisingly understanding advisor, “I don’t know what I will be doing next year, but I know it’s not this,” she earned an M.S. in the summer of 2008 and took a leave of absence from the Ph.D. program. She found a position teaching physics to high school junior and senior girls at the Winsor School in Boston, Massachusetts. This turned out to be an amazing fit, and not just because Kristine was often mistaken for a student at the school. After learning a great deal from her colleagues and students about physics and herself, Kristine returned to Duke in the fall of 2010 to continue the pursuit of her Ph.D. “Phase II” of graduate school, as she calls it, included highlights such as two intramural basketball championships and the Dean’s Award for Excellence in Teaching, and culminated in the completion of her Ph.D. in 2013.

## Publications

- K.E. Callan, L. Illing, and D. J. Gauthier, "Broadband Chaos," in *Nonlinear Laser Dynamics: From Quantum Dots to Cryptography*, edited by Kathy Lüdge, Ed. (Wiley-VCH Verlag, Weinheim, 2012), Ch. 13, pp. 317-332.
- D. P. Rosin, K. E. Callan, D. J. Gauthier, and E. Schöll, "Pulse-train solutions and excitability in an optoelectronic oscillator," *Eur. Phys. Lett.* 96, 34001 (2011).
- K. E. Callan, L. Illing, Z. Gao, D. J. Gauthier, and E. Schöll, "Broadband Chaos Generated by an Optoelectronic Oscillator," *Phys. Rev. Lett.* 104, 113901 (2010).
- R. J. Wiener, K. E. Callan, S. C. Hall, and T. Olsen, "Proportional feedback control of chaos in a simple electronic oscillator," *Am. J. Phys.* 74, 200 (2006).

## Presentations

- K. E. Callan, D. Rontani, and D. J. Gauthier, "Detecting the position and strength of attenuating elements in a small network." Poster presented at Dynamics Days 2013, Denver, Colorado, Jan. 3-6, 2013
- K. E. Callan, D. Rontani, and D. J. Gauthier, "Sensing capabilities of optoelectronic oscillators due to changes in complexity measures." Poster presented at the 12th Experimental Chaos and Complexity Conference 2012, Ann Arbor, Michigan, May 16-19, 2012.
- K. E. Callan, D. Rontani, and D. J. Gauthier, "Time-delay signatures in broadband chaos generated by optoelectronic oscillators." Poster presented at Dynamics Days 2012, Baltimore, Maryland, Jan. 4-7, 2012.
- K. E. Callan, L. Illing, D. Rosin, D. J. Gauthier, and E. Schöll, "Switching from steady-state to chaos via pulse trains in an optoelectronic oscillator." Poster presented at Dynamics Days 2011, Chapel Hill, North Carolina, Jan. 5-8, 2011.
- K. E. Callan, L. Illing, D. J. Gauthier, "High Speed Chaos Generated in an Optoelectronic Oscillator." Poster presented at Gordon Research Conference: Nonlinear Science, Waterville, ME, June 24-29, 2007.
- K. E. Callan, L. Illing, D.J. Gauthier, "High Speed Chaos Generated in an Optoelectronic Oscillator." Fitzpatrick Institute of Photonics Annual Meeting, Duke University, Sep. 28-29, 2006.
- K. E. Callan, S. C. Hall, R. J. Wiener, and T. Olsen, "Controlling Chaotic Dynamics in a Simple Electronic Oscillator." Contributed talk at the Northwest Section of the American Physical Society Spring Meeting, Victoria, British Columbia, 2005.